Fabrication of Hierarchical Structures by Electrostatic Flocking for Fog Harvesting Applications

DISSERTATION

zur Erlangung des akademischen Grades

eines Doktors der Naturwissenschaften (Dr. rer. nat.)

an der Bayreuther Graduiertenschule für Mathematik und

Naturwissenschaften (BayNAT) der Universität Bayreuth

vorgelegt von

Felix Bretschneider

aus *Lauf a.d. Pegnitz*

Bayreuth, 2024

Die vorliegende Arbeit wurde in der Zeit von November 2020 bis April 2024 in Bayreuth am Lehrstuhl Makromolekulare Chemie II unter Betreuung von Herrn Professor Dr. Andreas Greiner angefertigt.

Vollständiger Abdruck der von der Bayreuther Graduiertenschule für Mathematik und Naturwissenschaften (BayNAT) der Universität Bayreuth genehmigten Dissertation zur Erlangung des akademischen Grades eines Doktors der Naturwissenschaften (Dr. rer. nat.).

Form der Dissertation: Monographie

Dissertation eingereicht am: 26.04.2024

Zulassung durch das Leitungsgremium: 15.05.2024

Wissenschaftliches Kolloquium: 11.11.2024

Amtierender Direktor: Prof. Dr. Jürgen Köhler

Prüfungsausschuss:

Prof. Dr. Andreas Greiner (Gutachter)

Prof. Dr. Johannes Brendel (Gutachter)

Prof. Dr. Markus Retsch (Vorsitz)

Prof. Dr. Georg Papastavrou

Teile der Arbeit wurden in folgender Publikation veröffentlicht:

M. Weber, F. Bretschneider *et al.*, Mimicking cacti spines via hierarchical self-assembly for water collection and unidirectional transport *Adv. Mater. Interfaces* **11**, 2400101 (2024)

Diese Publikation ist in der vorliegenden Arbeit mit der Literaturstellen [145] zitiert.

Table of Content

Table of Abbreviations

Definition	Abbreviation
Alternating Current	AC
All-in-One	AE
1,3,5-Benzenetricarboxamides	BTA
N^1,N^3,N^5-tri[2-(diisopropylamino)-ethyl]-1,3,5-benzenetricarboxamide	*iPr*-BTA
N^1, N^3, N^5-tri[2-(diethyl amino)-ethyl]-1,3,5-benzenetricarboxamide	Et-BTA
N^1, N^3, N^5-tri[2-(dimethyl amino)-ethyl]-1,3,5-benzenetricarboxamide	Me-BTA
N^1, N^3, N^5-tri[2-(dipropyl amino)-ethyl]-1,3,5-benzenetricarboxamide	*n*Pr-BTA
Degrees (Angle)	deg.
N, N,-Dimethylformamide	DMF
Environmental Scanning Electron Microscopy	ESEM
Food and Agriculture Organization	FAO
Fused deposition modeling	FDM
Magnetorheological drawing lithography	MRDL
Nuclear Magnetic Resonance	NMR
Polyamide	PA
Polyethyleneterephthalte	PET
Polypropylene	PP
Physical Vapor Deposition	PVD
Poly(vinylidene-*co*-hexafluoropropylene)	P(VDF-*co*-HFP)
Room temperature	r.t.
Scanning Electron Microscopy	SEM
Top-to-bottom	TB

Short Summary

Nature evolved intriguing and complex structures to harvest water in arid environments. Over recent years, the scientific community investigated these structures in detail and used bioinspired and biomimetic concepts to support the freshwater infrastructure in arid regions. Since many species rely on anisotropic morphologies to efficiently transport and condense water, a fiber-based coating technique may be a promising starting point to adapt these structures. Such a well-investigated and established fiber-based coating technology is electrostatic flocking. During the electrostatic flocking process, short microfibers are accelerated in an electric field and anchored by an adhesive layer to a substrate. Due to the influence of the electrostatic field lines, the microfibers align vertically relative to the substrate.

This thesis aimed to expand the field of electrostatic flocked-based water transporting and collecting systems as well as illustrate the potential of electrostatic flocking as a simple and low-cost coating technique. Hereby, exclusively bioinspired and biomimetic concepts are utilized. However, implementing these structures in material science is generally challenging due to the complex and hierarchical structures of biological systems. Therefore, the successful implementation of bioinspired and biomimetic flock-based systems is assumed to have, on the one hand, efficient fog interception and, on the other hand, would illustrate the potential of the electrostatic flocking technique.

The thesis achieved these goals in four chapters. In the first chapter, a preliminary study was conducted to investigate the interaction of flocked substrates with water in general. Besides the specific water transport mechanism of the flocked structure, the fog interaction was investigated. It was shown that hydrophobic polyamide flock fibers captured fog droplets at the tip of the fiber, which agglomerated under continuous irrigation to larger droplets. On the other hand, the fog captured by hydrophilic viscose flock fibers led to the wetting of the water droplets along the fiber axis. The study also revealed that the pore size and fiber dimensions influenced the interaction with fog. For flocked substrates with small pore sizes, fog mainly condensed on the fiber tip, while for larger pore sizes, more of the fiber surface was exposed to the fog stream.

Based on the preliminary study, three bioinspired and biomimetic concepts were developed and implemented utilizing the distinct features of the Namib desert beetle, cactus spine, and Dandelion seed, respectively. In the second chapter, the patterned backplate of the Namib desert beetle consisting of hydrophilic spots with a hydrophobic background was adapted by utilizing a stamp to selectively apply hydrophilic viscose flock fibers on a hydrophobic electrospun nonwoven. The resulting membrane showed similar fog interaction as the backplate of the Namib desert beetle.

In the third chapter, supramolecular spines were developed based on the molecular self-assembly of 1,3,5-benzenetricarboxamides in a flocked substrate. Due to specific molecular self-assembly conditions, supramolecular spines were formed. The supramolecular spines showed unidirectional water transport capabilities similar to the natural cactus spine. This device was equally developed and characterized by Melina Weber (University of Bayreuth, Macromolecular Chemistry I, Prof. H.W. Schmidt) and the author of this thesis.

In the fourth and final chapter, polymer flock fibers with a Dandelion seed morphology were developed by a sequential flocking approach. The interaction with fog was investigated in detail, and based on these results, a fog-harvesting device was designed. The resulting fog harvesting device showed improved fog-collecting abilities due to the coalescing collecting mechanism and an improved interception compared to a reference sample.

Kurzfassung

Die Natur hat faszinierende und komplexe Strukturen entwickelt, um in trockenen Gebieten zu überleben. In den letzten Jahren wurden diese Strukturen eingehend untersucht und bioinspirierte und biomimetische Konzepte zum effizienten Einfangen von Nebel entwickelt, um die Trinkwasserinfrastruktur in trockenen Gebieten zu unterstützen. Hierbei basieren viele solcher biologischen Vorbilder auf anisotrope Strukturen. Daher könnte eine faserbasierte Beschichtungstechnik ein vielversprechender Ansatzpunkt zur Adaption solcher Strukturen sein. Eine etablierte und faserbasierte Beschichtungstechnologie ist die elektrostatische Beflockung. Während des elektrostatischen Beflockungsprozesses werden kurze Mikrofasern in einem elektrischen Feld beschleunigt und durch eine Klebstoffschicht auf einem Substrat verankert. Aufgrund der elektrostatischen Feldlinien richten sich die Mikrofasern vertikal zum Substrat aus.

Das Ziel dieser Arbeit wurde in zwei Hauptbereiche unterteilt: Zunächst wurde das Potenzial der elektrostatischen Beflockung zur Nebelkondensation aufgezeigt. Des weiteren wurde die elektrostatische Beflockung als eine unkomplizierte und kostengünstige Beschichtungstechnik hervorgehoben. Diese Ziele wurden simultan erreicht, indem ausschließlich bioinspirierte und biomimetische Konzepte zum Einsatz kamen. Da die Umsetzung solcher bioninspirierten und biomimetischen Strukturen in der Materialwissenschaft aufgrund des komplexen und hierarchischen Aufbaus eine Herausforderung ist, würde eine erfolgreiche Umsetzung von bioinspirierten und biomimetischen flockbasierten Systemen zum einen eine effiziente Interaktion mit Nebel ermöglichen und zum anderen das Potenzial der elektrostatischen Beflockungstechnik verdeutlichen.

Im Rahmen dieser Arbeit wurden diese Ziele in vier Kapiteln erreicht. Im ersten Kapitel wurde eine Vorstudie zur Untersuchung der Wechselwirkung von beflockten Substraten mit Nebel durchgeführt. Neben dem spezifischen Wassetransportmechanismus, wurde gezeigt, dass hydrophobe Polyamid-Flockfasern Nebeltröpfchen an der Faserspitze einfangen, welche bei kontinuierlicher Benebelung zu größeren Tröpfchen agglomerieren. Die Wechselwirkung von Nebeltröpfchen mit einer hydrophilen Viskoseflockfaser führt hingegen zu einer kompletten Benetzung der Faseroberfläche entlang der Faserachse. Im Rahmen der Vorversuche wurde auch der Einfluss der Porengröße des beflockten Substrats und der Flockfaserdimensionen qualitativ untersucht. Für beflockte Substrate mit einer kleinen Porengrößen kondensierte der Nebel hauptsächlich an der Faserspitze, während mit einer zunehmenden Porengrößen ein größerer Teil der Faseroberfläche vom Nebel benetzt wurde.

Auf der Grundlage der Vorstudie wurden drei bioinspirierte und biomimetische Konzepte entwickelt und umgesetzt. Das erste Konzept orientiert sich an den Merkmalen des namibischen Wüstenkäfers, wohingegen den weiteren Konzepten die Eigenschaften eines Kaktusstachels sowie Löwenzahnsamens zu Grunde liegen. Im zweiten Kapitel wurde die strukturierte Rückenplatte des namibischen Wüstenkäfers adaptiert, welche sich aus hydrophilen Flecken mit einem hydrophoben Untergrund zusammensetzt. Mit Hilfe eines Stempels wurden hydrophile Viskoseflockfasern selektiv auf ein hydrophobes elektrogesponnenes Nanofaservlies appliziert, und die Interaktion mit Nebel näher untersucht. Ähnlich zu dem natürlichen Vorbild, konnte beobachtet werden, dass sich Wassertropfen auf den Viskose Flockfasern sammeln, die dann zu größeren Tropfen wachsen bis diese von dem Substrat abtropfen.

Im dritten Kapitel wurden supramolekulare Stacheln entwickelt, die auf der Selbstassemblierung von 1,3,5-Benzoltricarboxamiden (BTAs) in einem beflockten Substrat basieren. Die supramolekularen Stacheln zeigten neben einer strukturellen auch eine funktionelle Ähnlichkeit zu dem natürlichen Vorbild und waren ebenfalls in der Lage Wasser unidirektional zu transportieren. Dieses Konzept wurde zusammen mit Melina Weber (Makromolekulare Chemie I, Prof. H.W. Schmidt) entwickelt und untersucht.

Im vierten und letzten Kapitel wurden Polymerflockfasern mit der Morphologie von Löwenzahnsamen durch einen sequenziellen Beflockungsansatz entwickelt. Dabei wurde die Wechselwirkung mit Nebel eingehend untersucht. Auf der Grundlage dieser Ergebnisse wurde eine Nebelsammelvorrichtung entworfen und die Nebelausbeute im Vergleich zu einer Referenzprobe quantifiziert.

1. Introduction

Due to millennia of evolution, nature developed intriguing structures to overcome common everyday problems. These structures include, but are not limited to, the hierarchical morphology of collagen, [1] the efficient design of honeycombs, [2] the anisotropic features of cacti spines, [3] the patterned backplate of the Namib desert beetle, [4] and the filament structure of Dandelions. [5] Applying these solutions to material science, physics, or chemistry is generally referred to as biomimicry or bioinspiration. [6] Inspired by the biological role models, the scientific community developed several approaches for a plethora of different applications, [3,7] ranging, for example, from penguin feather-like nanofiber composites for air filtration [8] to the special wettability of Namib desert beetle plate [9] to efficiently condense fog as a sustainable water resource, as well as many more. [10,11]

Due to the increased evolutionary pressure, a fascinating source for biological adaptations is often observed in extreme places. [12,13] Especially arid and semi-arid climate regions, where access to water is drastically limited, offer an astonishing diversity despite the life-restricting feature of water scarcity. [12–14] Therefore, it is not surprising that many species adapted to harvest unconventional water resources such as fog and dew to support their water budget. [15] Due to the immanent risks of climate change, learning from these species becomes more and more relevant. As highlighted in a recent Food and Agriculture Organization (FAO) report, [16] communities will encounter water shortages in the upcoming years. As a result of climate change, population growth, and water mismanagement, the stress on freshwater resources will drastically increase. In fact, a Global Risks Report of the World Economic Forum identified water scarcity as a high-impact risk.[17,18] A new sustainable water resource may be found in naturally occurring fog streams. [19–21] Therefore, a lot of effort has been invested in adapting biological structures to harvest fog more efficiently over recent years. [22–24] While many different species live in places with significant water scarcity and therefore evolved specific counter strategies, the underlying physics converges to a few major physical effects: Manipulation of the wettability, utilization of a LAPLACE pressure difference, and microstructured surfaces. [11,23,25]

Wettability and Water Transport Effects

The wettability generally refers to the interaction of water with a surface. [26] If the resulting water droplet spreads, the surface is defined as hydrophilic, while a stable spherical droplet gives rise to a hydrophobic surface. [26] The geometry of the droplet on a surface is described by the contact angle. A hydrophilic surface has a contact angle of < 90 deg and a hydrophobic of > 90 deg. This concept can be further expanded by incorporating the extreme cases. Complete wetting of a surface with a contact angle of 0 deg is defined as superhydrophilic, and a perfect spherical droplet on surfaces with a contact angle of 150-180 deg as superhydrophobic (cf. Figure 1.1). [26]

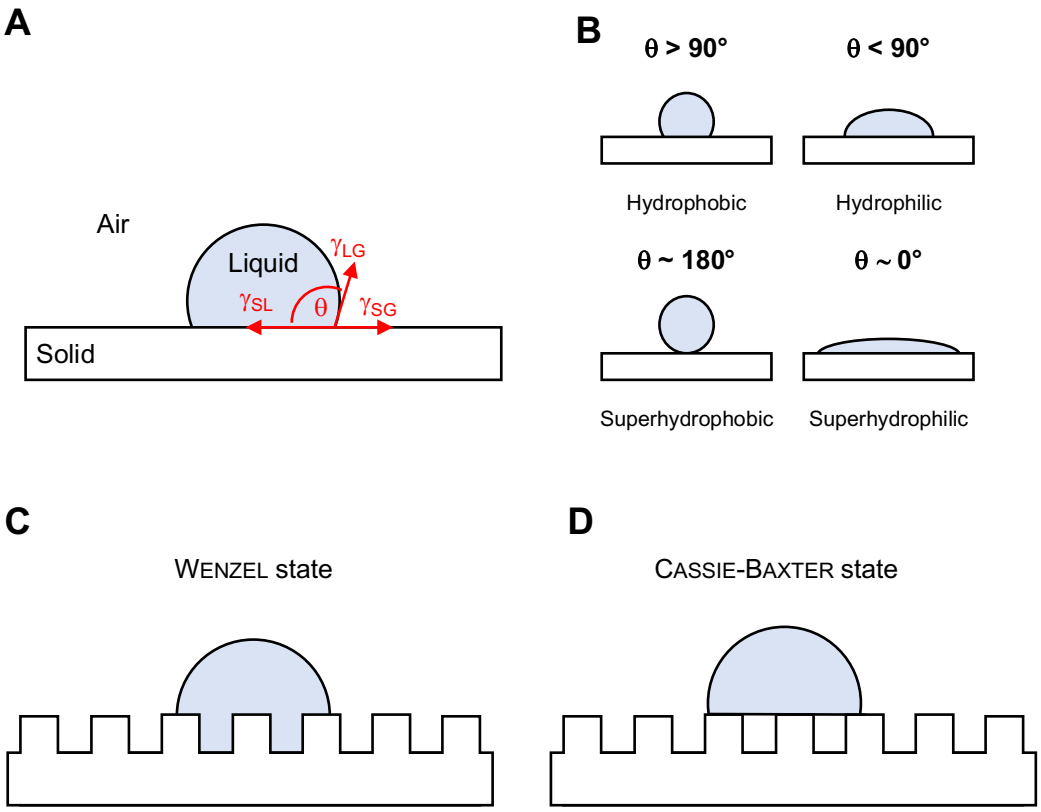

Figure 1.1: Wettability states of droplets on a surface. (**A**) Single water droplet on a surface with the contributing surface energies to the contact angle. (**B**) Illustration of a water droplet on a hydrophobic, hydrophilic, superhydrophobic, and superhydrophilic surface. (**C**) Water droplet adjustment according to WENZEL and (**D**) according to CASSIE-BAXTER. Adapted from [11].

In general, the contact angle of a flat, non-structured surface is described by YOUNG's Equation (cf. Equation 1.1). Here, the contact angle Θ depends on the interfacial tension between solid/gas γ_{SG}, solid/liquid γ_{SL} and liquid/gas γ_{LG}: [26]

$$\gamma_{SG} = \gamma_{SL} + \gamma_{LG} \cos \Theta$$

(1.1)

If a surface roughness is introduced, the contact angle deviates from the YOUNG's equation. In the context of surface roughness, it is imperative to distinguish between homogeneous and heterogeneous wetting. The wetting of chemically homogenous surface is described by the WENZEL-Equation. According to Equation 1.2, the wettability is strengthened by introducing a surface structure. Thus, a hydrophilic surface becomes more hydrophilic and a hydrophobic surface more hydrophobic: [27]

$$\cos \Theta^* = r \cdot \cos \Theta_e$$

(1.2)

The apparent contact angle Θ^* depends on a roughness value r, which relates the projected surface area to the real surface area and varies between 0 and 1. The intrinsic contact angle is described by Θ_e.

For surfaces with very high porosity or chemical heterogeneous surfaces, the WENZEL equation is no longer valid. Here, the CASSIE-BAXTER-Equation gives results with higher confidence. [28] The CASSIE-BAXTER-Equation relates the fractional area f_i to the apparent and intrinsic contact angle. Assuming a water contact angle of 180 deg for air, the equation can be simplified accordingly:

$$\cos \Theta^* = \sum f_i \cos \Theta_i$$

$$\cos \Theta^* = f_1 \cos \Theta_1 - (1 - f_1)$$

(1.3)

In general, a clear differentiation between WENZEL and CASSIE-BAXTER state rarely occurs. As Khadka *et al.* and Marmur have highlighted, a mixed wetting state are frequently observed. In the mixed wetting state, the asperities as well as the pores are only partially wetted. The resulting mixed state wetting is described by the following equation: [29,30]

$$\cos \Theta^* = r \cdot f \cos \Theta + f - 1$$

(1.4)

Taking advantage of differences in surface wettability, water droplets can be transported along the surface by a wettability gradient. Such a gradient can be achieved either by partially covering the surface with wax, with a roughness gradient, or, for the example of a cactus spine, a combination of both. [31] For the case of a cactus spine, due to the gradient of the surface free energy, a force F is produced that drives the water droplets from the spine tip l_{tip} to the base l_{base}: [31,32]

$$F = \int_{l_{tip}}^{l_{base}} \gamma(\cos\Theta_{\mathrm{A}} - \cos\Theta_{\mathrm{R}})dl \tag{1.5}$$

The second major effect of transporting water droplets is achieved by utilizing a LAPLACE pressure difference. In general, the LAPLACE pressure is a phenomenon that describes the pressure difference of a droplet between the inside and outside of a curved interface. [26] Consequently, nature has evolved several mechanisms to exploit this effect for the directional transport of water droplets. Examples include beads on spider silk [33] or the cone geometry of cacti spines. [31] If a droplet interacts with a surface, it will deform and adapt to the geometry of the surface. Since the LAPLACE pressure depends on the droplet curvature, an asymmetric surface geometry leads to a difference in droplet curvature and, thus, to a pressure difference and to an active droplet transport. For the case of a cacti spine, the LAPLACE, pressure difference ΔP can be described as shown in Equation 1.5: [31,34–37]

$$\Delta P = -\int_{R_1}^{R_2} \frac{2\gamma}{(r + R_0)^2} \sin\beta dz \tag{1.6}$$

Where r and R_0 give the local radii and drop radius. β is the half apex angle, γ the surface tension of the interacting liquid, and dz the integrating variable along the diameter of the spine.

The last significant consideration pertains to the impact of microgrooved surfaces. On a hydrophilic, untextured surface, water droplets typically spread isotropically in all directions. However, if such a surface is patterned with aligned grooves, the droplets tend to spread along these grooves. [36,38] Natural structures often exhibit a combination of one or all of the effects discussed above. As a result, it becomes difficult to distinguish between these effects clearly.

While many different species rely on passive water transport effects, only a few are well studied. Most noteworthy in the context of this thesis are the Namib desert beetle, cacti plants, and Dandelion flower seeds. The water interaction of these species is described in more detail in the following chapters.

Namib Desert Beetle

Due to its unique adaptations, the Namib desert beetle is a well-described and observed organism. [4,39,40] The Namib desert is located on the west coast of the African continent, close to the Atlantic Ocean. Owing to the distinct geographical features, the desert region is characterized by an arid environment that experiences regularly recurring fog streams, leading to special evolutionary adaptions like the Namib desert beetle. [19] As described by A. R. Parker and C.R. Lawrence, the beetle's elytra – or backplate – consists of alternating hydrophobic and hydrophilic regions (cf. Figure 1.2 A, B). [4] The hydrophilic regions form bumps, which are 0.5–1.5 mm apart. At the microscopic level, the peaks of these bumps are hydrophilic, while the troughs are covered in wax, creating a hydrophobic background. A schematic illustration by D. Gurera and B. Bhushan of the patterned backplate is shown in Figure 1.4 C. This structure allows the beetle to collect water droplets by condensing fog droplets onto the hydrophilic bumps. Once a critical droplet size is reached, the condensed fog droplets roll off the tilted backplate against the fog stream. The fog speed v, where below the droplets roll off, can be estimated by EULER'S first law: [4]

$$v \approx \sqrt{\left[\left(\frac{\rho_{water}}{\rho_{air}}\right)\left(\frac{4}{3}\right) Rg \cdot \sin\vartheta\right]} \tag{1.7}$$

Where ρ_{water} and ρ_{air} correspond to the density of water and air, respectively. R is the droplet radius, g is the gravitational constant, and ϑ the backplate's tilting angle.

A fundamental and semi-empiric description of the tilting angle – also referred to as the roll-off angle - is provided by C. G. L. Furmidge. In his publication, the roll-off angle was related to the mass of the droplet $m_{droplet}$, the gravitational acceleration, the projected width of the droplet during movement w, the surface tension, and the advancing Θ_{Adv} and receding Θ_{Rec} contact angles of the water droplet: [41,42]

$$m_{droplet} \cdot g \sin \vartheta = w \cdot \gamma_{LG}(\cos \Theta_{Rec} - \Theta_{Adv}) \tag{1.8}$$

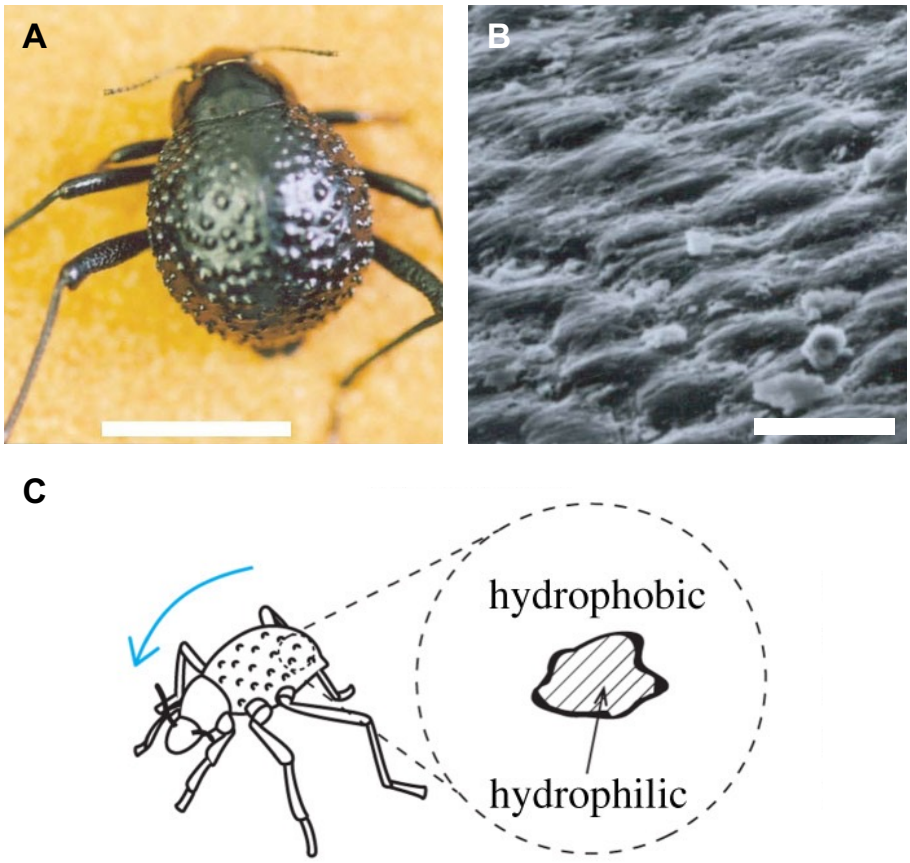

Figure 1.2: The Namib Desert Beetle and its Backplate. (**A**) shows a photograph focused onto the backplate of the Namib desert beetle. (**B**) Scanning electron microscopy micrograph of the patterned backplate. The scale bars in (**A**) and (**B**) correspond to 10 mm and 10 µm, respectively. (**C**) shows a schematic illustration of the beetle's backplate consisting of hydrophobic and hydrophilic regions. (**A**, **B**) Reprinted with permission from [4], (**C**) with permission from [25].

The structure of the Namib desert beetle's backplate is readily implemented in the scientific literature for the purpose of fog harvesting.[40] The approaches include controlled etching, [43] weaving, [44] or micro pipetting. [45] A noteworthy publication by L. Zhang *et al.* implemented a Namib desert beetle-inspired surface by ink-jet printing technique. [9]

The authors introduced a one-step, mask-free method using inkjet printing technology to produce superhydrophilic micropatterns on superhydrophobic surfaces (cf. Figure 1.3). The researchers used a mussel-inspired ink, composed of a dopamine solution. This solution was applied directly to superhydrophobic surfaces via inkjet printing. Subsequently, the dopamine solution polymerized in air to polydopamine, forming superhydrophilic spots on a superhydrophobic glass slide. The resulting micropatterned superhydrophobic surfaces exhibited enhanced water collection efficiency compared to uniform superhydrophilic and superhydrophobic surfaces. The inkjet printing method was shown to be a promising approach for large-scale patterning of superhydrophobic surfaces with high precision and pattern stability.

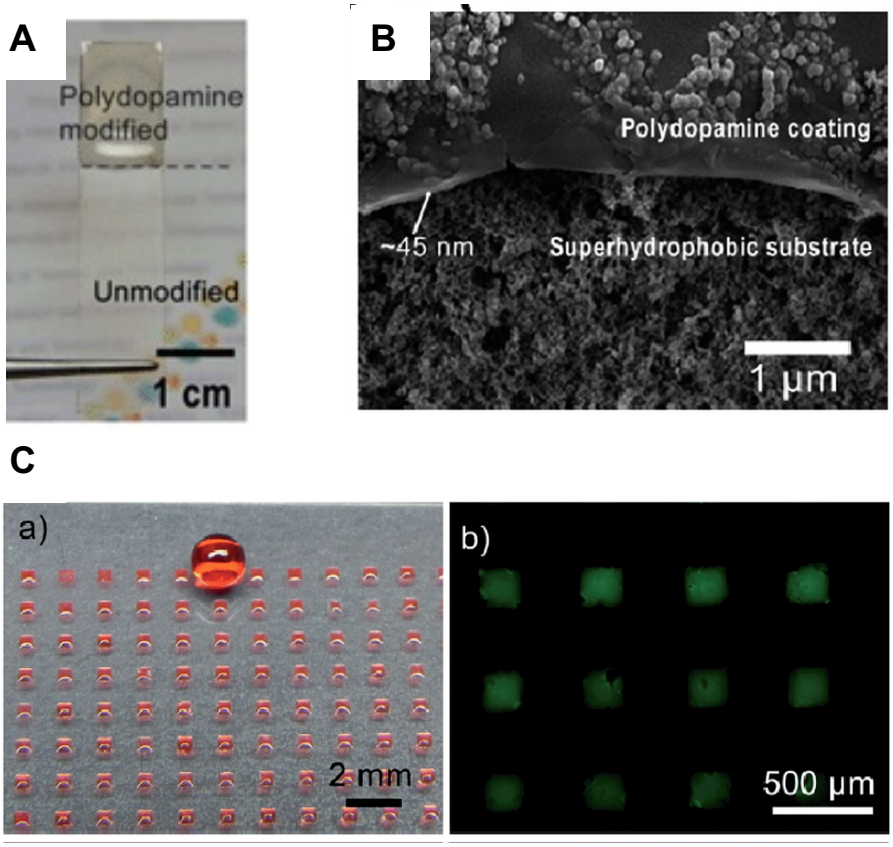

Figure 1.3: Namib Desert Beetle-inspired substrate by inkjet printing. (**A**) Photograph of superhydrophobic modified glass slide coated with superhydrophilic polydopamine. (**B**) Scanning electron microscopy micrograph of the patterned substrate. (**C**) Photogaph of the patterned substrate with superhydrophobic and superhydrophilic regions. Reprinted with permission from [9].

Cactus Spine

One of the most prevalent organism in arid regions is the cactus plant. Cacti specialize their metabolism and tissue to store water for a long time to bypass dry periods during the day.[46] Additionally, cacti optimized their water budget by collecting condensed atmospheric water as they adapted their natural defense mechanism – namely, cacti spines. For this, cacti spines utilize three general features for the water-collecting mechanism. First, the conical structure of the spine results in a curvature gradient along the spine axis. [31,37] This further leads to a LAPLACE pressure difference at the spines, forcing water droplets to move toward the spine's base (cf. Equation 1.5). Second, the spines developed microgrooves parallel to the spine axis that guide the droplet along these grooves. [31,47] Third, a roughness gradient between the tip and base translates, according to the WENZEL state, to a wettability gradient (cf. Equation 1.5). [27] Combined with the microstructured surface, condensed water droplets are efficiently transported from the tip to the base of the spine, as schematically illustrated in Figure 1.4, where the droplets are then taken up by the cactus plant.

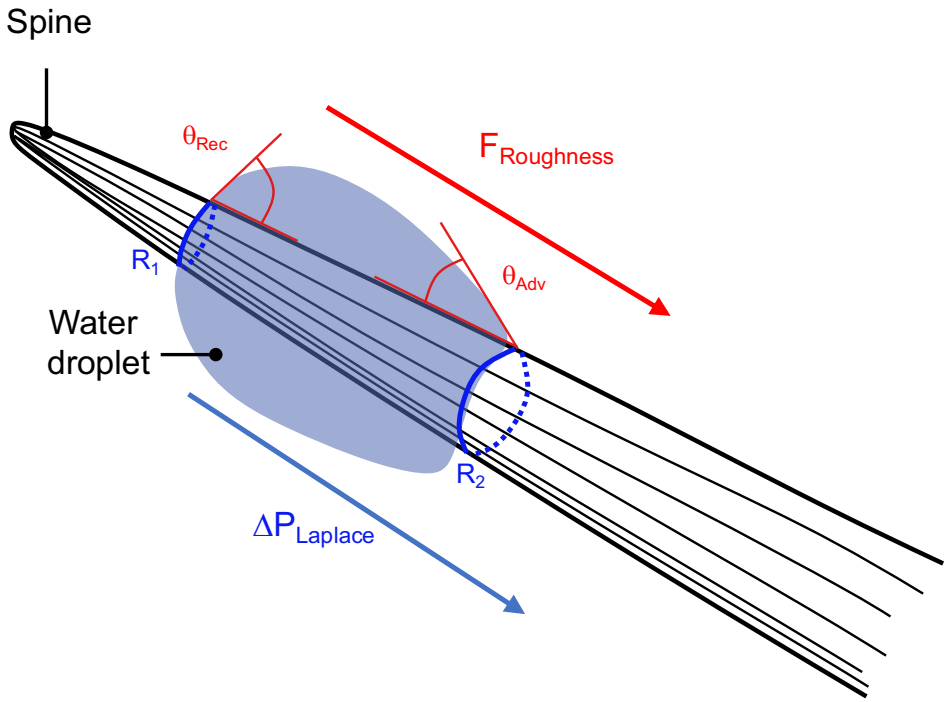

Figure 1.4: Unidirectional Water Transport Mechanism of a Cactus Spine. Schematic illustration of the water droplet transport on a cactus spine. The droplet is guided by microgrooves and transported by LAPLACE pressure (blue) with two curvature radii R_1 and R_2 as well as a difference in wettability (red). The water droplet on the cactus spine has a receding and advancing contact angles Θ_{Rec} and Θ_{Adv}.

In the context of fog harvesting, two distinct spine types are commonly observed in cacti plants: Those with and without barbs. In general, barbs describe the hook-like projections along a cacti spine. Among the cactus species with barbs, *Opuntia microdasys* is the most widely researched in the context of water transport (cf. Figure 1.5 A, B). Although there are other cacti, such as *Mammillaria neocoronaria*, that feature smooth spines, they are still capable of transporting water droplets unidirectionally (cf. Figure 1.5 C, D). Recent studies by Ju and Bai *et al.* have demonstrated that the cactus *O. microdasys*, with its barbs oriented at the tip and microgrooves aligned along the spine, can effectively transport water droplets at a rate of ~12 µm s^{-1}. [31] In contrast, Malik *et al.* have shown that dew harvesting is optimized in cacti with hydrophilic surfaces and microgrooves, while those with hydrophobic surfaces and barbs show decreased water nucleation. [48] Additionally, Guo *et al.* observed that cacti spines with microgrooves facilitate the channelling of water droplets. [38]

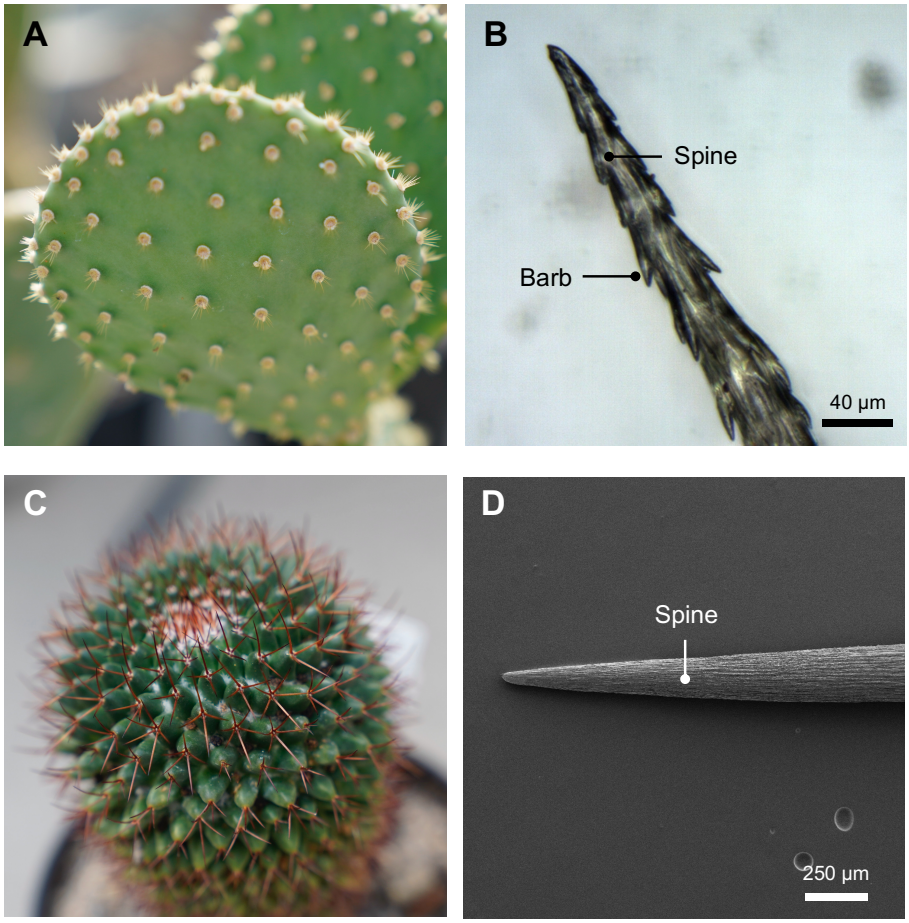

Figure 1.5: The Morphology of Cacti Spines with and without barbs. (**A**) and (**C**) Photography of cacti species *Opuntia microdasys* and *Mammillaria neocoronaria* (**C**) shows an optical microscopy image of the spine of *O. microdasys* with barb and (**D**) scanning electron microscopy image of *M. neocoronaria* with smooth cacti spine morphology.

In general, there are many publications that show the fabrication of cacti spine-inspired structures. An interesting fabrication strategy with high experimental flexibility was proposed by S. Yi *et al* (cf. Figure 1.6).[49] This method utilized a magnetorheological drawing lithography (MRDL) method that resulted in spines with and without oriented microbarbs. The fabricated cactus-inspired conical spines demonstrated efficient coalescence and transport of fog droplets.

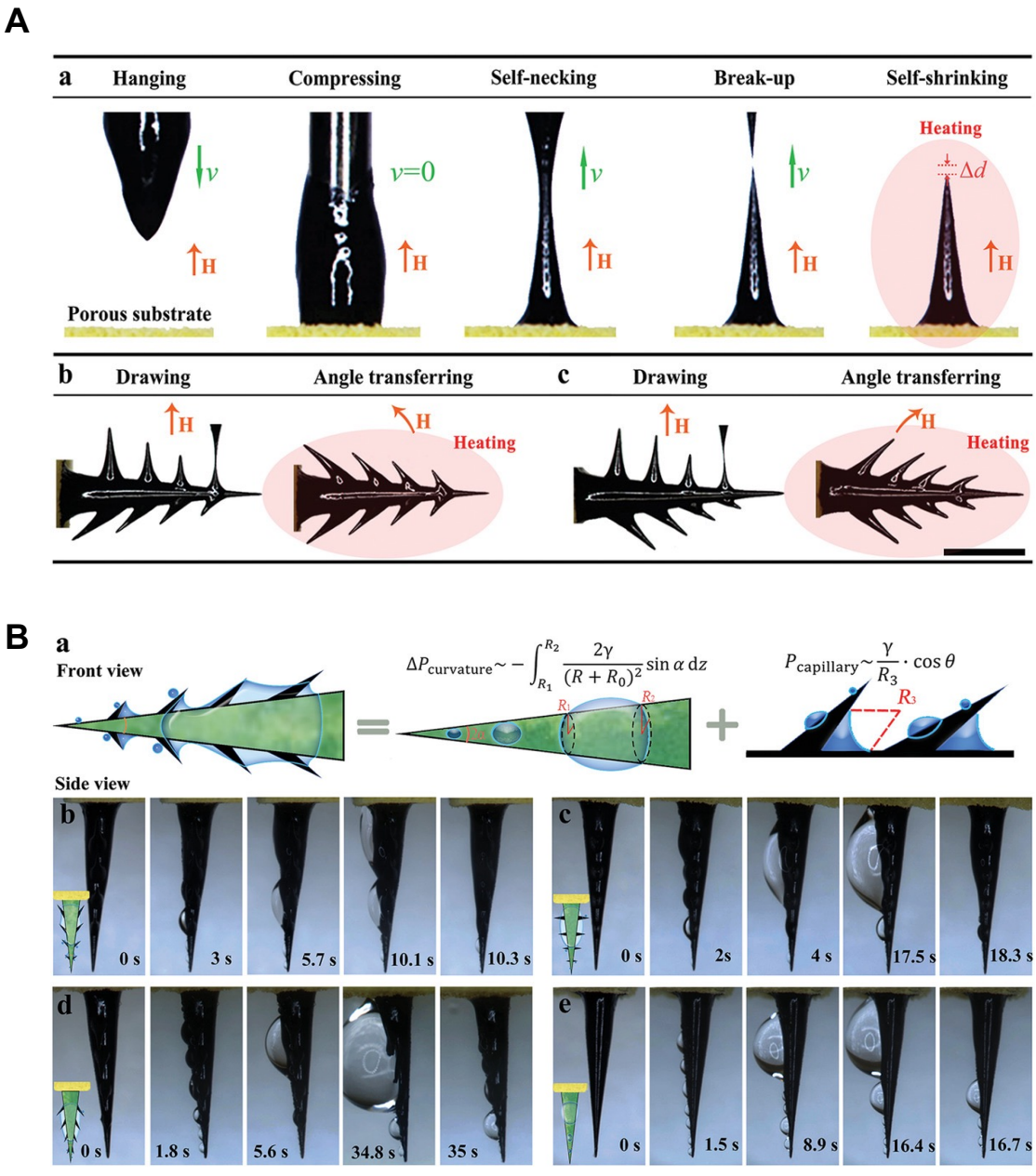

Figure 1.6: Fabrication of artificial cacti spines with barbs by magnetorheological drawing lithography. (**A**) Fabrication scheme of cacti spines with and without barbs. (**B**) Overview of the water transport mechanism of water droplets on the artificial cactus spine. Reprinted with permission from [49].

Additionally, the authors showed that conical spines with backward-facing microbarbs exhibited the most efficient unidirectional transport of water drops due to the synergisitc effect of LAPLACE pressure difference and capillary pressure. This efficient transport resulted in faster fog harvesting rates and higher fog collection efficiency compared to spines without microbarbs. The backward-facing microbarbs promoted the unidirectional movement of water droplets and enhanced the fog deposition rate further. The authors suggested that the proposed strategy of cactus-inspired conical spines with oriented microbarbs on a superhydrophilic substrate holds great potential for high-efficiency fog harvesting applications.

Dandelion Seed

Dandelions (*Taraxacum*) are herbaceous plants commonly found in the northern hemisphere. The genus consists of several different species, while the common Dandelion (*T. officinale*) has been introduced almost all over the world. The development of the Dandelion consists of several stages, starting from the flowering stage (cf. Figure 1.7 A, B), which transitions into the seed stage (cf. Figure 1.7 C). In general, the flowering stage starts early in the year, being one of the first flowers in the spring. After the flowering phase, the Dandelion flower falls off, and a fluffy white ball of several single parachute seeds develops. [50,51]

Figure 1.7: Photography of Dandelion flowers. (**A**) shows a photograph of a Dandelion flower field, while (**B**) shows a close-up recording of a Dandelion flower and (**C**) of a developed Dandelion flower seed.

On one flower, multiple seeds are loosely connected to the stem of the flower (cf. Figure 1.8). The Dandelion seeds consist of a branched filament head – also referred to as a pappus. The pappus is attached to a stem, which connects the pappus with the seed (cf. Figure 1.11 B, C). The pappus functions as a parachute, allowing the seeds to be carried by the wind to new locations, even over a distance of several kilometers. Combining the early flowering stage with the efficient seed dispersal strategy allows the Dandelion flower an evolutionary advantage. [50,51]

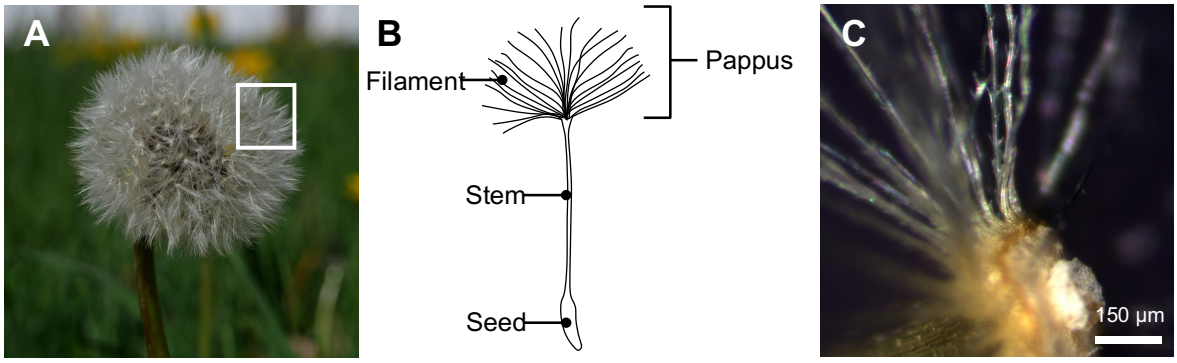

Figure 1.8: The Dandelion Seed. (**A**) optical photography of a developed Dandelion seed flower. (**B**) shows a schematic representation of a single Dandelion seed with the pappus consisting of multiple filaments, the stem, and the seed. (**C**) shows an optical microscopy image of the Dandelion seed pappus.

Besides the wind distribution feature, Y. L. Han *et al.* showed that Dandelion seeds are able to capture water droplets within the pappi. [52] In their work, the authors explored a distinctive wetting behavior found in Dandelion seeds, specifically within their pappus. When the seeds were immersed and then pulled out of the water, the pappus encapsulated a water droplet. Notably, this wetting behavior was not limited to water, as it was also observed with oil, indicating the versatility of the Dandelion seed in interacting with different liquids (cf. Figure 1.9 A). The interaction was further simulated, and a theoretical model was proposed (cf. Figure 1.9 B).

Assuming the filaments can be modeled as a beam according to the classical beam theory, the deformation during liquid uptake is given by the curvature $1/\rho$, the bending moment M, the YOUNG'S modulus E, and the moment of inertia I.:

$$\frac{1}{\rho} = \frac{M}{EI} \tag{1.9}$$

I can be expressed by the diameter of the filament *d:*

$$I = \frac{\pi d^4}{64}$$

(1.10)

Once a liquid droplet is captured by the pappus, the surface tension balances with the fiber bending moment, leading to the maximal surface tension σ, where the droplet is held in place by the pappus:

$$\sigma \geq \max\left\{\left[\frac{EI}{2(\gamma(s)\sin\Theta + x(s)\cos\ \Theta(s))} \cdot \frac{\partial^2\delta(s)}{\partial s^2}\right]\right\}$$

(1.11)

Where δ is the angle between the fiber and the horizontal axis, and *s* the profile of the fiber as schematically depicted in Figure 1.9 C.

The authors concluded that the proposed mechanism for water capture involves the interplay between the elasticity of the fibers and the forces exceeded by the surface tension of water.

As shown by Hale *et al.,* one reason for this unusual interaction may be due to the improved water channeling of the pappus to the seed. In their work, it was shown that seeds without intact pappus exhibited significantly decreased germination rates compared to seeds with intact pappus. It was hypothesized that the intact pappus facilitates water entry to the seed and thus gives the germinating seed an improved water access. [53]

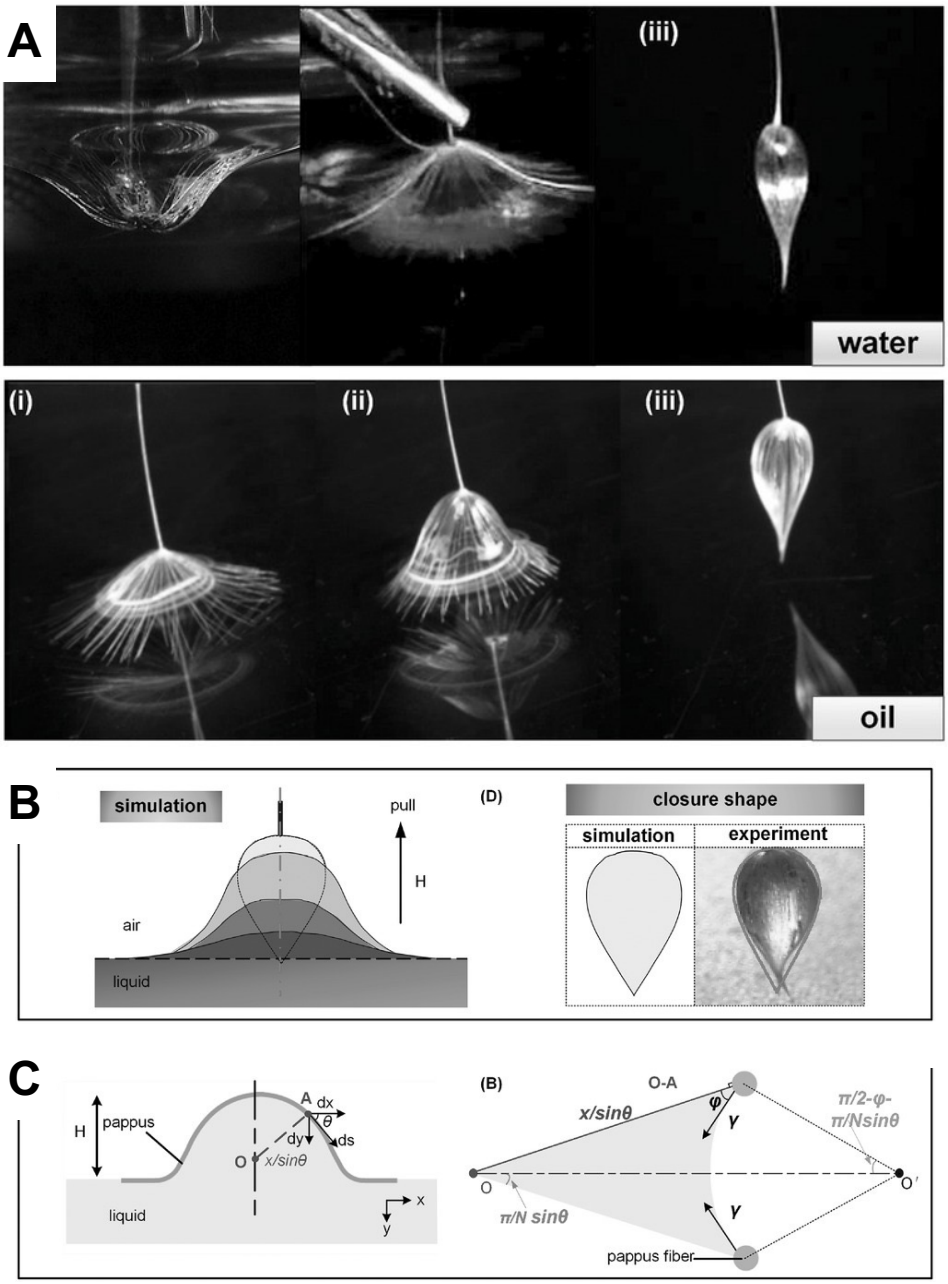

Figure 1.9: The interaction of Dandelion seeds with water and oil. (**A**) shows the interaction of a Dandelion seed with water and (**B**) with oil. (**C**) gives a schematic overview of the theoretical framework of the interaction with a liquid. Reprinted with permission from [52].

Electrostatic Flocking Technique

The above-discussed fog harvesting species often depend on fiber-based morphologies. Thus, in the pursuit of developing bioinspired and biomimetic fog harvesting devices, fiber-based coating techniques may be a promising approach. In general, coating techniques are an essential aspect of modern day-to-day life, including applications of corrosion resistance, [54–56] anti-fouling, [57–59] or electric insulation [60–62] used in electronics, medicine, automotive, and marine applications, as well as many more. [63] While the advancements during the Industrial Revolution accelerated science and technology, humankind utilized coatings long before. It is well established that coatings and painting techniques have accompanied humans throughout the course of history, ranging, for example, from cave paintings at the beginning of civilization to the design of pilled drugs in the Middle Ages. [64–66] Nowadays, the field of coatings includes complex techniques from physical [67,68] or chemical vapor deposition [69,70] (PVD, CVD) to spray- or dip-coating. [71] Noteworthy, electrostatic-based coating techniques are generally widely utilized in today's industrial landscape due to the renunciation of solvents, ease of use, and cost-efficiency. [72,73] One of the most prominent coating techniques is powder coating. [74] This method involves the application of polymer microparticles to a substrate using a combination of pressured air and electrostatic forces. Upon curing and sintering, a stable and conformal coating is obtained. [74] A close relative to electrostatic powder coating is the electrostatic flocking technique. Instead of using polymer microparticles, polymer microfibers, also referred to as flock fibers, are applied to the substrate. A unique caveat of this technique is the vertical fiber orientation due to the utilization of an electrostatic field. The resulting micrograss-like polymer fiber morphology is widely used in a plethora of different applications. [75–89]

The underlying technique of flocking was refined at the end of the last century by including modern polymer materials and electrostatic generators in the flocking process. [90] As outlined by Stig W. Bolgen, the general electrostatic flocking process consists of six subsequent steps. [91] 1.) If necessary, the substrate is pretreated to obtain a clean surface. 2.) A thin adhesive film is applied to the substrate. According to established flock fiber providers, the thickness of the adhesive layer should be ~1/10th of the flock fiber length. [92–94] 3.) The flock fibers are placed on an electrode, and the ground is attached to the adhesive layer of the substrate.

After applying the electrostatic field, the flock fibers are accelerated toward the grounded substrate and anchored according to the electrostatic field lines in the adhesive layer (cf. Figure 10 A). As schematically depicted in Figure 10 B, for a two-dimensional flat substrate, the flock fibers are anchored vertically. 4.) A preliminary cleaning step to remove loose and non-oriented flock fibers. 5.) The adhesive film is cured to provide sufficient anchoring of the flock fibers to the substrate. 6.) A final cleaning step is used to remove non-sufficiently anchored flock fibers and to prevent flock fiber leaching during the handling of the substrate.

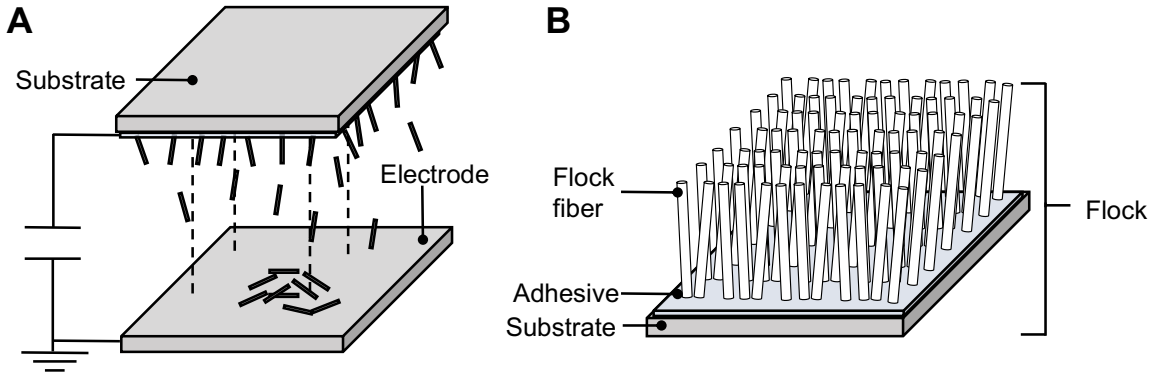

Figure 1.10: Schematic representation of Electrostatic Flocking. (**A**) shows the electrostatic flocking process in a bottom-to-top (BT) setup. The ground is generally attached to the substrate, while the loose flock fibers are charged by an electrostatic field. Due to the electrostatic charging, the flock fibers are accelerated toward the substrate and anchored by an adhesive film. (**B**) gives the schematic structure of a flocked substrate consisting of single flock fibers attached to a two-dimensional substrate with an adhesive layer.

In general, the electrostatic flocking technique involves three main components: Flock fibers, adhesives, and the substrate to be coated. While most substrates can be coated, the choice of flock fibers and adhesive materials is more restricted. The fiber materials consist of polymeric fiber materials such as polyamide (PA), viscose, polyethylene terephthalate (PET), polyacrylonitrile (PAN), or polypropylene (PP), while PA, PET, and viscose are most commonly used in industrial applications. [90]

The choice of adhesive depends on the substrate, where the adhesion between the surface of the substrate and the anchored flock fibers has to be sufficient. Commercial adhesives can be classified as solvent- and water-based adhesives. Solvent-based adhesives provide longer pot life and are suitable for larger substrates. On the other hand, water-based adhesives are generally preferred due to their environmental and health aspects.

Almost all substrates can be coated by the flocking process. However, issues may occur for three-dimensional cavities: Due to electrostatic shielding effects, three-dimensional geometries are difficult to coat by conventional electrostatic flocking. To overcome this problem, electrostatic-pneumatic flocking was developed. By additionally employing pressured air, the flock fibers are forced into the three-dimensional cavities. While pneumatic electrostatic flocking ensures an even flock fiber coating, the orientation is generally decreased compared to conventional electrostatic flocking. [90]

The conventional electrostatic flocking process can be further classified into two different setups: Top-to-bottom (TB) and bottom-to-top (BT). Depending on the specific setup, many different case-specific devices are available. In a TB setup, the flock fibers are stored in a fiber reservoir, where the substrate is placed underneath the reservoir. In addition to the electrostatic force, a pneumatic or mechanical feed may be added to the fiber reservoir to ensure a steady flock fiber supply. In a BT setup, the location of the flock fiber reservoir and substrate is changed. [88,95]

Since electrostatic flocking relies on electrostatic forces, the application of electrostatic charge to the fibers is an essential part of the flocking process. While there are also setups utilizing an alternating current (AC), direct currents (DC) are preferred due to the improved safety aspects. For the simplified DC case, where a uniform electrode, constant flock fiber dimensions, and the omitting of gravitational forces are assumed, the electrostatic flocking process can be described by the amount of charge accepted by an individual fiber q during the contact time with the electrode t. [88,95]

$$q = q_0[1 - e^{-t/\tau}]$$

(1.12)

Where q_0 corresponds to the theoretical maximal Coulomb charges accepted and τ to the relaxation time of the flock fibers. The relaxation time is characterized by the dielectric constant of the fiber material ε_r, the permittivity of free space ε_0, and the conductivity of the fiber β [88,95]

$$\tau = \frac{\varepsilon_0 \varepsilon_r}{\beta}$$

(1.13)

The theoretical maximal Coulomb charge q_0 is:

$$q_0 = \frac{\pi \epsilon_0 l^2 E}{\ln\left(4 \cdot \frac{l}{d}\right) - 1}$$

(1.14)

Where E corresponds to the electric field strength, l to the fiber length, and d to the fiber diameter. [88,95]

According to Equations (1.11) to (1.13), the charging time required to establish sufficient acceleration is inversely proportional to the conductivity of the fiber. Polymeric materials, which are most commonly used as a flock fiber material, are known to have a low electric conductivity. [96] Therefore, fiber finishes are necessary to increase the conductivity and the overall flocking properties. These finishes generally consist of surfactant treatment in combination with different inorganic salts and metal oxides. [97,98]

Besides electrostatic properties, it is also necessary to consider aerodynamic factors when describing the flocking process. The air drag coefficient K is described by the fiber drag coefficient C_0, the specific density ρ of air, the kinematic viscosity of air γ_L, the flock fiber diameter d_F, and the flock fiber length l_F: [88,95]

$$K = \frac{c_0 \pi \rho (\gamma_L d_F)^{0.5} l_F}{2}$$

(1.15)

The overall acceleration of a single flock fiber in the electric field a is described by its mass m, the airflow v, the electric field E, the gravitational acceleration g, and the air drag coefficient K: [88,95]

$$ma = qE - Kv + mg$$

(1.16)

During flocking, the electrostatic greatly exceeds the gravitational forces, allowing flock fiber acceleration even against gravity. [88,95]

In conclusion, electrostatic flocking is a highly versatile and unique coating technique. Traditionally, this technique has been extensively utilized in the automotive or textile industry. However, in recent years, electrostatic flocking has also gained traction in functional applications developed by the academic community. In general, the scientific literature may be classified into four major topics: Thermal insulation materials [89,99], tissue engineering [85–88], electronics [80–82,100], and water transport. [83,84]

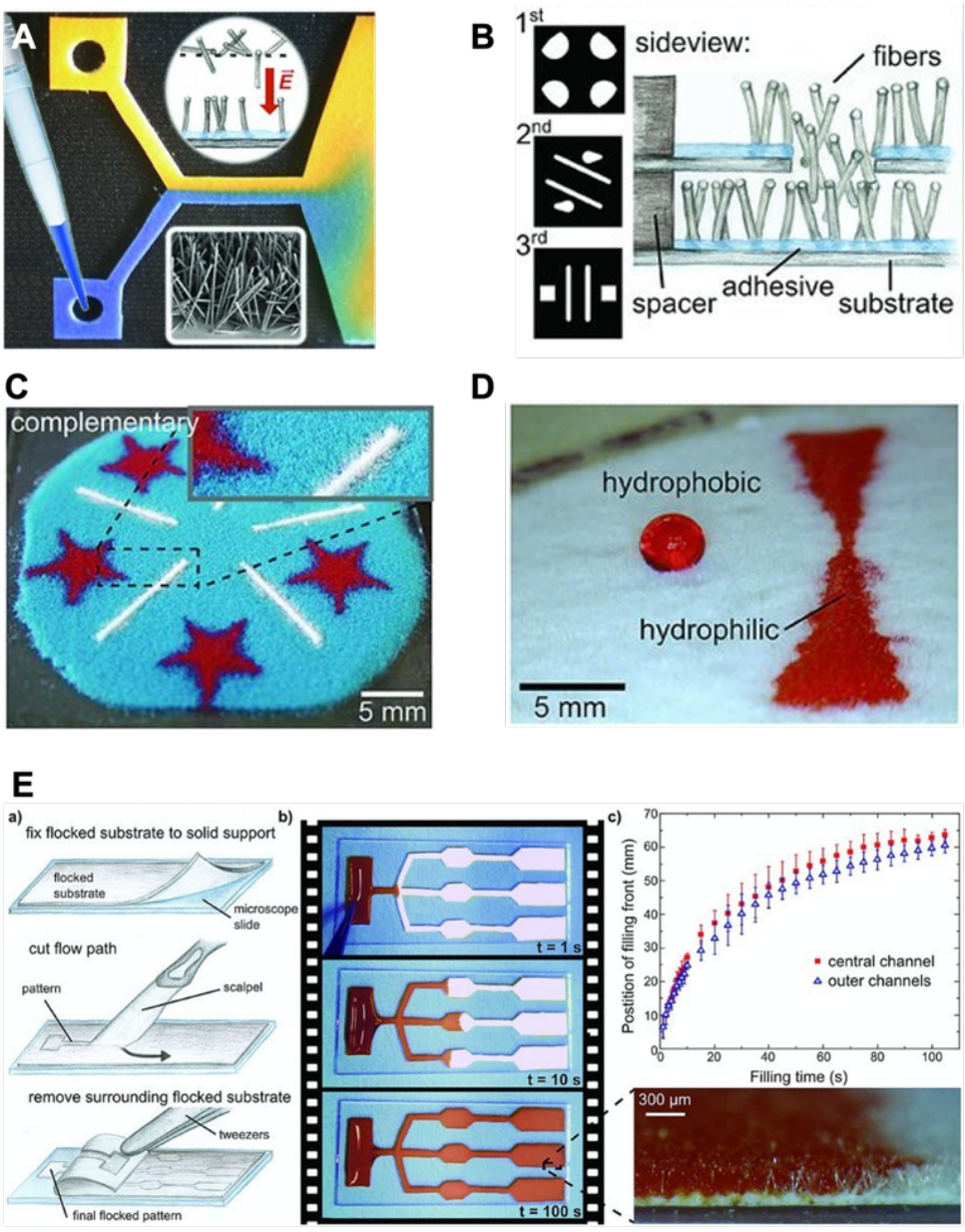

Figure 1.11: Flock-based microfluidic system. (**A**, **B**) Fabrication of a flock-based microfluidic device. (**C**, **D**) By utilizing a mask, structural and functional patterning was possible. (**E**) Schematic fabrication scheme and wicking properties of the microfluid device. Reprinted with permission from [83].

An especially noteworthy publication is the one by Hitzbleck *et al.* [83] The study explored the potential of electrostatically flocked polymer microfibers for the fabrication of flexible and cost-effective microfluidic devices (cf. Figure 1.11 A). The lateral capillary-driven fluid flow was utilized to design two- as well as three-dimensional microfluidic devices (cf. Figure 1.11 B). Additionally, the study investigated the use of a mask to precisely create flocked patterns (cf. Figure 1.11 C). This technique allowed for not only structural patterning by using flock fibers with different lengths and colors, but also patterning of wettability by utilizing hydrophilic and hydrophobic flock fibers (cf. Figure 1.11 D). Furthermore, the fabrication of microfluidic channels was investigated, and the wicking properties were characterized (cf. Figure 1.11 E). The authors concluded that electrostatic flocking of microfibers provides a cost-effective and versatile method for creating microfluidic channels.

Based on the findings of Hitzbleck *et al*., the unique water interactions of flocked substrates were further utilized by Y. Guo *et al*. toward the development of a solar-based evaporator for the desalination of seawater. [84] Motivated by the pressing issue of global water scarcity, the research of Y. Guo *et al.* presented the development of a solar-powered All-in-One Evaporator (AE) for the sustainable desalination of water. The AE device consisted of two different types of flock fibers on its top and bottom surfaces, as depicted in Figure 1.12 A. The top part was covered with black hydrophilic flock fibers, while the bottom side was equipped with hydrophobic flock fibers. This design allowed the top part to absorb water continuously. Additionally, the black color of the flock fibers absorbed light efficiently and transferred heat to the trapped water. This led to a continuous evaporation of the absorbed water. On the opposite side of the sample, hydrophobic flocks formed an air layer and acted as a thermal insulator to reduce heat loss to bulk water. The integration of these features allowed the AE to achieve an evaporation rate of 1.32 $kg\,m^{-2}\,h^{-1}$ for pure water and 1.10 $kg\,m^{-2}\,h^{-1}$ for seawater (cf. Figure 1.12 B). One notable aspect of the AE was its resistance to salt accumulation during evaporation and stability in the seawater analogon. The diffusion effect prevented salt crystals from accumulating at the irradiated surface, demonstrating the system's reliability for long-term use in seawater (cf. Figure 1.3 C). The authors showed that the fabricated device has mechanical durability, high evaporation rates, chemical stability, and resistance to salt accumulation.

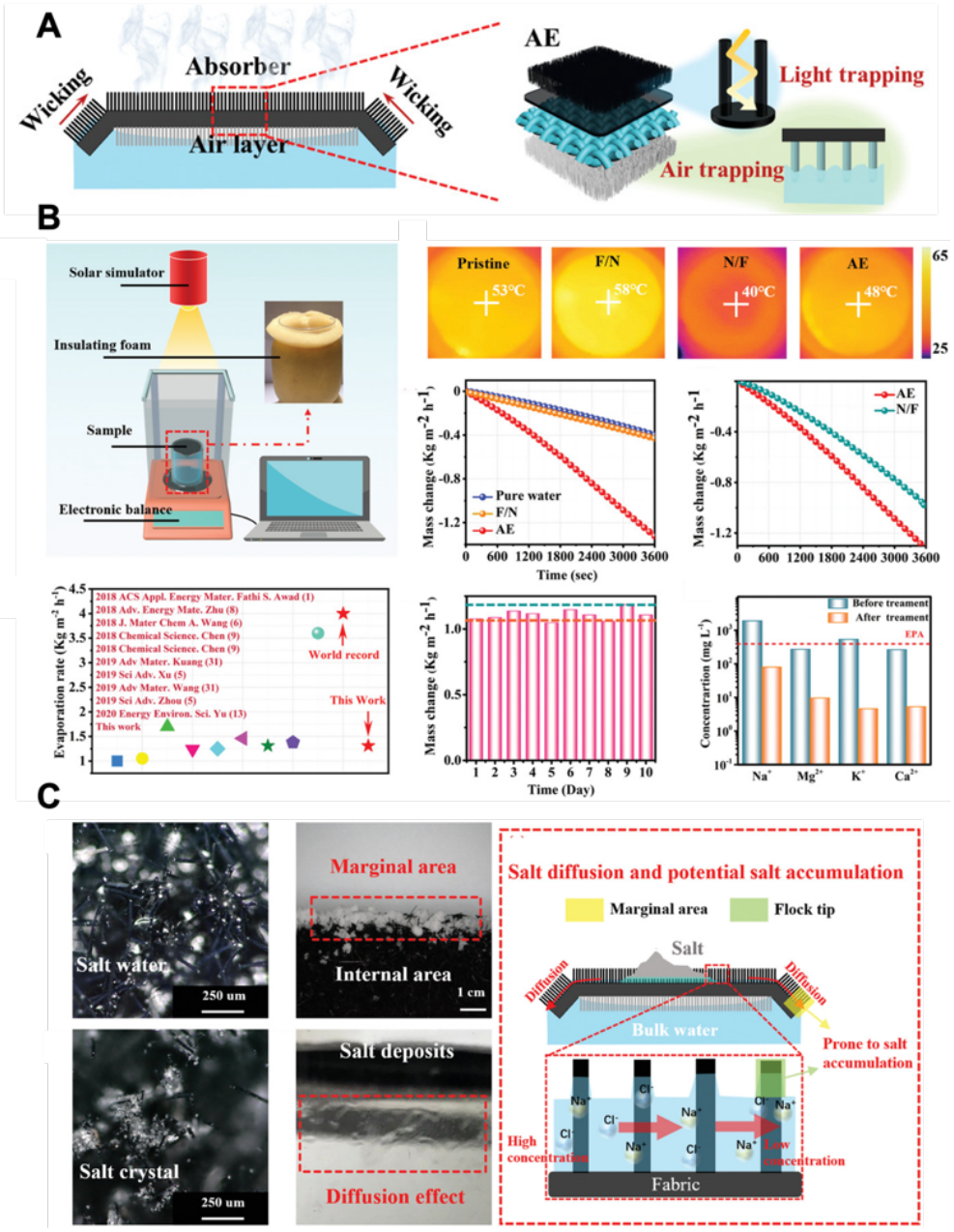

Figure 1.12: Flock-based water evaporation system. (**A**) A schematic depiction of the solar evaporation system with the underlying principle. (**B**) shows the quantification experiments and (**C**) the principle of resistance against salt accumulation. Reprinted with permission from [84].

Interestingly, the specific design of the AE's device by Y. Guo *et al.* mimics the air-trapping effect observed in nature, contributing to its self-floating capability. This overall trend of adapting or mimicking biological role models is often observed in the field of electrostatic flocking. [77,101,102]

2. Aim of the Thesis

The thesis aims to achieve two major objectives: First, the detailed interaction of the flocked substrates with water and fog is investigated toward the development of a fog harvesting device. Second, the thesis focuses on expanding the field of functional flock-based systems and illustrating its potential as an industrially established but low-cost coating technique. These two aims are expected to be achieved simultaneously by focusing on bioinspired and biomimetic concepts. In general, bioinspired and biomimetic concepts are known to efficiently condense and collect water due to the specific adaption over the course of evolution. However, bioinspired and biomimetic structures are challenging to implement due to hierarchical and complex structures. Therefore, the successful adaptation of bioinspired and biomimetic flock-based systems is assumed to have efficient fog interaction and would illustrate the potential of the electrostatic flocking technique as well.

The aims of the thesis are addressed in four chapters (cf. Figure 2.1). In the first chapter, the general interaction of the flocked substrate with water and fog is investigated. Based on these findings, three different bioinspired and biomimetic devices are designed. In the second chapter, a flock-based approach to obtain a structure similar to the Namib desert beetle is achieved by a simple stamping technique. The proposed technique combines electrospinning to fabricate a hydrophobic membrane and electrostatic flocking to selectively apply hydrophilic flock fibers. For a proof of concept, the interaction between the membrane and fog is investigated.

In the third chapter, the complex and hierarchical morphology of a cactus spine is rebuilt by an evaporation-guided molecular self-assembly mechanism of benzenetriamides (BTAs) molecules. A detailed self-assembly protocol is proposed and the self-assembly mechanism toward BTA spines is examined. Here, different BTA molecules and flocked substrates are screened to establish a suitable candidate for the fabrication of supramolecular spines. Furthermore, the interaction of fog with the supramolecular spines is investigated and characterized.

In the final and fourth chapter, microfibers with a structure similar to Dandelion seeds are obtained by a sequential flocking approach. Different flock fibers are examined, and the device's interaction with fog and dew is investigated and characterized. Finally, a fog harvesting device is designed and the fog yields are quantified.

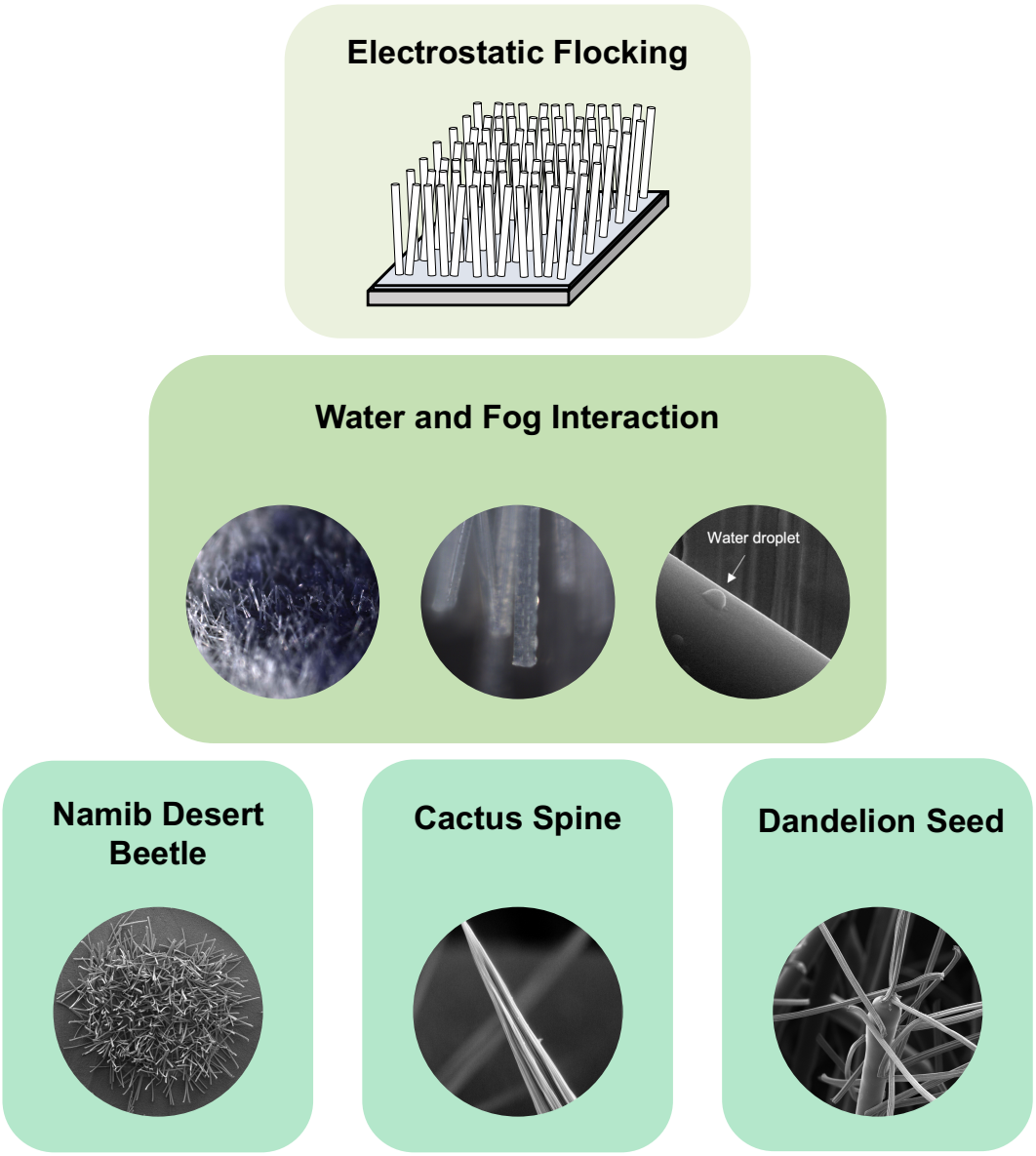

Figure 2.1: Schematic overview of the thesis. The thesis investigates the electrostatic flocking technique and the development of a fog-harvesting device utilizing bioinspired and biomimetic concepts. In a preliminary study, the electrostatic flocking technique, as well as the interaction with water and fog, is investigated. Based on these findings, three bioinspired and biomimetic concepts were implemented. In the second chapter, the patterned structure of the Namib desert beetle, in the third chapter, the structure of cacti spine, and in the fourth and final chapter, the complex structure of a Dandelion seed are adapted.

3. Results and Discussion

3.1 Interaction of Flocked Substrates with Water

General Properties of Flocked Substrates

In the literature, the definitions of flock, flocks, and flock fibers are not clearly defined and are often used interchangeably. In general, flocks and flock fiber refer to the single polymer microfiber, while the flock is associated with the flocked substrate. However, this definition may still be confusing. Therefore, in the scope of the thesis, a consistent definition is established: Flock fibers refer to single polymer microfibers. The application of the flock fibers to a substrate results in a flocked substrate.

In the thesis, two different flock fiber materials were used: Polyamide (PA) and viscose. PA is a polymer with a high E-modulus and a more hydrophobic surface. [103] On the other hand, viscose has a lower E-modulus and is characterized as a hydrophilic material. [104] For PA, a contact angle of ~ 74 deg. is reported, [105] while viscose is more hydrophilic with a contact angle of ~50 deg. [106] Due to the low E-modulus, viscose flock fibers usually deform after the application of a mechanical load. In contrast, PA flock fibers recover after load application. An overview of the flock fibers used in this thesis is listed in Table 3.1.1. The dimensions of the flock fibers are abbreviated with an Arabic numeral, where smaller numerals correspond to smaller dimensions.

Table 3.1.1: Overview of the flock fibers used in this thesis. The flock fibers are classified according to their material composition and dimensions.

Material	Diameter / dtex	Length / mm	Abbreviation
Polyamide (PA)	3.3	0.5	PA2
	3.3	1.0	PA2-1
	22	2.0	PA3
	44	6.0	PA4
Viscose	1.7	0.5	V1
	3.3	0.5	V2
	5.6	1.0	V3

Additionally to the flock fiber dimensions, the PA and viscose flock fibers can be distinguished by their surface morphology. In Figure 3.1.1, PA (3.1.1 A, 3.1.1 B) and viscose flock fibers (3.1.1 C, 3.1.1 D) are compared in their surface morphology and cryogenically cut cross-section view.

The PA flock fiber shows a smooth surface with a solid cross-section. The viscose flock fiber, on the other hand, has a grooved surface where the groves are oriented parallel to the fiber axis. Additionally, in the cross-section view, the viscose flock fiber shows a more porous morphology compared to the PA flock fiber.

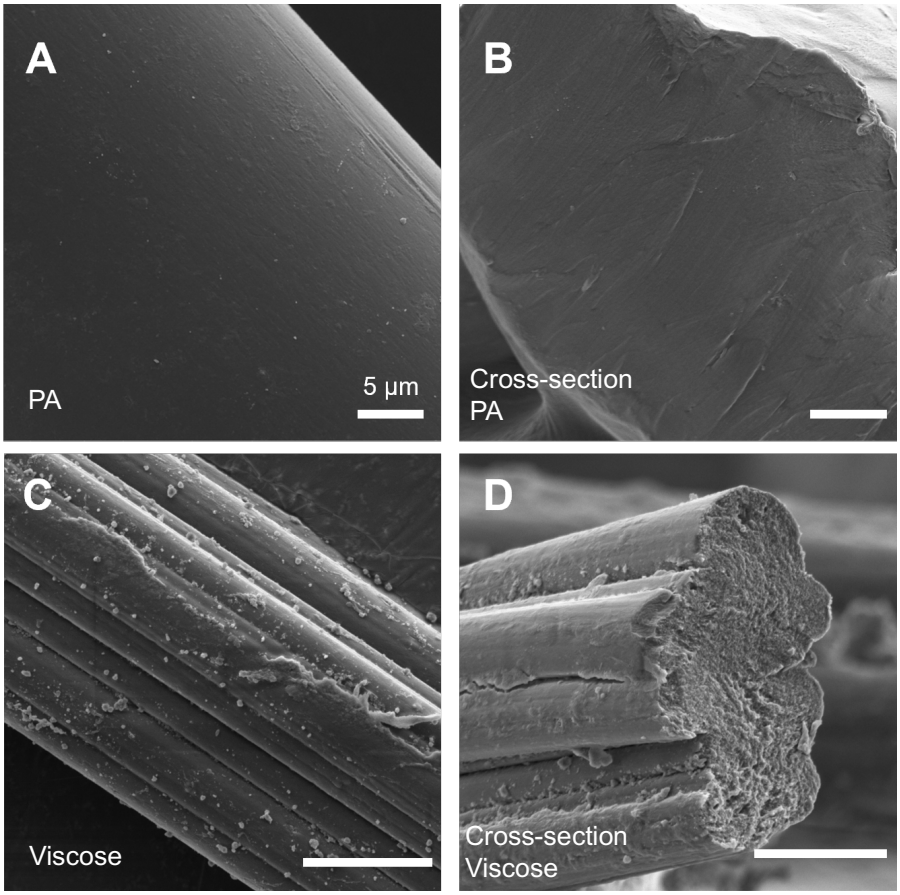

Figure 3.1.1: Scanning electron microscopy micrographs of PA and Viscose flock fibers. (**A**, **C**) shows the top-view of PA3 (22 dtex/2mm)- and viscose V2 (3.3 dtex/0.5 mm) flock fibers. (**B**, **D**) gives the cryogenically cut cross-section view of the respective flock fiber. The scale bars in (**B**-**D**) correspond to 5 µm.

Despite the morphological difference between PA and viscose flock fiber, the flocked substrate of the respective PA and viscose flock fiber shows similar characteristics (cf. Figure 3.1.2). Both the PA and viscose flock fibers are oriented perpendicular to the substrate. As shown in Figure 3.1.2 A and Figure 3.1.2 C, the longer the flock fibers used for preparing the flocked substrate, the larger the space between the flock fibers (3.1.2 A *vs.* 3.1.2 C) and, therefore, the larger the pore size. On the other hand, shorter and thinner flock fibers result in higher fiber density and, thus, a higher porosity.

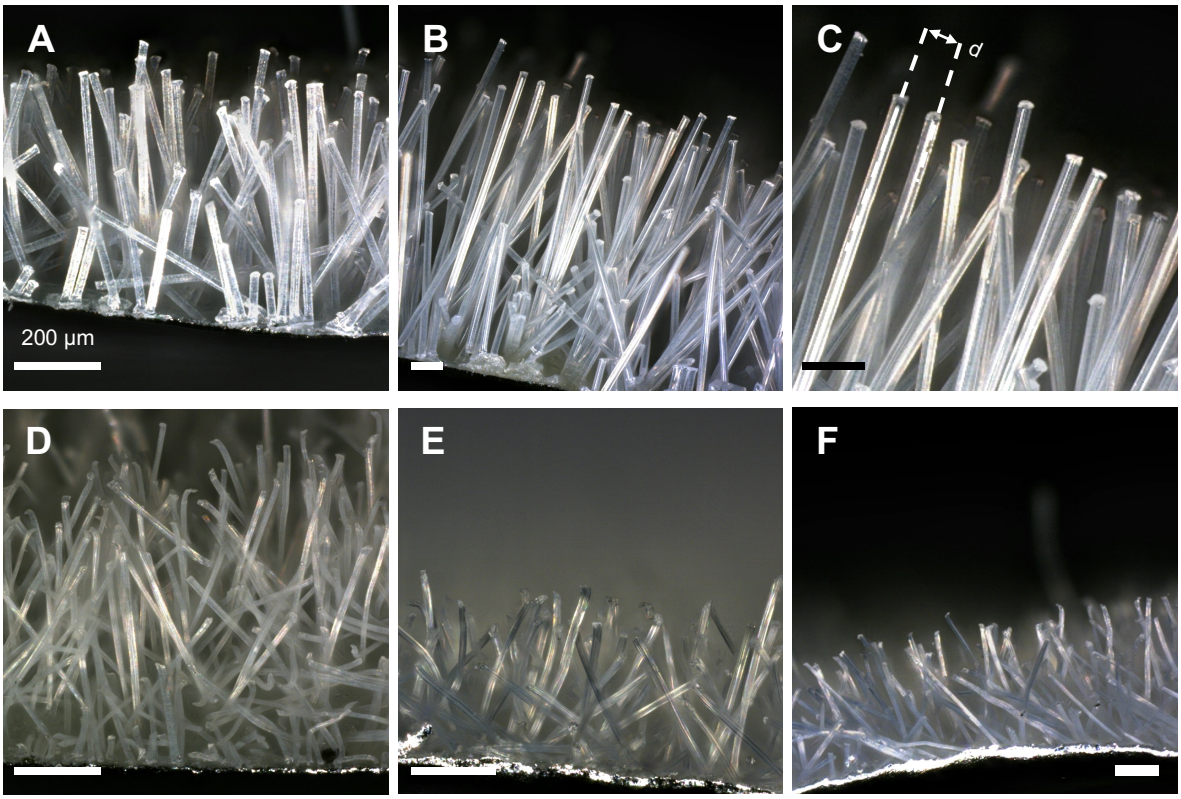

Figure 3.1.2: Optical microscopy side-view micrographs of flocked substrates. (**A**, **B**) show the flocked substrates using a PA2 and PA3 flock fiber, respectively. (**C**) shows (**B**) at a higher magnification with the exemplary annotated flock fiber distance *d*. (**D**, **F**) show V1, V2, and V3 flocked substrates. The scale bars in (**B**-**F**) correspond to 200 µm.

In general, a flocked substrate is characterized by the orientation α and density ρ. The density is measured gravimetrical by comparing the mass before and after flock- and adhesive application:

$$\rho = \frac{\Delta m}{A_0} = \frac{m_1 - m_0}{A_0} \tag{3.1.1}$$

Where A_0 corresponds to the projected area of the substrate, Δm to the mass difference before and after flock application, and m_1 and m_0 of the initial mass and the mass after flock fiber application.

The orientation is obtained by the side view. In the scope of the thesis, the orientation is defined as the following:

$$0\ \text{deg} < \alpha < 180\ \text{deg} \tag{3.1.2}$$

Where angles of 0 deg and 180 deg correspond to an orientation parallel to the substrate's surface and 90 deg to a perpendicular orientation.

A summary of the orientation and density parameters of the investigated flocked substrates is given in Table 3.1.2. All flock fibers used in this thesis result in flocked substrates with fiber orientation of ~90 deg, corresponding to a perpendicular orientation relative to the substrate, where the flock fiber orientation of PA and viscose show similar values. Thus, the flock fiber orientation seems to be independent of the flock fiber material.

While the orientation is independent of the flock fiber, the flock density significantly changes with the different flock fiber dimensions. Flock fibers with similar fiber dimensions (cf. Table 3.1.2: PA2 *vs.* V2) result in similar densities. Therefore, a neglectable influence of flock fiber material on flock density is assumed. In contrast, comparing PA2 to PA4, a gradual increase in the density was determined. This is contributed to the increased fiber dimension and, thus, to the increased fiber mass of a single flock fiber. Furthermore, to ensure a sufficient anchoring of the fiber in the adhesive layer, a thicker adhesive layer for longer flock fibers has to be applied. According to the supplier, an adhesive film of roughly 1/10th the fiber length is recommended. [92–94]

Table 3.1.2: Overview of the flocking parameters for different flock fibers. The orientation (α), and density (ρ) were determined for the different flocked substrates. The values in round brackets correspond to the error**.**

Flock Fibers	α / deg	ρ / mg/cm^2
PA2	92(2)	7(1)
PA2-1	91(3)	11(1)
PA3	95(3)	23(2)
PA4	89(2)	36(7)
V1	89(2)	6(1)
V2	92(3)	7(1)
V3	93(3)	9(2)

Interaction of the Flocked Substrates with Water

Knowing the difference in porosity and pore size, the interaction of the flocked substrates with water is investigated next. As shown by M. Hitzbleck *et al.*, [83] the water transport mechanism is mediated by the capillary forces exceeded by the flocked morphology. In the first study, the transport of water parallel to the substrate is characterized. As a first experiment, a droplet of a methylene blue solution in water was exemplarily applied to a V3 flocked substrate. As shown in Figure 3.1.3, a random stepwise spreading of the droplet was observed. The random spreading and stepwise behavior are attributed to the random azimuthal orientation of the flock fiber. Since wicking in the flocked substrate is mediated by capillary forces, the liquid preferably spreads in the direction where flock fibers connect with each other to form a continuous network.

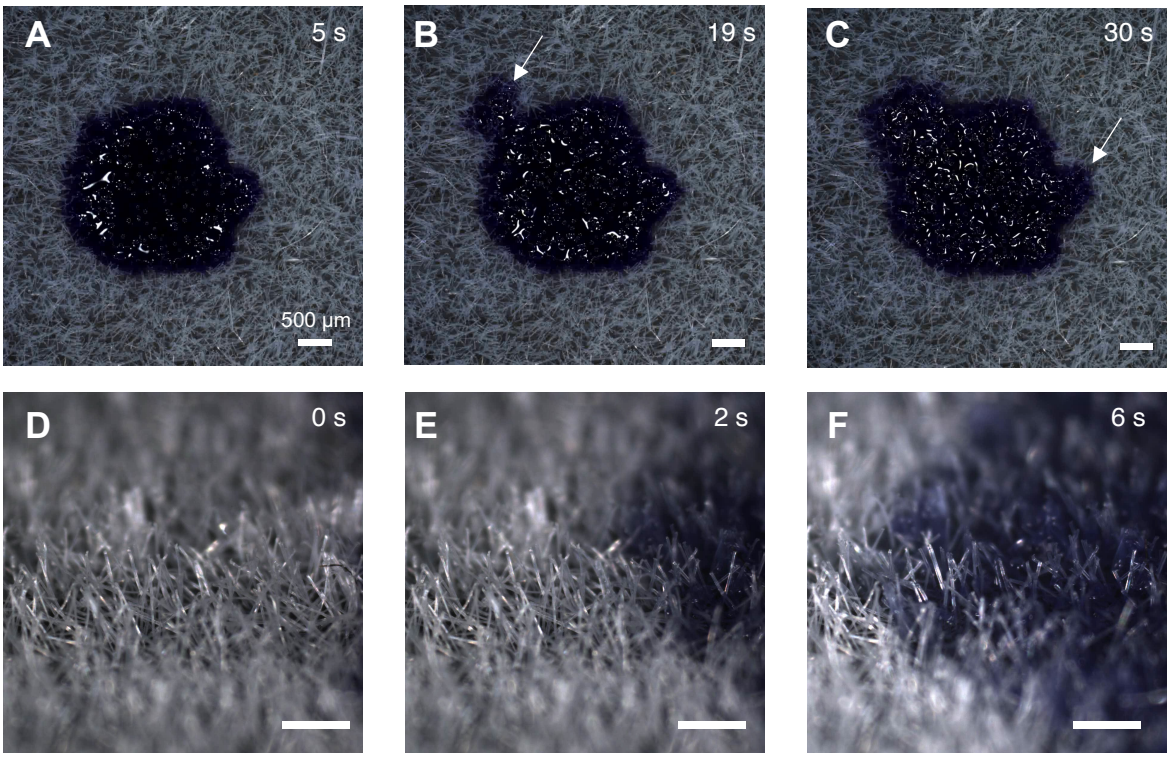

Figure 3.1.3: Optical microscopy of the wicking behavior of a flocked substrate. (**A**-**C**) shows the top view of the V3-flock wetted with methylene blue solution droplet. The white arrows indicate the asymmetric wicking. (**D**-**F**) shows the wicking of the V3 flock in the cross-section view. The scale bars in (**B**-**F**) correspond to 500 µm.

To quantify the wicking in more detail and to investigate the influence of fiber material and dimension, different flock fibers were applied as a 5 mm strip to a glass slide. The flock was then placed in a water reservoir so that the liquid moved against gravity. A schematic depiction of the experimental setup is shown in Figure 3.1.4 A, B. The time required to reach a certain height was recorded with a camera and plotted. The resulting data is fitted by the WASHBURN equation: [107]

$$h_c = \sqrt{\frac{\gamma r \cdot \cos\Theta}{2\eta} \cdot t} = \sqrt{\kappa} \cdot \sqrt{t} \tag{3.1.3}$$

Where h_c corresponds to the capillary rise, γ to the surface tension of the used liquid, r to the porosity, Θ to the contact angle, η to the viscosity, and t to the time required to reach the capillary height h_c. Linearization of the WASHBURN equation is achieved by squaring the data, where the slope corresponds to the fitting parameter κ. Since water is used as a test solvent, the slope is only influenced by the porosity and the contact angle of the respective flock fiber material.

The wicking properties of the viscose-flocked substrates are shown in Figure 3.1.4 C, which agree well with WASHBURN's law. The corresponding slopes compared with the remaining flocked substrates are summarized in Figure 3.1.4 D. Due to the gravitational pull on the wicked liquid, only data with sufficient linearization was used for the fitting. [108] Moreover, it is mentioned in the literature that cellulosic and nylon materials are generally difficult to describe by the WASHBURN equation due to the swelling of the material, which significantly influences the porosity of the material. [109–111] Despite these shortcomings, it was possible to fit the data sufficiently using WASHBURN's equation. Nevertheless, it is pointed out that the dataset was only used to obtain a broad overview of the relative wicking properties and to compare different flocked substrates with each other.

The presented wicking data allows for two conclusions to be drawn. First, the flocked substrates with higher porosity (V1) showed faster wicking than those with smaller porosity (V2, V3). Second, the flocked substrates prepared with viscose flock fibers experienced an overall faster wicking than the ones prepared with PA flock fibers. This is attributed to the more hydrophilic surface of viscose compared to PA. As shown in Equation 3.1.3, the capillary height depends on the wettability of the porous material. Furthermore, it was observed that the viscose flock fibers can flex toward the liquid front due to the decreased flock fiber stiffness and the forces exceeded by the surface tension of water. Thus, viscose flock fibers provide a more continuous network. PA flock fibers, on the other hand, have, compared to viscose flock fibers, an increased fiber stiffness and does not flex toward the waterfront.

Besides wicking-, the water-retaining properties of the different flocked substrates were investigated. Here, the samples were immersed for ~10 s in deionized water and then weighed. By determining the weight difference before (m_0) and after water immersion (m_{H2O}) and dividing it by the sample area (A_0), the water-retaining properties (Q_{H2O}) were quantified according to Equation 3.1.4:

$$Q_{H2O} = \frac{m_{H2O} - m_0}{A_0} \tag{3.1.4}$$

In contrast to the wicking properties, the water-retaining of the flock did not correlate with the wettability of the flocked material (cf. Figure 3.1.4 E), but rather with the size of the pores. The larger the size of the pores, the more water was retained. This behavior suggests that the water retaining is mediated by the capillary interactions of the pore geometry while swelling of the fiber material may be neglectable.

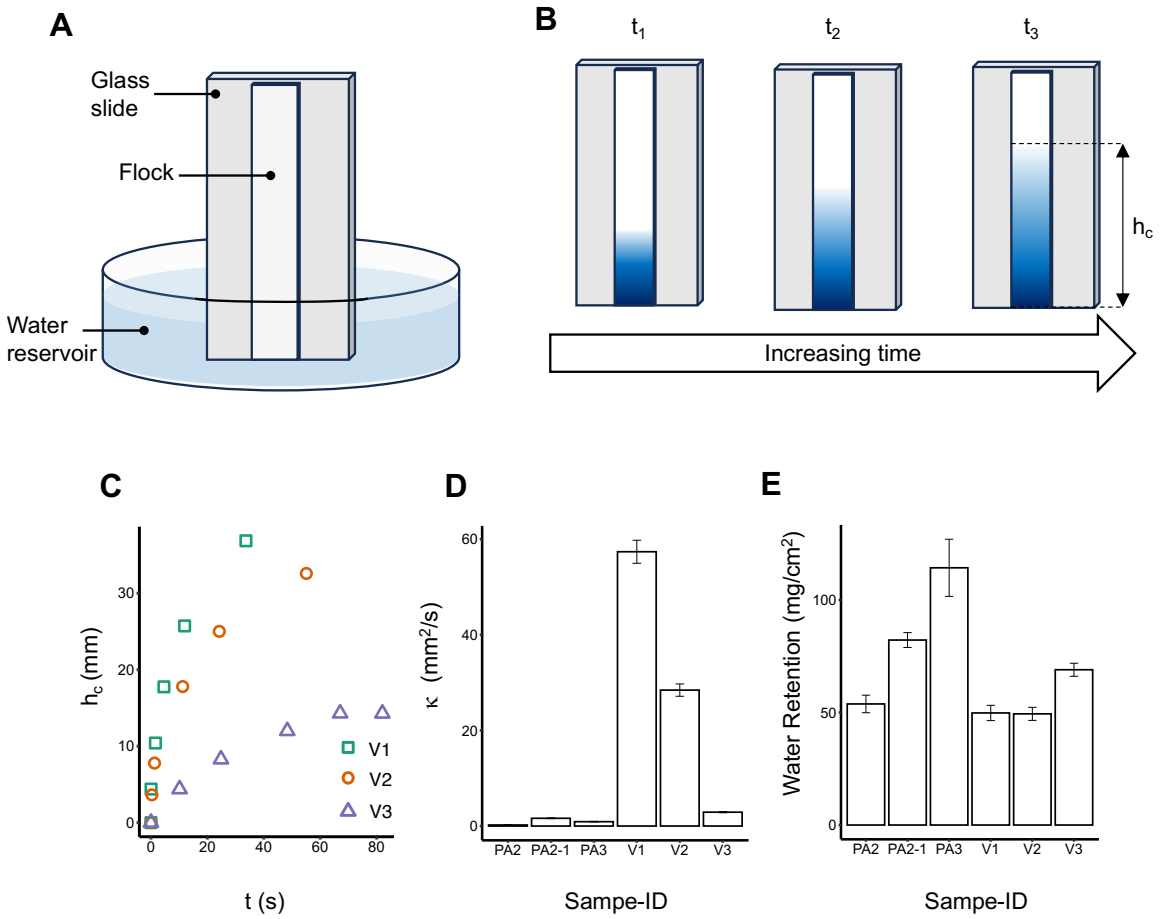

Figure 3.1.4: Wicking kinetics and water retaining properties of the different flocked substrates. (**A**) Schematic depiction of the experimental setup. (**B**) Wicking of the flocked substrate against gravity over time. (**C**) Wicking properties for the viscose flocks. (**D**) summarizes the WASHBURN constant for the flocked substrates. (**E**) shows a summary of the water-retaining properties.

Interaction of the Flocked Substrates with Fog

In the next study, the interaction of the flocked substrates with fog is explored. To obtain a more fundamental insight, the water condensation behavior directly on the flock fiber was investigated first. Here, environmental scanning electron microscopy (ESEM) was utilized. With this method, a defined water vapor pressure was introduced into the SEM chamber. By cooling the sample to the dew point, water condensation occurs directly on the flock fiber and can be observed in real-time. To minimize beam damage and to ensure sufficient contrast with a low signal-to-noise ratio, a water vapor pressure of 720 Pa at acceleration voltages between 5-10 kV was chosen. Under these conditions, the dew point occurs at 2 °C. Additionally, the specimens were all cooled from 5 °C to ~1.8 °C with a cooling rate of 1 °C/min to ensure adequate thermal transfer from the stage to the flock fibers. Starting the experiment at temperatures significantly above the dew point combined with the slow cooling rate gives the specimens sufficient time to equilibrate thermally. This protocol was deemed to be necessary because it was not possible to keep the stage at the dew point for a longer period of time. Upon reaching the dew point, water condensation simultaneously occurs on the sample stage, specimen holder, and the PELTIER element. Since water condensation should only be investigated on the flock fiber, condensation on the sample stage interferes with the evaluation and interpretation of the ESEM experiment. Furthermore, keeping the temperature at the dew point for longer periods results in water condensation in the space between the specimen holder and the PELTIER element, leading to a significant sample shift.

The ESEM experiments with the discussed parameters of the PA and viscose flock fibers are shown in Figure 3.1.5. Upon cooling the PA flock fiber (Figure 3.1.5 A to Figure 3.1.5 C), water droplet formation was observed. The formation of droplets is generally associated with a more hydrophobic surface chemistry. [112] The ESEM experiment of the viscose flock indicated the spreading of the condensed water toward a continuous film. However, due to the high electron dose, the aqueous environment, and the general instability of viscose in the electron beam, the flock fiber rapidly degraded and thus prevented successful interpretation of the condensation behavior.

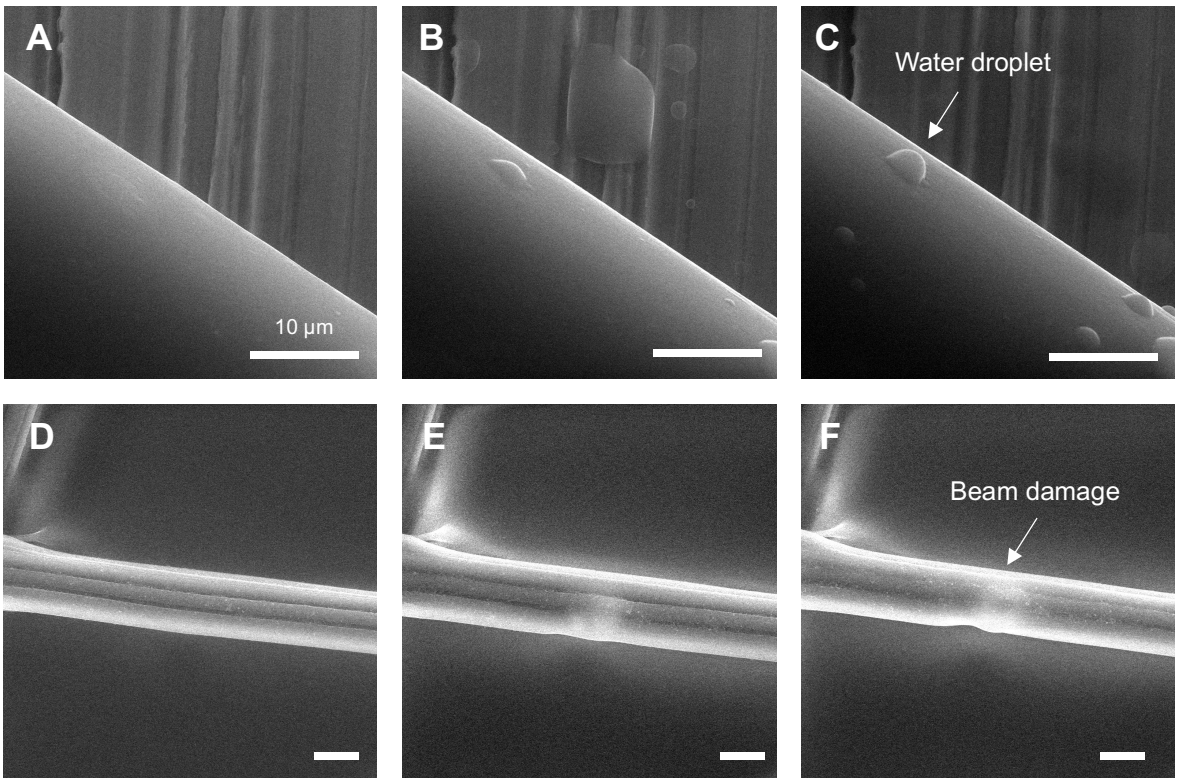

Figure 3.1.5: Scanning environmental electron microscopy micrographs of PA and viscose flock fibers. (**A**-**F**) show micrographs at a partial water vapor pressure of 720 Pa at different temperatures. (**A**-**C**) give the micrographs of PA3 while (**D**-**F**) of V2. (**B**, **E**) The stage is at the dew point, while (**C**, **D**) show the flock fibers below the dew point. The arrow in (**C**) indicates water droplet formation. The white arrow in (**F**) shows electron beam damage due to continuous irradiation in the aqueous environment. The scale bars in (**B**-**F**) correspond to 10 µm.

To investigate the condensation on the viscose flock fiber, nonetheless, a condensation stage for an optical microscope was designed. The condensation stage consisted of a water-cooled PELTIER element, which is controlled by a lab power supply. An Arduino microcontroller was used to monitor the temperature of the PELTIER, as well as the temperature and humidity of the encloser. Using the MAGNUS formula as proposed by M. Lawrence, [113] the dew point is estimated. To control the cooling rate, all the relevant data were transferred to a display in the front of the cooling stage. The voltage and amperage were then manually adjusted to reach the dew point. In general, a voltage between 3.0 V and 5.0 V at 3 A was sufficient to cool the sample to the dew point within ~5 min. A schematic cross-section view of the setup is shown in Figure 3.1.6 A. The setup was tested by cooling an Al-foil to the dew point. As shown in Figure 3.1.6 B-E, water condensation occurs as small droplets upon cooling the stage to the dew point. The longer the temperature was held, the more water condensed.

When the voltage was turned off, the stage warmed up over the course of a few seconds, and the droplets evaporated again.

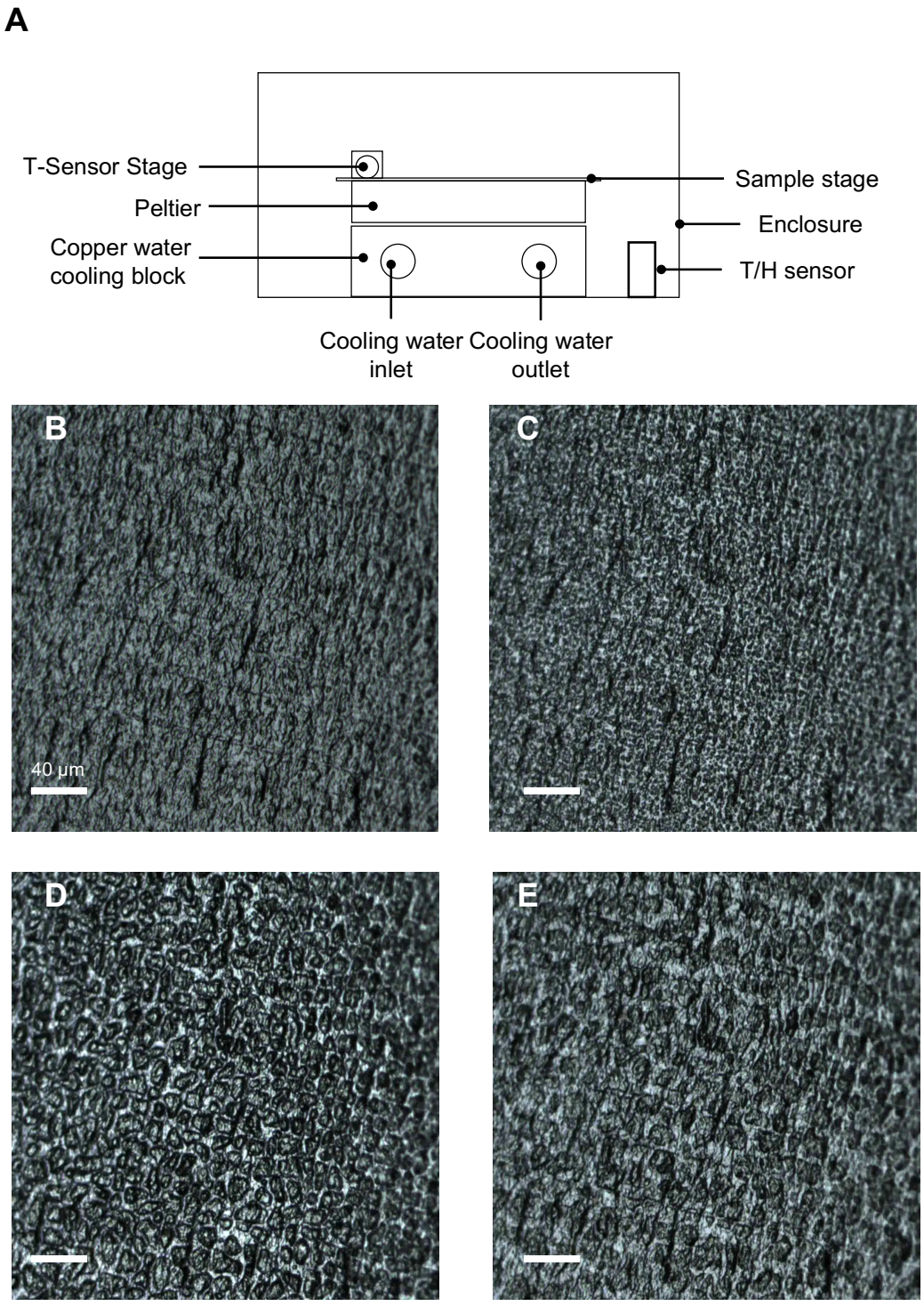

Figure 3.1.6: Condensation setup for optical microscope. (**A**) shows a schematic illustration of the condensation setup in the cross-section view. (**B**-**D**) gives the condensation behavior of an Al-foil during a test run, where (**B**) shows the initial dry stage, (**C**-**D**) during proceeded condensation, and (**E**) after warming the Al-foil above the dew point. The scale bars in (**C**-**E**) correspond to 40 µm.

After successfully testing the setup, isolated flock fibers were investigated by the condensation stage. The fibers were transferred to an Al-foil and slowly cooled to the dew point. The resulting micrographs during condensation are shown in Figure 3.1.7. The PA flock fibers showed similar behavior to that observed in the ESEM. Here, also water droplets were formed during the condensation. The viscose flock fibers, on the other hand, showed the formation of a water film that spread along the fiber axis. The spreading of the water confirms the more hydrophilic surface chemistry compared to the PA flock fibers, while the directional spreading is associated with the grooved surface. [36,38,112] As discussed in Chapter 1, when a surface is patterned with aligned grooves, water droplets tend to spread along these grooves.

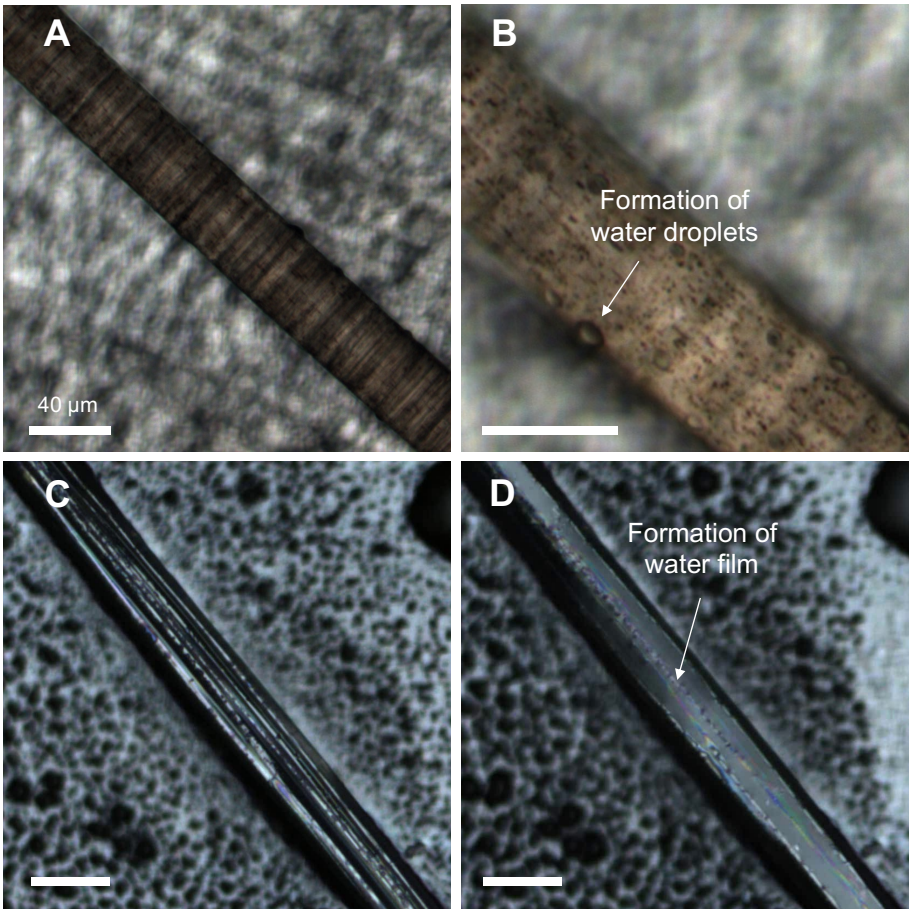

Figure 3.1.7: Condensation behavior of PA and viscose flock fibers by optical microscopy. (**A**-**C**) PA and (**D**-**F**) viscose flock fibers at the initial dry- and wetted state respectively. The scale bars in (**B**-**F**) correspond to 40 µm.

While in the previous experiments, the condensation directly on the fiber was investigated, in the following experiments, the interaction with suspended water droplets in air – namely fog – is analyzed. Here, two different behaviors between PA and viscose were observed. The PA flocked substrate captured the fog by the tip of the flock fiber, where water droplets aggregated into larger droplets (cf. Figure 3.1.8). Similar behavior was also observed for the viscose flocked substrate. The fog droplets were also intercepted by the flock fiber tip. However, due to the hydrophilic surface, the fog droplet immediately spreads after the interception, where the condensed fog droplets are then taken up by the flocked structure.

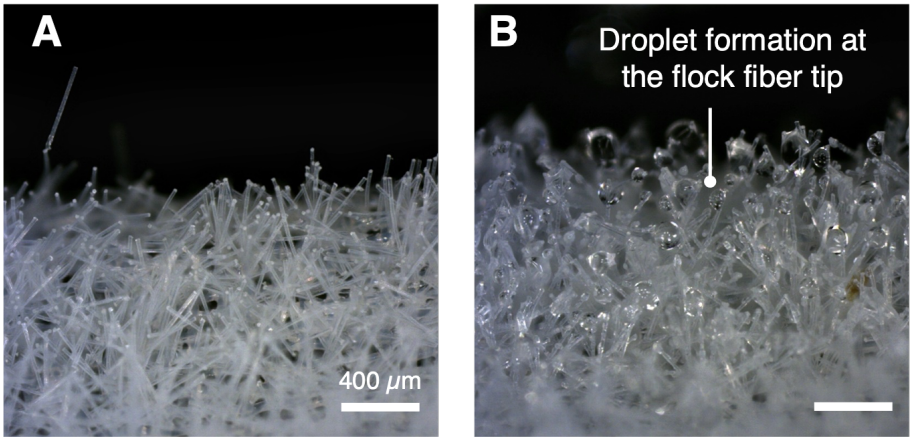

Figure 3.1.8: Optical microscopy micrographs of the PA2 flock during fog irrigation. (**A**) shows the side view of the PA2 flock in the dry- and in (**B**) during fog irrigation state. The scale bar in (**B**) corresponds to 400 µm.

Besides the wettability, the flock fiber dimensions also influence the fog capture. PA2 flocked substrates mostly capture fog by the flock fiber tip. However, when irrigating the PA3 flocked substrates with fog, a larger portion of the flock fiber surface was wetted. (cf. Figure 3.1.9). This is attributed to the larger pore size of the PA3 flocked substrates compared to the PA2 flocked substrate. The larger the flock fiber, the larger the pore size, and therefore, more area of the flock fiber tip is accessible to the fog stream. Thus, it is suggested that flocked substrates with larger pore sizes should experience a higher fog intercepting yield compared to flocked substrates with smaller pore sizes.

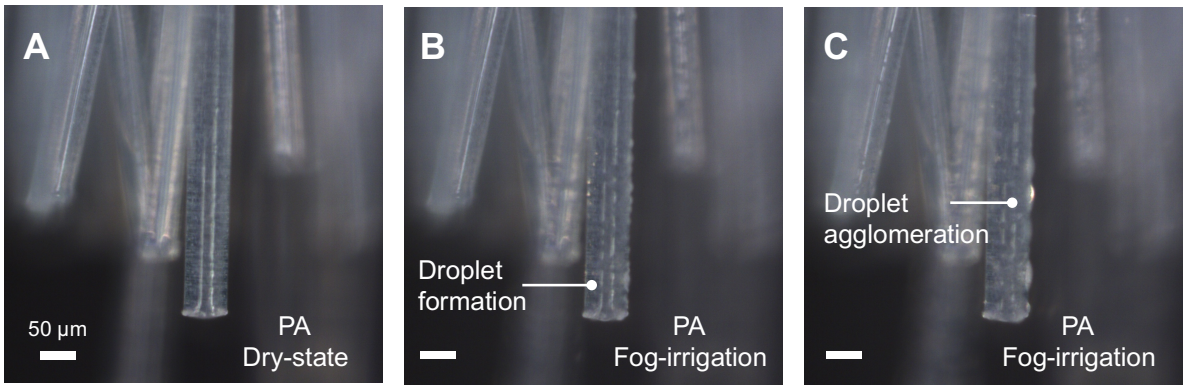

Figure 3.1.9: Fog irrigation of PA3 flocked substrate. (**A**) gives the dry state while (**B**, **C**) shows the flocked substrate after continuous fog irrigation. The scale bars in (**B**-**C**) correspond to 50 µm.

To conclude, in the preliminary study, the flocking behavior of PA and viscose flock fibers and their interaction with water and fog were investigated. It was shown that the orientation of the fibers remained unaffected by their dimensions. However, larger flock fiber dimensions resulted in a higher flock density due to the increased mass of a single fiber and an increased thickness of the adhesive layer to ensure sufficient flock fiber anchoring. Furthermore, with larger flock fiber dimensions, the porosity of the flocked substrate decreased while the pore size increased. By utilizing wicking and *in-situ* water condensation experiments, it was shown that water on the surface of PA flock fibers tended to droplet formation. On the other hand, viscose flock fibers spread water droplets to a water film along the fibers' axis due to the hydrophilic and microgrooved surface. This behavior is translated to the fog interaction with the respective flocked substrate. PA showed a droplet-growing fog capture mechanism and viscose flock fibers a spreading of the intercepted fog particles. Additionally, flocked substrates with larger pore sizes intercepted more of the fog stream due to the increased pore size.

3.2. Namib Desert Beetle Inspired Membrane

As mentioned in Chapter 1, the Namib desert beetle shows a simple and easily adaptable morphology consisting of a hydrophobic background decorated with hydrophilic spots. This morphology was already realized in the scientific literature by a large variety of different strategies. [9,40,44,45,81,114] Many of these strategies may be readily implemented in a flock-based approach, but in the scope of this thesis, a novel fabrication method was pursued.

The fabrication method combined a hydrophobic electrospun nonwoven with hydrophilic viscose flock fibers (cf. Figure 3.2.1). The Namib desert beetle-inspired membrane was obtained in three steps. In the first step, the hydrophobic nonwoven was fabricated by electrospinning. For this, Poly(vinylidene fluoride-*co*-hexafluoropropylene) (P(VDF-*co*-HFP)) polymer was dissolved in *N*,*N*-dimethylformamide (DMF) and acetone. Then the polymer solution was transferred to a syringe and a high voltage between the cannula and substrate was applied, resulting in the formation of a nanofibrous nonwoven. [115,116] After fabrication and cleaning of the nanofibrous nonwoven, the adhesive was selectively applied by a stamp to achieve the required pattern. For this, the stamp was pressed in a thin adhesive film (Figure 3.2.1 A), followed by applying the stamp to the previously electrospun nonwoven (Figure 3.2.1 B). In the last step, flock fibers are applied to the nonwoven by electrostatic flocking (Figure 3.2.1 C). After washing and drying the flocked sample, flock fibers only remain in the previously adhesive-covered spots, resulting in the Namib desert beetle inspired morphology (Figure 3.2.1 D).

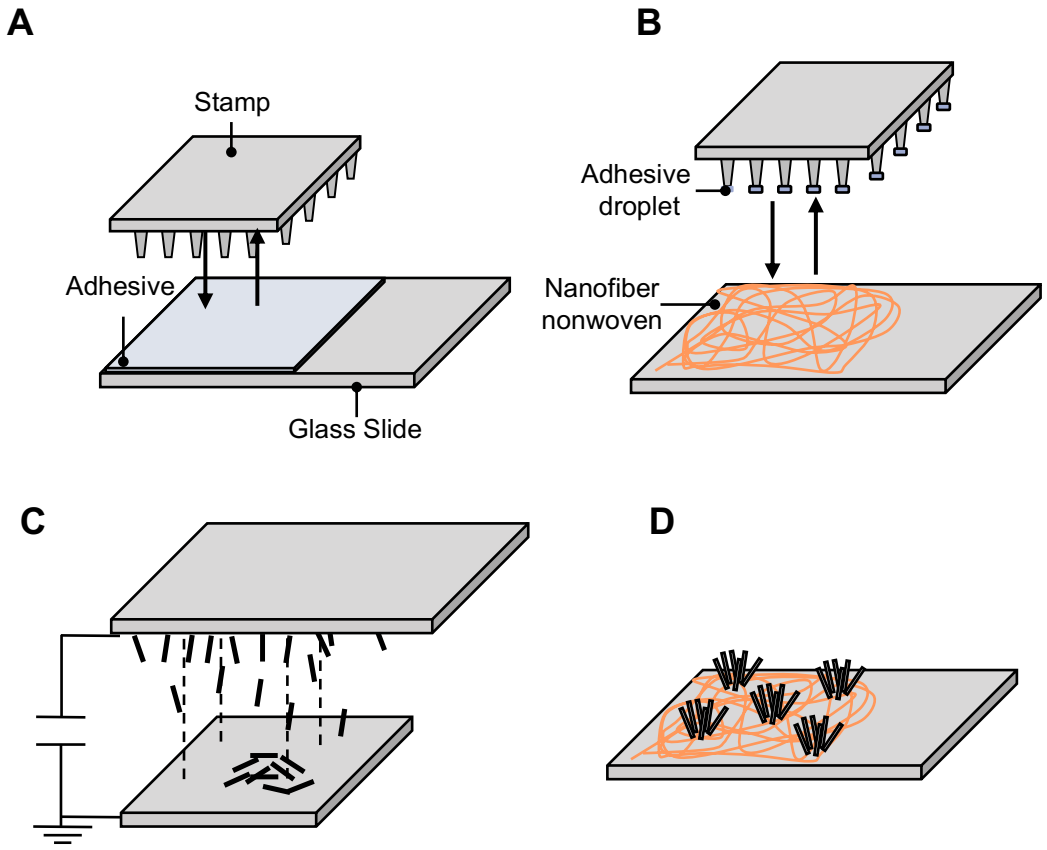

Figure 3.2.1: Schematic illustration of the fabrication process. The Namib Desert Beetle-inspired membrane was obtained in overall three steps. First, a hydrophobic nonwoven was electrospun, and a stamp was fabricated. (**A**) The stamp was immersed in a thin adhesive film. (**B**) The pattern was then transferred to the previously fabricated nonwoven and (**C**) the flock fibers were applied by electrostatic flocking. (**D**) After washing with water, non-anchored flock fibers were washed away, resulting in a structured membrane.

Fabrication of an Electrospun Hydrophobic Nonwoven

In general, many different fiber materials are worth considering. However, P(VDF-*co*-HFP) was chosen due to the easy spinnability and high hydrophobicity of the fiber material. As shown by Correia *et al.*, the water contact angle of the P(VDF-*co*-HFP) is around 100 deg and thus is defined as a hydrophobic material. [43,117] Due to the microstructure of an electrospun nonwoven, an even more pronounced hydrophobicity of ~115 deg. angle is reported. [43] For the fabrication of the P(VDF-*co*-HFP) nonwoven, a voltage of 15 kV was applied between the cannula and a grounded Al-foil. The resulting nanofibers evenly covered the Al-foil. After ~1 h of continuous spinning, the nonwoven was dried, washed with water to remove residual DMF, and dried again. An overview of the membrane characteristics is given in Figure 3.2.2. SEM micrographs of the electrospun nonwoven membrane are shown in Figure 3.2.2 A and Figure 3.2.2 B.

The nanofibers had a smooth surface and an average diameter of 0.45(1) µm (cf. Figure 3.2.2 C). Similar to the results of Correia *et al.*, [43] the nonwoven membrane showed a water contact angle of 115(4) deg (cf. Figure 3.2.2 D) and is therefore classified as a hydrophobic material.

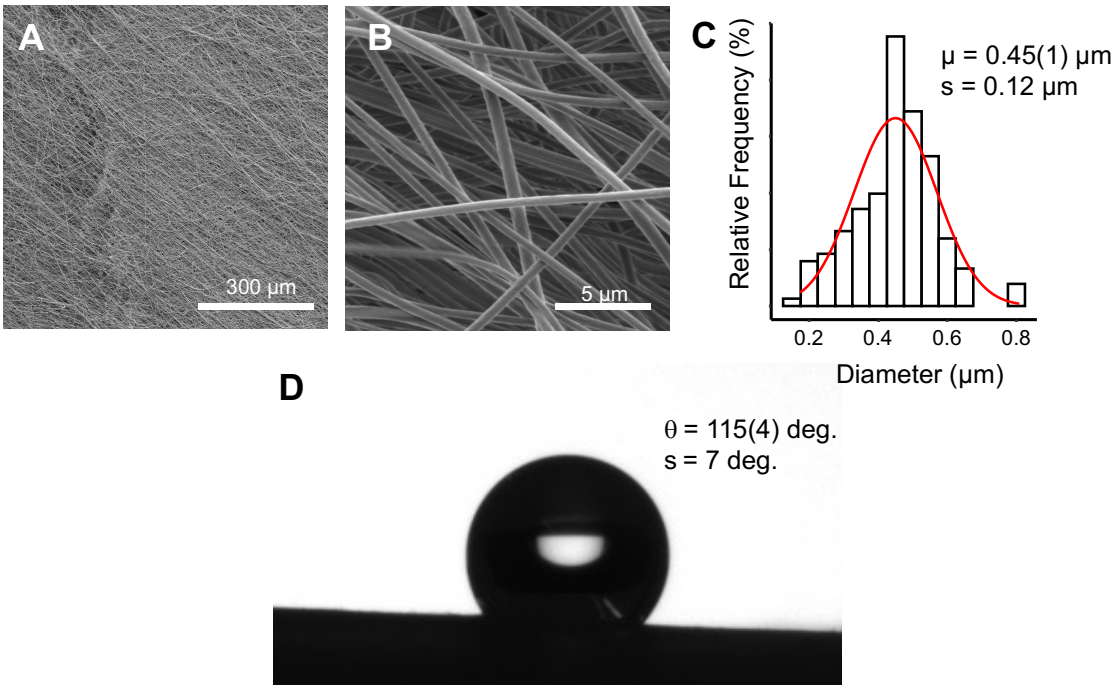

Figure 3.2.2: Overview of the electrospun P(VDF-*co*-HFP) nonwoven. (**A**, **B**) shows the overview and high-resolution SEM micrographs of the electrospun nonwoven, respectively. (**C**) gives the histogram of the fiber diameter evaluation. The average is abbreviated with μ with the errors noted in round brackets. The standard deviation is abbreviated with s. The red curve indicates the normal distribution. (**D**) shows the contact angle micrograph of a water droplet on the (PVDF-*co*-HFP) nonwoven, where θ represents the contact angle and s the corresponding standard deviation.

Stamp Fabrication

In the next step, the adhesive is selectively applied to the membrane to obtain an adhesive pattering. A stamping approach was chosen due to the ease of application, reproducibility, and high sample throughput. The stamp consisted of 31 heads with a 2 mm circular cross-section in a hexagonal pattern. The distance between the heads was kept to 2 mm. To allow more rapid prototyping, the stamp was fabricated by fused deposition modeling (FDM) 3D-printing.

An overview of the 3D model and the optical microscope micrographs of the fabricated stamp is shown in Figure 3.2.3. Due to layer-by-layer fabrication of the FDM printing process, the stamp showed a longitudinal structured surface morphology (cf. Figure 3.2.3 C, D).

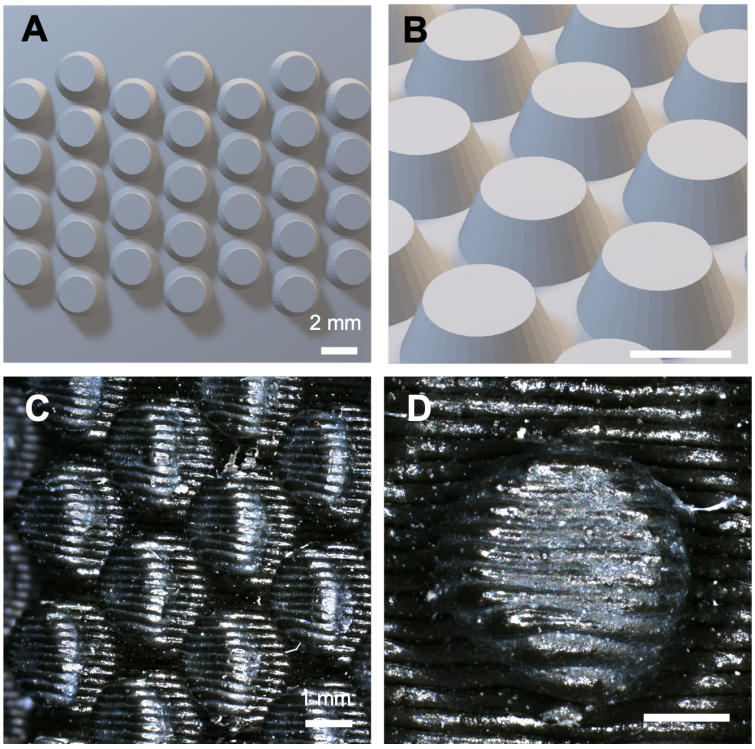

Figure 3.2.3: Overview of the adhesive application stamp. (**A**, **B**) shows the 3D model and (**C**, **D**) optical microscopy micrographs of the 3D printed stamp. The scale bars in (**B**, **D**) correspond to 2 mm and 1 mm, respectively.

In the next step, the adhesive application to the nonwoven was investigated. For this, the adhesive was applied to the stamp and then pressed for ~ 3 s to the nonwoven. Afterward, the nonwoven was peeled off the stamp and dried at room temperature (r.t.) for 2 d. As shown in Figure 3.2.4 A, the adhesive is applied evenly in the hexagon pattern specified by the 3D-printed stamp. While on the macroscopic scale, the adhesive has defined edges, according to the related SEM micrographs (cf. Figure 3.2.4 B and Figure 3.2.4 C), the edges of the adhesive layer seemed to be less defined and showed a fringed edge morphology. However, the fringes had significantly smaller dimensions than the flock fibers and, therefore, were not expected to negatively influence the anchoring of the flock fiber to the electrospun nonwoven. In the cryogenically cut cross-section of the membrane (cf. Figure 3.2.4 D), the adhesive formed a continuous film and showed complete embedding of the nonwoven in the adhesive film, suggesting a sufficient adhesion to the P(VDF-*co*-HFP) membrane.

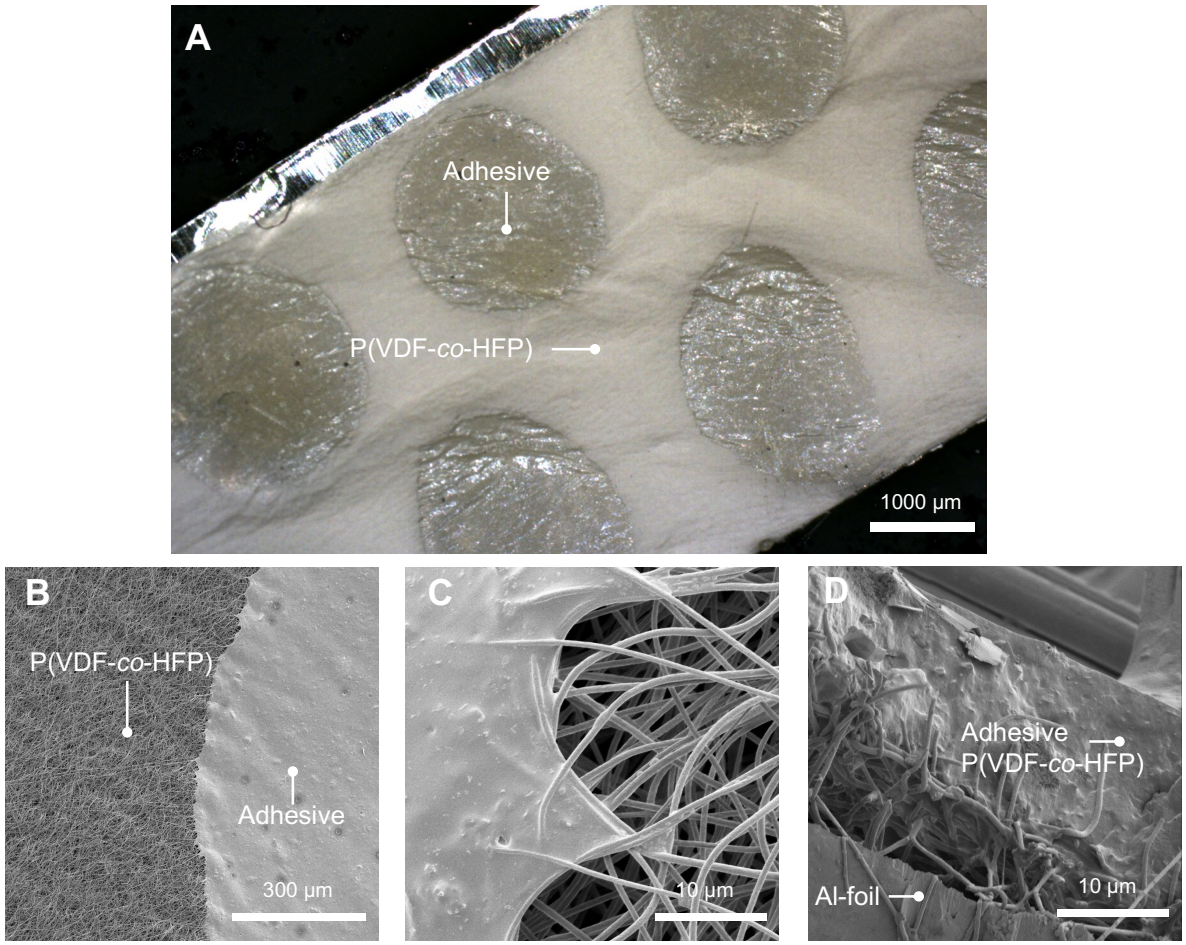

Figure 3.2.4: Adhesive application to an electrospun nonwoven by the 3D printed stamp. (**A**) gives an optical microscopy micrograph of the sample. In (**B**-**D**), the membrane was investigated by SEM, while (**D**) shows a cryogenically cut cross-section view.

Fabrication of the Namib Desert Beetle-Inspired Membrane

In the final fabrication step, the nonwoven was modified with hydrophilic V2 flock fibers. Hereby, the nonwoven was electrospun and selectively modified with adhesive spots, as described in the previous chapters. Immediately after the nonwoven was peeled off the stamp, the ground was attached to the nonwoven with a crocodile clamp, and an electric field was applied for ~ 30 s. Afterward, the adhesive was cured for 2 d at r.t. and then cleaned with pressured air and water. After application of the flock fibers, the V2 fibers were applied evenly to the whole membrane. However, after the cleaning steps, the flock fibers only remained in the spots previously covered with the adhesive by the stamping technique (cf. Figure 3.2.5 A, Figure 3.2.5 B). According to the SEM micrographs, the flock fibers were uniformly applied to the adhesive spots. In contrast, the area between the flock spots showed neglectable contamination of loose flock fibers (cf. Figure 3.2.5 C, Figure 3.2.5 D).

The proposed fabrication scheme may also be possible to implement with different flock fibers. However, flock fibers with lengths > 0.5 mm were insufficiently anchored in the adhesive layer and suffered from significant fiber leaching during the water washing steps.

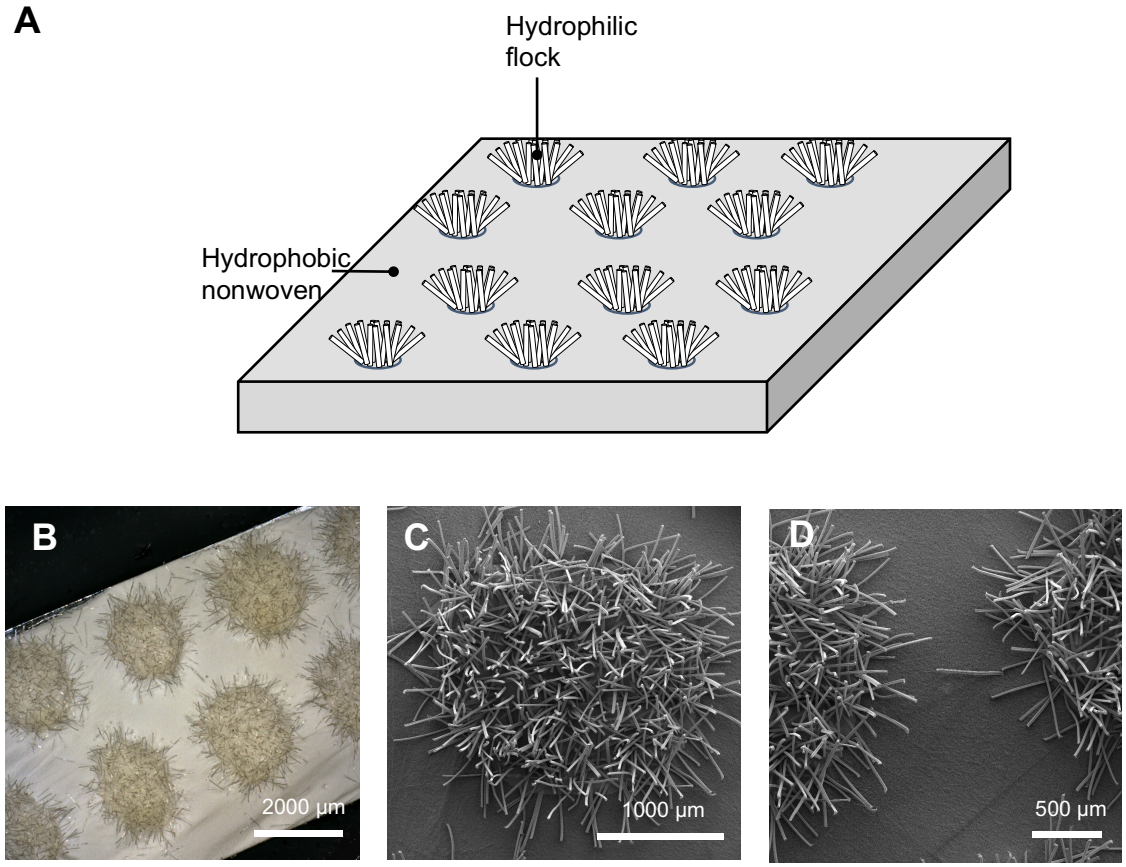

Figure 3.2.5: Beetle-inspired flock membrane. (**A**) Schematic illustration of the fabricated beetle-inspired flock membrane consisting of hydrophobic nonwoven and hydrophilic flock fibers. (**B**) Optical microscopy micrograph of the membrane. (**C**, **D**) SEM micrographs of the hydrophilic flock fiber spots.

Fog Interaction of the Namib Desert Beetle-Inspired Membrane

At last, the interaction of the prepared Namib desert beetle-inspired membrane with fog is investigated. Here, the membrane was fixed at ~60 deg. angle relative to the ground to ensure roll-off and still maintain a sufficient focus plane. The samples were then irrigated continuously with fog. A schematic illustration of the observed fog-condensing mechanism is shown in Figure 3.2.6 A. In general, fog droplets condensed on the electrospun nonwoven, where small droplets with a high contact angle were formed. These droplets grew in size until they interacted with the hydrophilic flocked spots. When contacting the hydrophilic spots, the droplets were immediately taken up by the flocked structure.

This process was repeated until the maximal water-retaining capacity of the flocked structure was reached. Then, the droplets either coalesced with neighboring water droplets into larger water droplets or rolled off the membrane (cf. Figure 3.2.6 B-E), resulting in a fog-collecting mechanism similar to the Namib desert beetle.

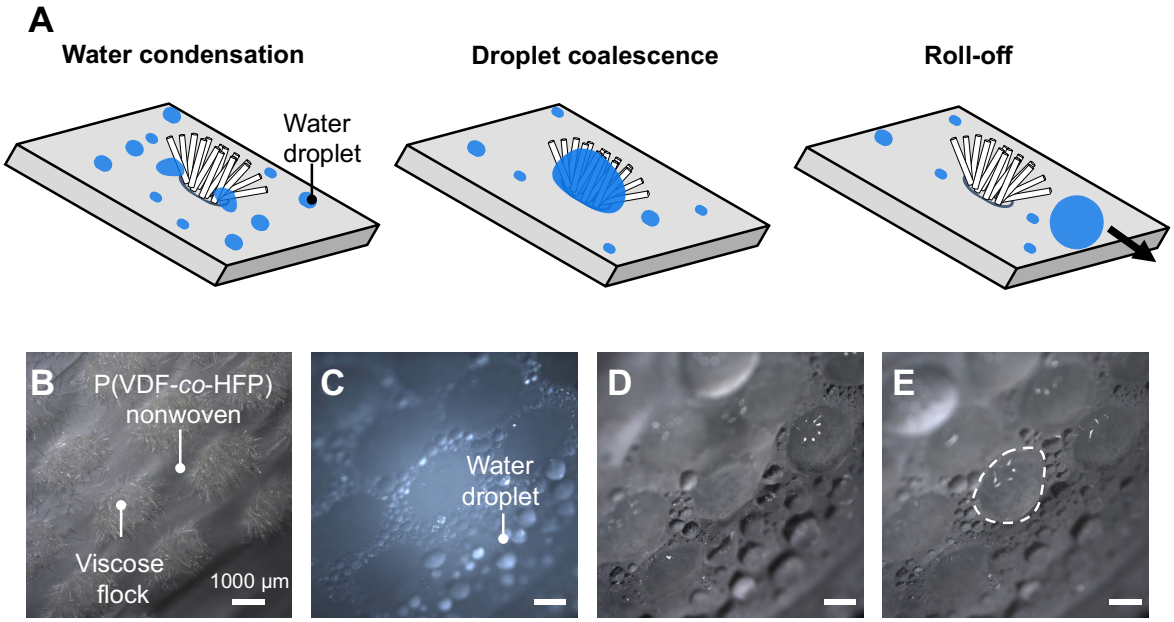

Figure 3.2.6: Fog harvesting mechanism of the Namib Desert Beetle-inspired flock membrane. (**A**) shows a schematic representation of the fog-collecting mechanism. (**B**) shows the membrane in the dry state while (**C-E**) gives snippets during fog irrigation. The white dashed line in (**E**) indicates a water droplet.

In conclusion, a Namib desert beetle-inspired flock-based membrane was fabricated, and the interaction with fog was investigated. While the bioinspired fog collecting mechanism was successfully implemented in the structure, the morphology may be optimized in several ways. Due to the spatial resolution limit of the FDM 3D printing process, adhesive spots with rather large cross-sectional diameters were applied. To obtain more control over the spatial resolution of the adhesive application process, different stamp fabrication methods may be used (e.g., stereolithography (SLA), micromachining), or a different application method may be developed. In general, lithography is a well-established method to fabricate structurally defined structures. [118] Here, UV-curable adhesives may be easily transferred to the proposed process.

3.3. Supramolecular Cacti Spines

Besides the Namib desert beetle, cacti spines are well known in the scientific literature for efficiently nucleating and transporting water droplets. [11,25] Namib desert beetles evolved a strategy that involves the coalescence of fog particles into larger water droplets. The water droplets are then transported by tilting the backplate, relying on the gravitational pull to move the water droplet once a sufficient droplet size is reached. On the other hand, due to their unique anisotropic features, cacti spines are able to transport water droplets unidirectionally, even against gravity.[31,47,48] However, their highly anisotropic morphology makes implementing cactus spine structures in material science challenging. Mimicking all three relevant features for the unidirectional water transport at once - cone geometry, gradient wettability, and longitudinal microgrooves - is especially difficult. For example, it was shown that electrochemical etching was able to produce spine structures. However, this method only replicates the cone geometry.[34] On the other hand, electrospinning combined with a sacrificial template produced a cone geometry with microgrooves. [3] Yet, these microgrooves were not oriented along the spine axis but instead resulted in a helical formation. As shown by D. Chen *et al.*, a JANUS wettability difference along the spine with a hydrophobic tip and a hydrophilic base was obtained by selective coating of an artificial spine. [119] However, this fabrication strategy does not give rise to gradient wettability, which is essential for effective droplet transport.

Besides the mentioned approaches, 3D printing, [35] magnetorheological lithography, [49] or vapor-phase approaches [120] were utilized to obtain cacti-inspired features. Therefore, with the discussed limitation of the published fabrication strategies in mind, there is a need for an artificial spine fabrication strategy that includes all three characteristic features of a cactus spine. Furthermore, the fabrication should be easy to apply and scalable. A promising method for such structures, which fulfills all the requirements, would be molecular self-assembly in a bottom-up approach. Here, BTAs may be the material of choice since it is well described in the scientific literature and is known to self-assemble into fibrous structures, which could be an appropriate starting material morphology to fabricate anisotropic spine geometries with longitudinal microgrooves.

The Molecule Class of 1,3,5-Benzenetricarboxamides

BTAs are a molecule class that forms supramolecular fibers by molecular self-assembly. In general, the molecular structure of BTAs consists of a core, a hydrogen-bonding-donor-acceptor functionality, and a peripheric unit (cf. Figure 3.1.1 A). The core is composed of a planar, aromatic unit.[121] The hydrogen-bonding-donor-acceptor pair consists of carboxamides, where the N-H group provides the donor- and the C=O group the acceptor functionality. The peripheric unit, however, can be built from a wide variety of different functional groups ranging from aliphatic to highly functional units. [122–124] Here, besides the connectivity and core, the specific peripheric unit significantly controls the self-assembly behavior. [121] As shown in Figure 3.3.1 B, the self-assembly proceeds by hydrogen-bonding stacking. The molecular building blocks are fixed by a three-stranded hydrogen bonding to helical columns. These columns then further assemble into larger aggregates, forming supramolecular fibers. [121]

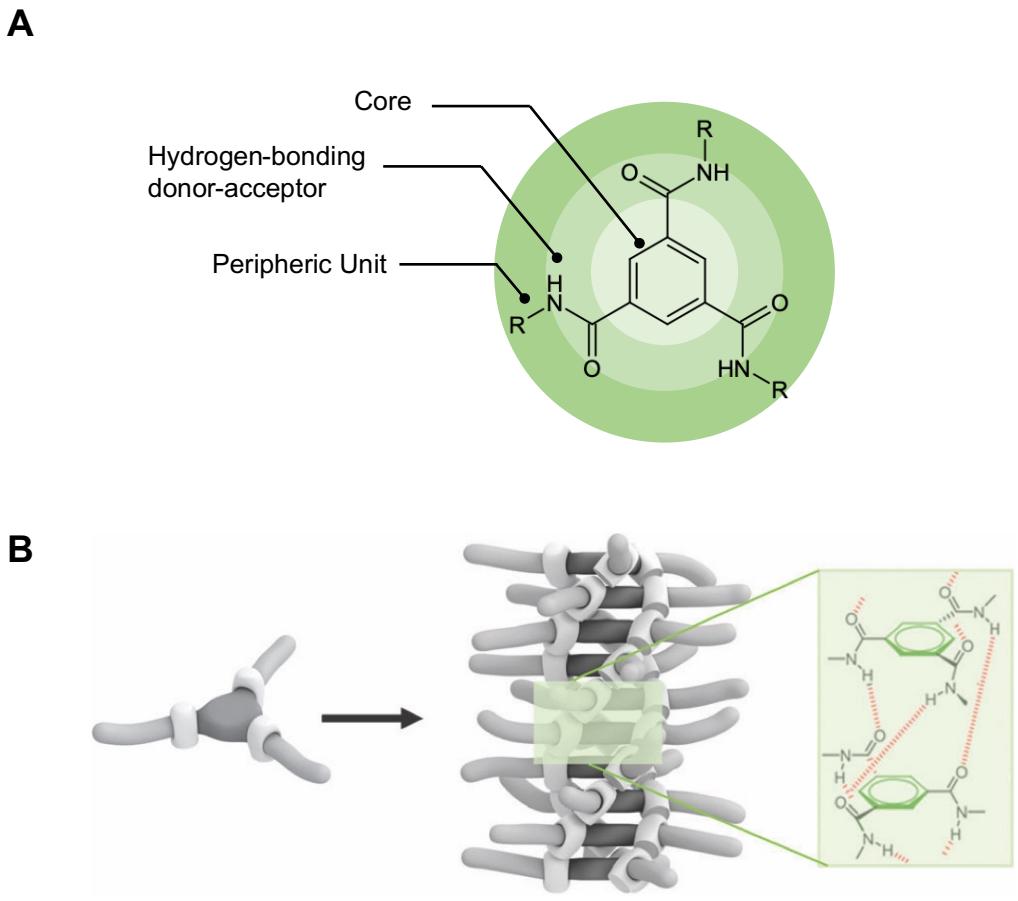

Figure 3.3.1: Schematic representation of BTA self-assembly. (**A**) shows the molecular BTA building block, consisting of an aromatic core, a hydrogen-bonding donor-acceptor unit, and a peripheric unit. (**B**) shows the self-assembly of the BTA building block into columnar structures due to hydrogen bonding. (**B**) Reprinted with permission from: [121].

As shown in Figure 3.3.2, a typical BTA phase diagram consists of three phases: A dissolved phase (BTA solution I), an assembled phase (BTA assembly II), and an insoluble phase (BTA insoluble III). For the case of supramolecular fiber formation by solvent evaporation, the BTA is first dissolved generally at elevated temperatures. After cooling, the BTA solution forms a stable solution. Due to solvent evaporation, the BTA concentration increases and the formation of supramolecular BTA assemblies occur. This process continues until complete solvent removal, and solvent-free supramolecular BTA fibers are formed. Additionally to solvent evaporation route, the BTA assembly phase (II) can also be reached by cooling or a combination of cooling and solvent evaporation. [121,122]

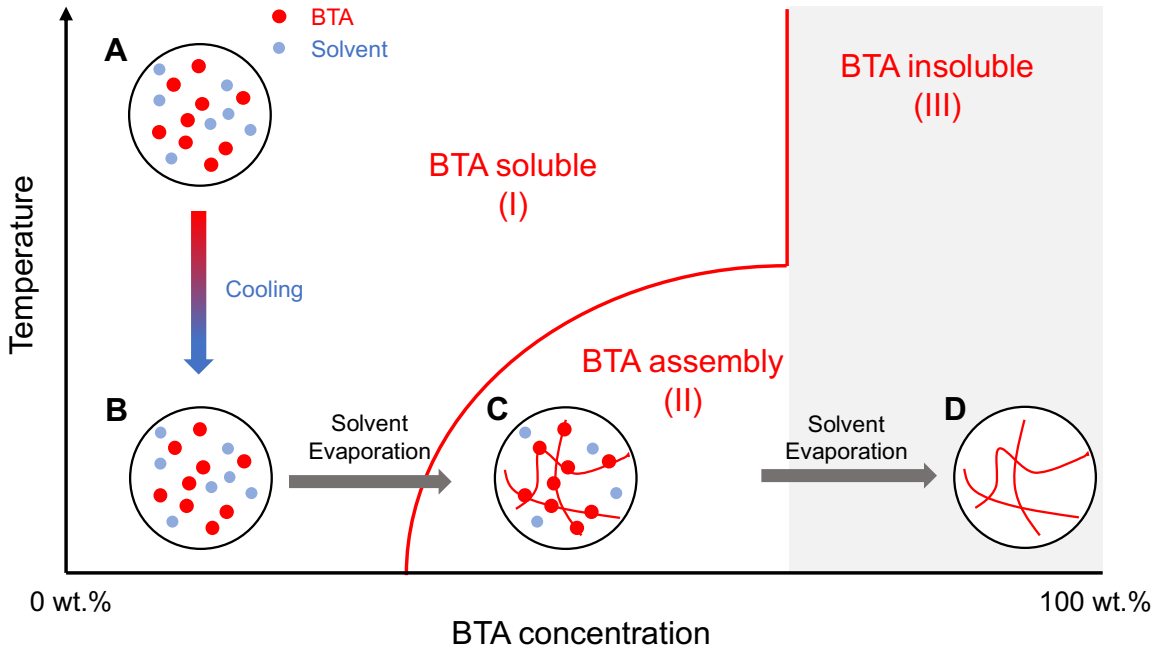

Figure 3.3.2: Schematic representation of a typical BTA phase diagram. The simplified phase diagram consists of a dissolved (BTA soluble I), an assembled (BTA assembly II), and an insoluble (BTA insoluble III) phase. For the case of solvent evaporation, (**A**) the BTA is completely dissolved at elevated temperature. (**B**) The solution is then cooled while still forming a stable solution. (**C**) Due to solvent evaporation, the concentration of the BTA solution increases, leading to BTA aggregates. (**D**) Further solvent evaporation leads to the complete self-assembled of supramolecular BTA fibers. Besides solvent evaporation, the BTA assembly phase (II) can be reached by cooling or a combination of cooling and evaporation. The specific path in the phase diagram depends on the BTA building block as well as the solvent choice. Adapted from: [122].

Besides the chemical structure of the peripheric unit or solvent, it has been shown that the specific BTA fiber morphology drastically depends on the substrate. In the work by Burgard *et al.* and Frank *et al.*, a chemical nucleus – BTA molecule or polymer patchy micelles – were utilized as seeding points. [8,125] It was observed that mesostructured morphologies were obtained by evaporation-guided molecular self-assembly in such a seeded-electrospun nonwoven, obtaining different mesostructured morphologies. As described in Chapter 3.1, flocked structures show interesting capillary-driven solvent transport behavior. Due to the unusual transport effects in flocked substrate, increased evaporation rates would lead to a concentration gradient. This concentration gradient may result in seeding nuclei which may further promote anisotropic fiber structure.

BTA Self-Assembly in a Flocked Substrate

In this thesis, the already published BTA molecule building block N^1, N^3, N^5-tri[2-(diisopropyl amino)-ethyl]-1,3,5-benzenetricarboxamide (*i*Pr-BTA) is focused on. [125] To establish a baseline, *i*Pr-BTA was dissolved in 2-propanol at a stable concentration of 0.50 wt.%. [125] Here, upon evaporation on a silicon wafer, the formation of uniform fibers with a fiber bundle morphology was observed (cf. Figure 3.3.3).

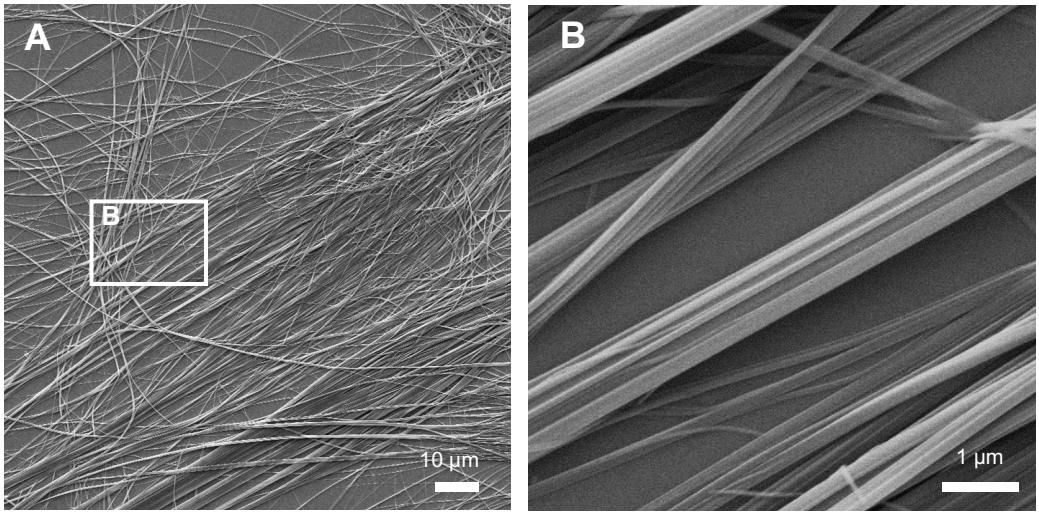

Figure 3.3.3: SEM micrographs of the assembled *i*Pr-BTA on a silicon wafer. (**A**, **B**) shows the fiber formation upon evaporation of *i*Pr-BTA on a silicon wafer from 2-propanol.

In the next step, the flocked substrate for the self-assembly experiments was prepared. During this study, the choice of flock fiber was initially restricted to PA2 flock fibers (cf. Figure 3.3.4). The flock fibers were applied to a PET mesh with a pore and thread size of 100 µm. The prepared PA2 flocked substrate exhibits an overall flock fiber orientation of 100.5(3) deg and a density of 5.4(1) mg/cm².

The decreased density is associated with the smaller amount of adhesive applied and the smaller accessible surface area available for the flock fibers. Due to the lower density, the flock fibers cannot self-stabilize and, therefore, show slightly decreased orientation. Since a porous substrate was used, the flocked scaffold also has a porous structure. However, due to the adhesive application, the pore size of the PET mesh was decreased from 100 µm to 62(3) µm. This decrease in pore size also aligns with the air permeability measurements. The PET mesh showed an air permeability of 1076(4) mm s^{-1}, and the flocked substrate had a permeability of 516(1) mm s^{-1}. Due to the reduced pore size as well as the increased air resistance exhibited by the flock fibers, an overall decreased air permeability was observed.

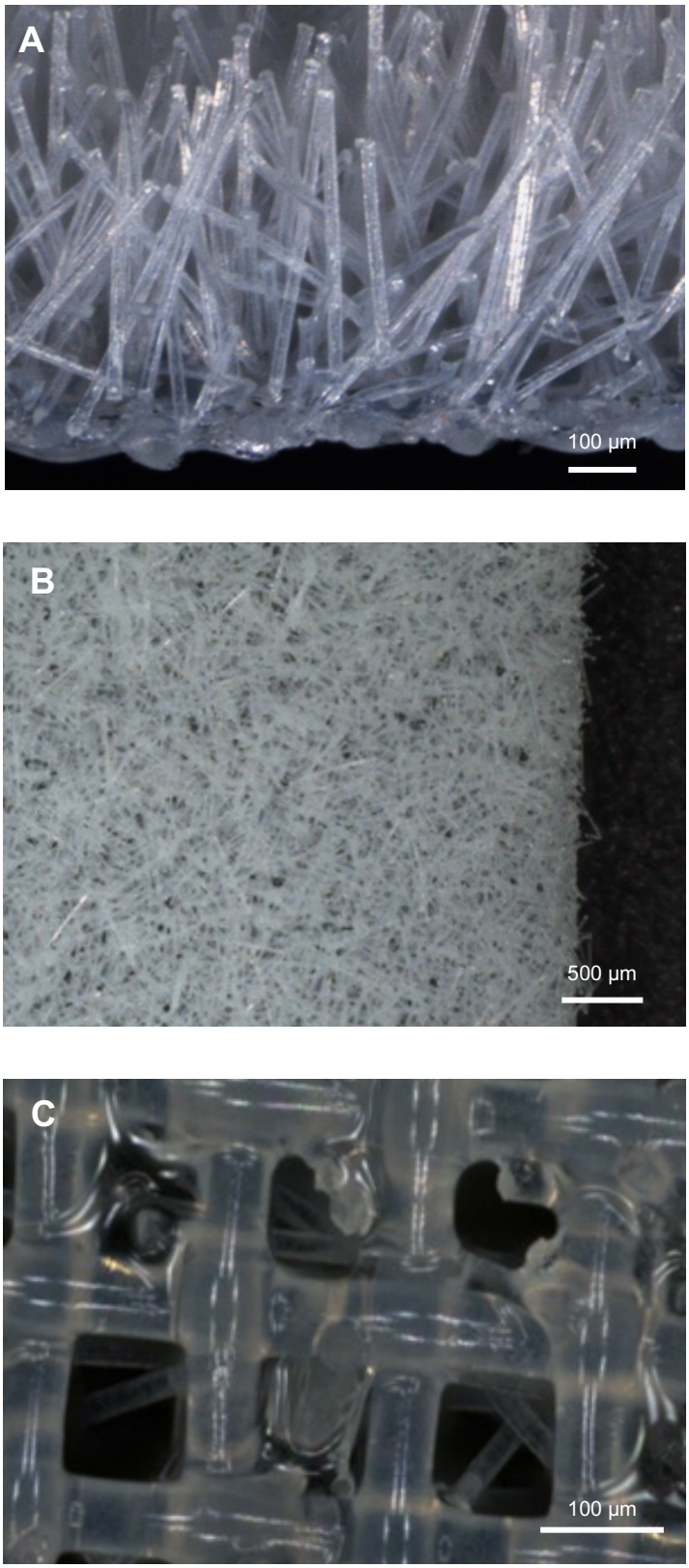

Figure 3.3.4: Optical microscope images of the PA2 flocked substrate on a PET mesh. (**A**) side view of the PA2 flock (**B**) top view, and (**C**) view of the PET mesh from the bottom. Reprinted with permission from [145].

After preparing the flocked substrate, self-assembly experiments of *i*Pr-BTA at 0.50 wt.% in 2-propanol were performed. The flocked substrate was immersed in the *i*Pr-BTA solution for a few seconds. Afterward, the flocked substrate was removed from the solution and placed on filter paper to partially remove the *i*Pr-BTA solution from the substrate. Then, the flocked substrate, filled with *i*Pr-BTA solution, was transferred to a petri dish and covered with Al-foil to evaporate the solvent at 30 °C. This protocol resulted in the selective formation of supramolecular spines on top of PA2 flock fibers. As schematically shown in Figure 3.3.5, the assembled spine has a similar morphology to a cacti spine.

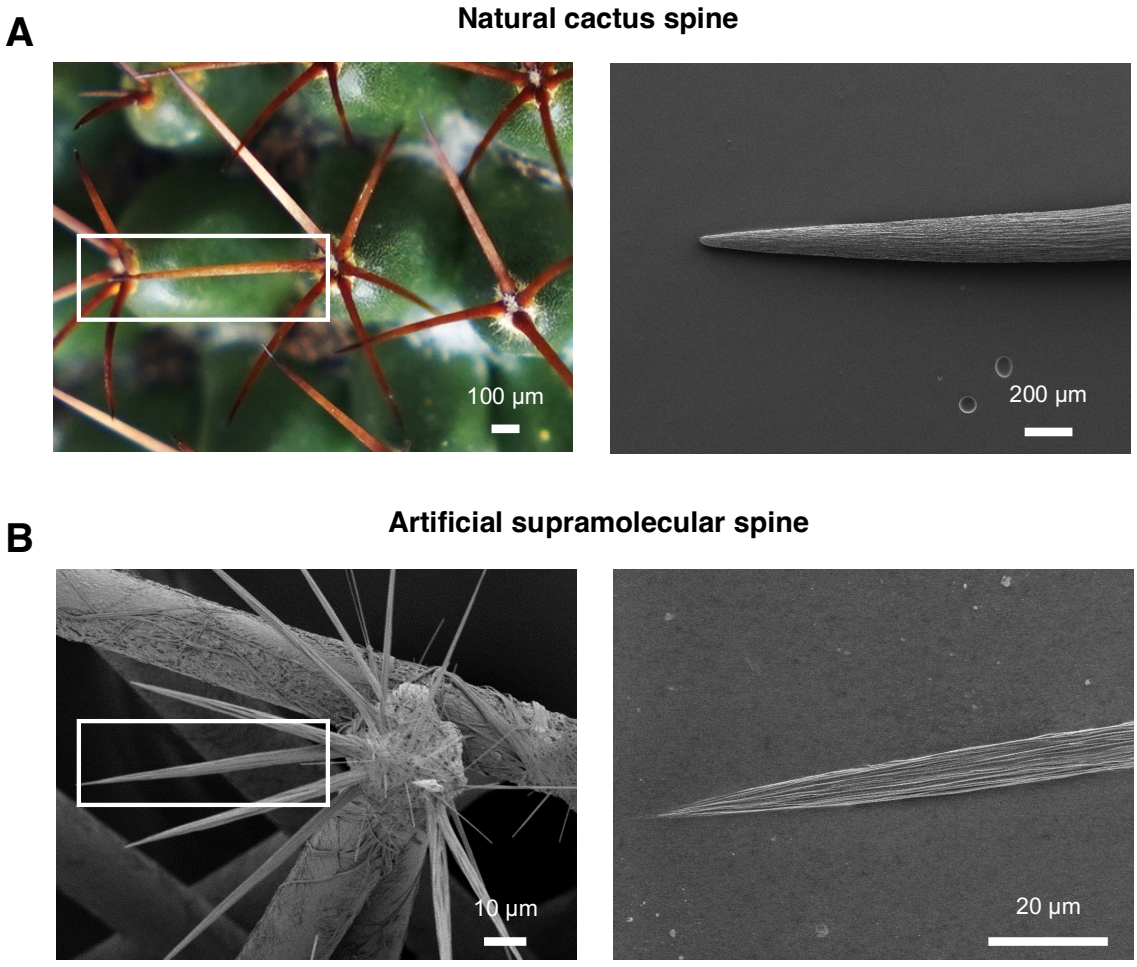

Figure 3.3.5: Comparison of a natural cactus spine *vs.* the self-assembled BTA spine. (**A**) shows the cactus *mammillaria neocoronaria* with (**B**) a SEM micrograph of a single spine. (**C**, **D**) gives SEM micrographs of the assembled BTA spines on top of a single PA flock fiber and a single isolated BTA spine, respectively. Reprinted with permission from [145].

Supramolecular Spine Morphology

In general, the morphology of the supramolecular spine comprises three main hierarchical levels. The first hierarchical level is the molecular self-assembly of the *i*Pr-BTA molecules driven by three strands of hydrogen bonds into single supramolecular columns. On the second hierarchical level, the supramolecular columns are densely packed into supramolecular fibrils. Finally, these fibrils further organize themselves with a high degree of order into the supramolecular spine with a conical geometry.

The specific morphological structure of the supramolecular *i*Pr-BTA spine was investigated in more detail by high-resolution SEM (cf. Figure 3.3.6). Overall, the morphology of a supramolecular spine is divided into the tip, middle part, and base, as depicted in Figure 3.3.6. The spine tip featured a smooth and defined shape with less than 400 nm in diameter (Figure 3.3.6 B). The middle part of the spine included fibril diameters between 500 nm – 1 µm.

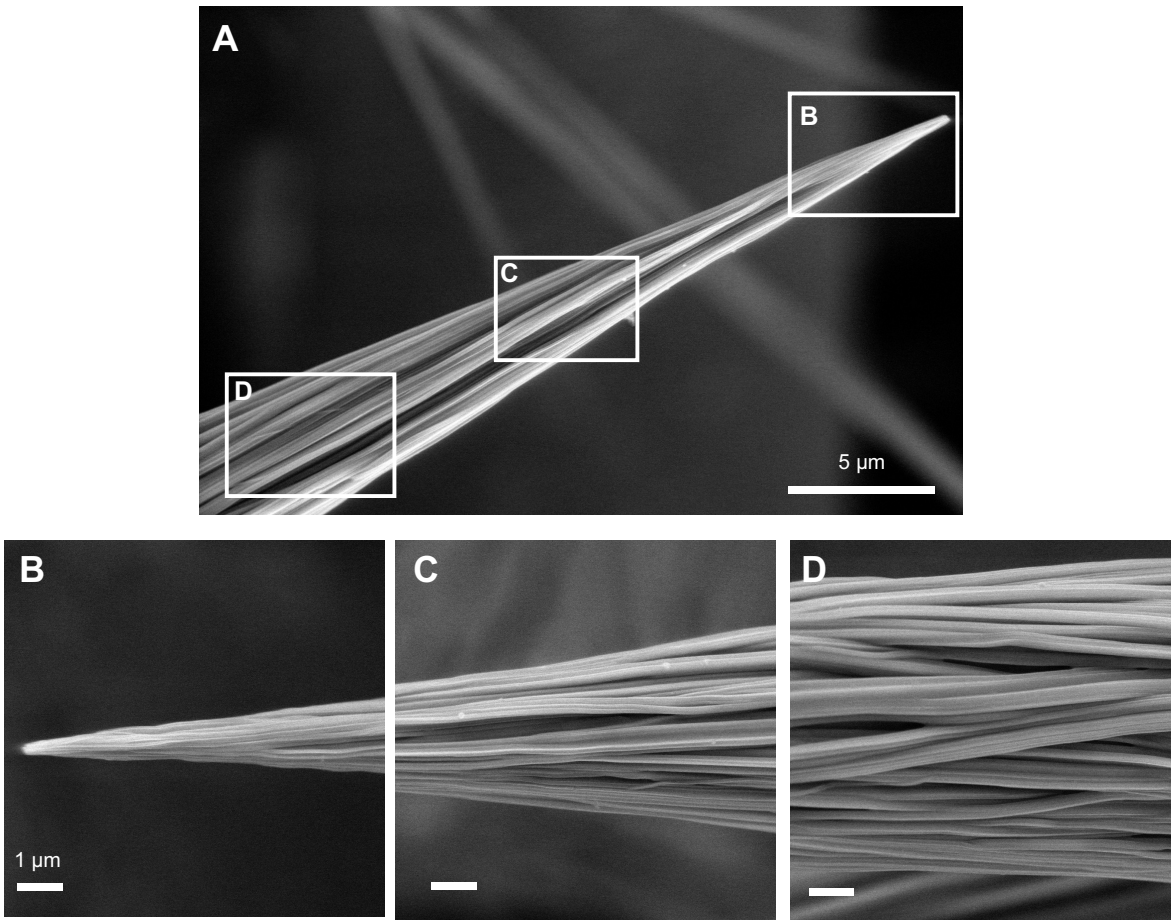

Figure 3.3.6: High-resolution scanning electron microscopy of a single BTA-spine. (**A**) gives the overview of the BTA spine while (**B**) focuses on the tip, (**C**) on the middle, and (**D**) on the base. The scale bars in (**B**-**D**) correspond to 1 µm. Reprinted with permission from [145].

These fibrils were aligned in an orientated and dense way, forming longitudinal microgrooves (Figure 3.3.6 C). At the base, the *i*Pr-BTA fibrils were more randomly oriented, creating a pronounced microgrooved surface (Fig. 3.3.6 D) with average fibril diameters up to 1 µm. The fibrous morphology of the supramolecular spine was further investigated by the cross-sectional SEM micrographs (cf. Figure 3.3.7). A single supramolecular spine was isolated on carbon tape and cut with a razor blade. According to the cross-section, the spine comprised of multiple single fibrils. These fibrils also showed longitudinal orientation parallel to the spine axis. While some fibrils were isolated, most were agglomerated into larger fibril bundles. This morphology resulted in a highly porous inner structure (cf. Figure 3.3.7 C).

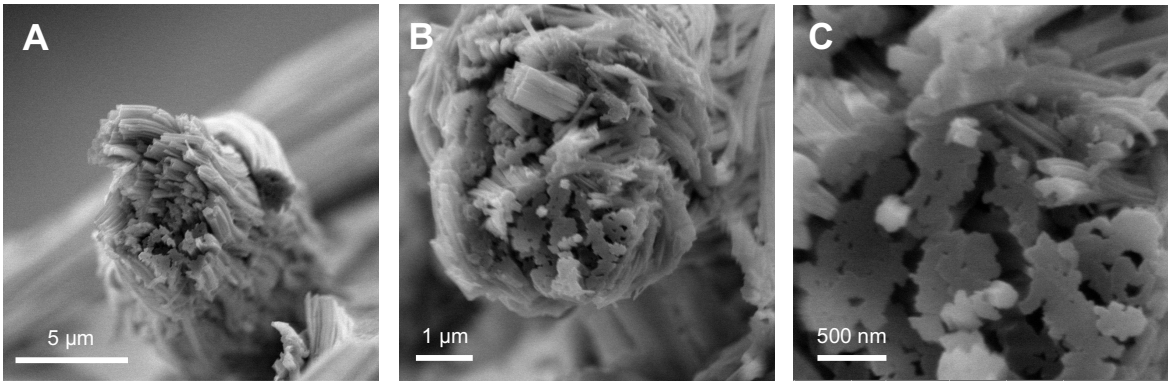

Figure 3.3.7: High-resolution cross-section SEM micrographs of a single *i*Pr-BTA spine. The *i*Pr-BTA was isolated on a carbon tape and cross-sectionally cur with a razor blade to reveal the inner structure.

As shown in Figure 3.3.5 and Figure 3.3.6. the supramolecular spines self-assembled on the tip of the flock fiber. The transition between the base of the highly orientated supramolecular spines and the PA flock fiber tip is shown in Figure 3.3.8. In general, starting from the PET-mesh, BTA fibrils were erratically entwined along the PA flock fiber. The random orientation continued until the BTA fibers reached the tip of the PA flock fiber. Once the *i*Pr-BTA fibers reached the tip of the PA flock fiber, they spread into several highly orientated supramolecular spines. Thus, the supramolecular fibrils were aligned and densely packed with a high degree of order, whereas, at the base of the artificial spine, the arrangement of the supramolecular fibrils deviated from the main orientation axis, resulted in an overall roughness difference along the spine.

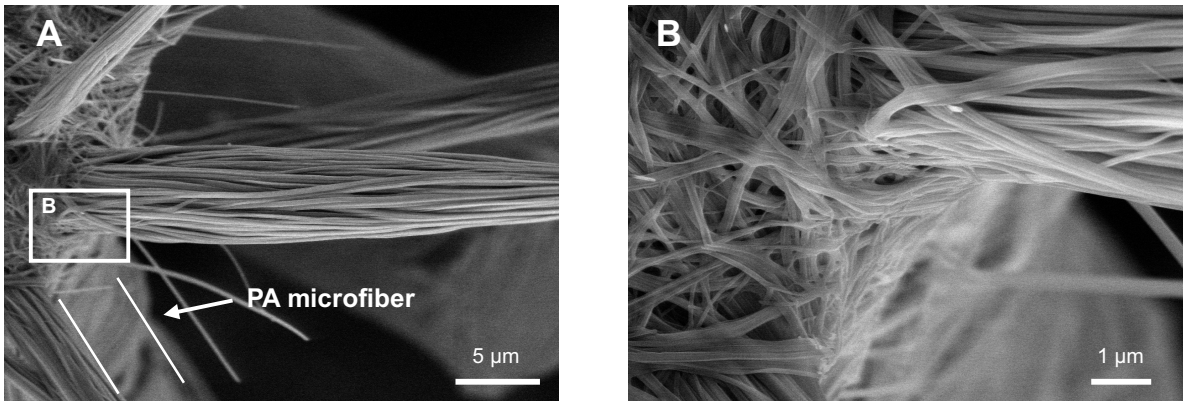

Figure 3.3.8: SEM micrograph of the transition between oriented *i*Pr-BTA spine and PA flock fiber tip. (**A**) Top-view of a PA flock fiber equipped with *i*Pr-BTA spines. The spines are entwined around the flock fiber and spread at the flock fiber head into several oriented *i*Pr-BTA spines. (**B**) focuses on the transition between ordered and randomly oriented *i*Pr-BTA fibrils. Reprinted with permission from [145].

The self-assembly protocol of *i*Pr-BTA in a flocked PA2 substrate gave rise of several supramolecular spines per flock fiber tip. In general, the number of spines varied from around 20 to 110 supramolecular spines per flock fiber, as shown in Figure 3.3.9. On average, 81(8) spines per flock fiber tip with a broad deviation were observed. There were PA flock fibers observed with only 20 supramolecular spines, while other flock fibers were equipped with spines > 100. In general, the supramolecular spines exhibited an average length of about 50(2) µm and a half apex angle of 6(1) deg. Besides the numerical deviation, a morphological deviation was observed. While some spines form spine structures as discussed earlier, also very thin fibrous spines with no measurable apex angles were observed.

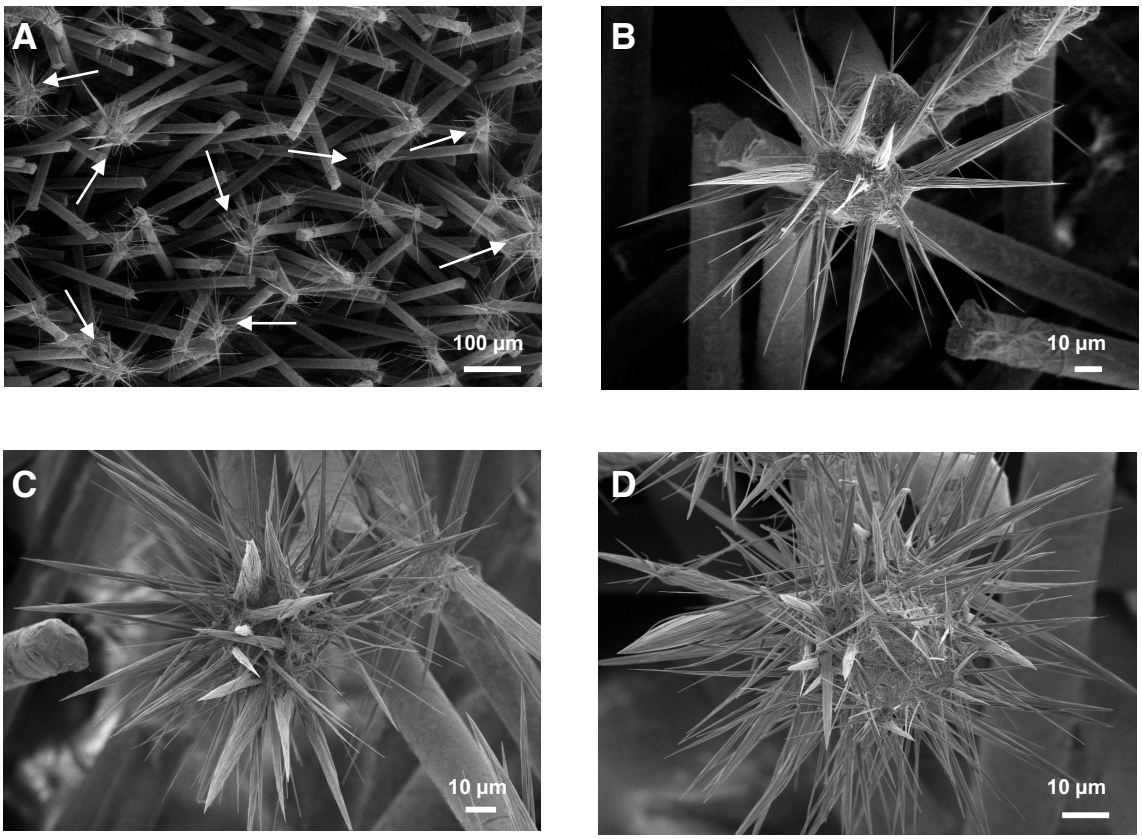

Figure 3.3.9: SEM micrographs of the assembled BTA-spines on top of different PA2 flock fibers. (**A**) gives an overview of micrographs where the white arrows indicate assembled BTA spines. (**C**-**D**) show representative snippets of different *i*Pr-BTA assemblies. Reprinted with permission from [145].

To obtain more information about the molecular self-assembly behavior and phase separation, RAMAN imaging was employed. According to RAMAN imaging (cf. Figure 3.3.10 A, 3.3.10 B), the *i*Pr-BTA (red) and PA (blue) components were clearly identified. The *i*Pr-BTA component formed the supramolecular spine, while the tip of the flock fiber consisted of a mixed phase of *i*Pr-BTA and PA. To investigate the high order within the alignment of *i*Pr-BTA molecules into a columnar arrangement, and thus the orientation of the fibrils along the spines, confocal polarized RAMAN-spectroscopy was utilized (cf. Figure 3.3.10 C, 3.3.10 D). As shown in Figure 3.3.6 D, the benzene ring of the *i*Pr-BTA molecule showed a strong correlation to the angle of the polarizer. When the *i*Pr-BTA molecules self-assembled into a columnar arrangement, the benzene rings were stacked on each other. Measuring with a parallel polarization along the columns reduced the intensity of the signal corresponding to the benzene units.

A measurement with a perpendicular polarizer angle relative to the main axis of the spine, however, increased signal intensity. Thus, the RAMAN-imaging measurement indicates phase separation at the tip of the flock fiber into flock fiber and supramolecular *i*Pr-BTA spine, as well as complete molecular self-assembly of the spine into supramolecular *i*Pr-BTA spine.

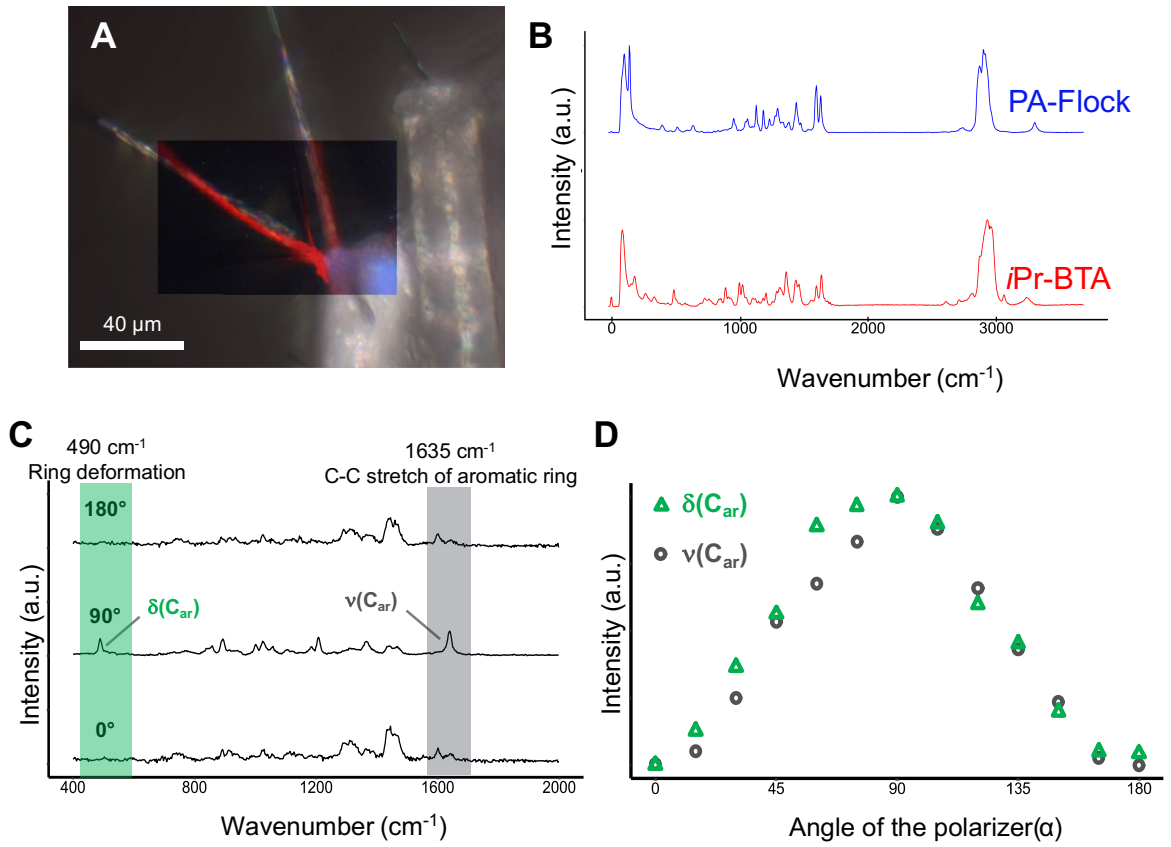

Figure 3.3.10: RAMAN-imaging and polarized RAMAN spectroscopy of the *i*Pr-BTA spine. (**A**) gives the RAMAN-imaging overlay with the corresponding spectrum shown in (**B**). (**C**) show polarized RAMAN spectrum of a single BTA spine with a polarizer angle of 0 deg, 90 deg and 180 deg. The intensity variation of the aromatic stretching and bending vibrations in dependency on the polarizer angle is shown in (**D**). (**C**, **D**) Reprinted with permission from [145].

Self-Assembly Mechanism

It was observed that the three-dimensional morphology of the flocked substrate was crucial for preparing supramolecular *i*Pr-BTA spines. As shown in Figure 3.3.3, *i*Pr-BTA formed evenly round supramolecular fibers upon solvent evaporation on a silicon wafer. However, adapting the same protocol to a flocked structure resulted in the formation of supramolecular spines, as discussed in the previous chapter. In general, BTAs form supramolecular fibers with a distinct morphology depending on the set of conditions, such as selected solvent, concentration, cooling, and evaporation conditions.

For the following experiments, a stable *i*Pr-BTA solution at r.t. and a constant concentration of 0.5 wt% in 2-propanol is used. At these conditions, *i*Pr-BTA forms a stable solution. [125] To get a first impression, the formation of supramolecular spines was observed by optical microscopy. A representative time series of the side- and top view is shown in Figure 3.3.11 and Figure 3.3.12 respectively. For this experiment, the flocked substrate was immersed in the *i*Pr-BTA solution and immediately placed underneath the microscope. The completely wetted flocked substrate is depicted in Figure 3.3.11 A (t_0), where the white dashed line indicates the solvent level and the arrow, the distance between the solvent level and the substrate. After a few seconds, the solvent level decreased and wetted the flock fibers. At the same time, the *i*Pr-BTA solution rose to the tip of the flock fibers. Here, the evaporation rate of the solvent was significantly increased and *i*Pr-BTA self-assembly occurred. This process was repeated until the supramolecular spine was formed and no *i*Pr-BTA solution was left (cf. Figure 3.3.11 D, t_E). During this process, a continuous solvent transport from the base of the flock fibers to the tip of the supramolecular *i*Pr-BTA spines was observed. In the last step, the wetted spines dried. As shown in Figure 3.3.12, the wetted iPr-BTA spine had a translucent appearance. When all *i*Pr-BTA solution was consumed, the supramolecular spines dried and *i*Pr-BTA fibers from the tip to the bottom of the flock fibers were formed (cf. Figure 3.3.12 C). The overall self-assembly process toward supramolecular *i*Pr-BTA spines was completed over a few minutes. While this experiment gave valuable insight into the solvent transport and self-assembly process, it is important to highlight that the described observations did not describe the complete system. Due to the open system and thermal input of the illumination, a faster evaporation rate is introduced to the system and therefore significantly increases the evaporation rates. The increased evaporation rates led to less defined spines. However, it is assumed that the mechanism of the molecular self-assembly toward supramolecular spines proceeds similarly.

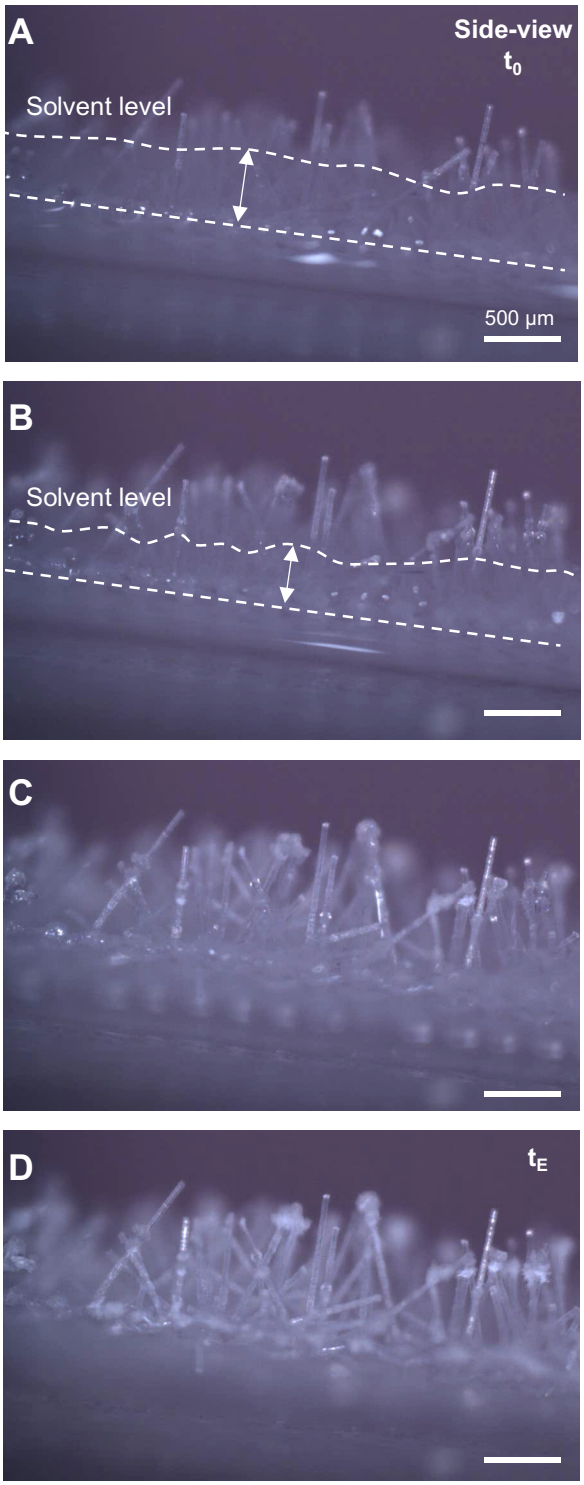

Figure 3.3.11: Side view of *in-situ* molecular self-assembly of *i*Pr-BTA in a flocked substrate. (**A**) gives the flocked substrate immersed in the *i*Pr-BTA solution at the starting point t_0. The white dashed lines indicate the maximum and minimum solvent level, and the arrow estimates the respective distance. (**B-C**) show the proceeding evaporation, while (**D**) corresponds to the completely dried flocked substrate with the supramolecular spines at the tip of the flock fibers. t_0 and t_E correspond to the end and start point of the self-assembly process respectively. The scale bars in (**B-D**) are 500 µm.

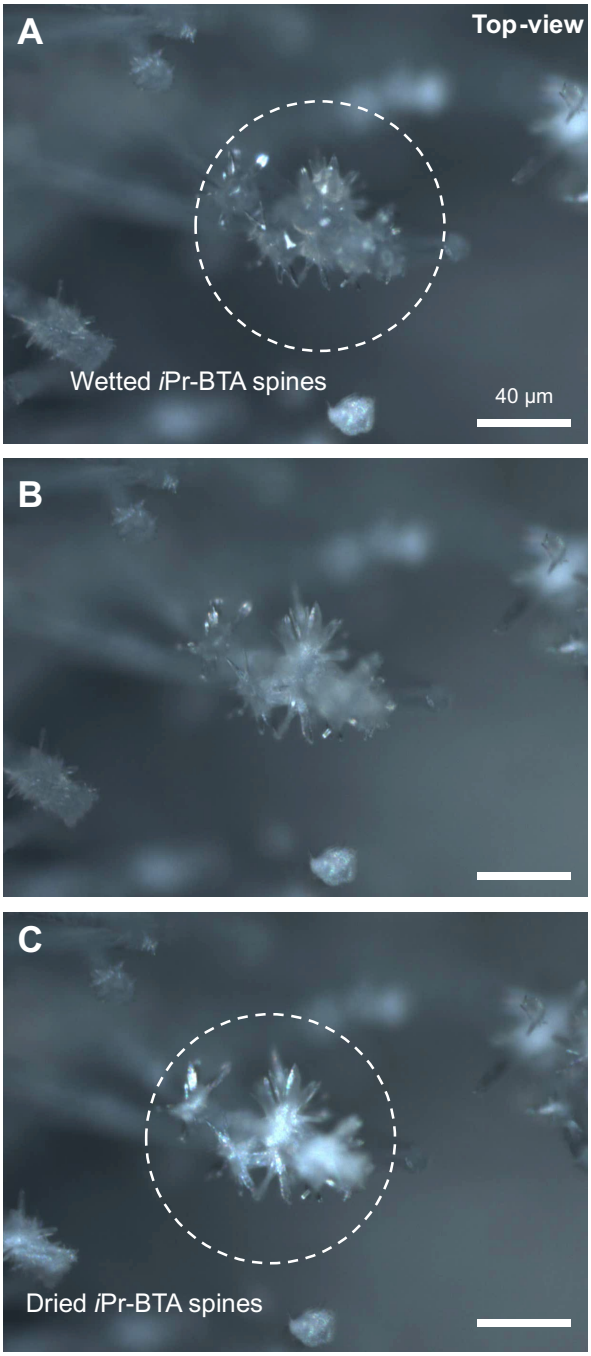

Figure 3.3.12: Top view of *in-situ* molecular self-assembly of *i*Pr-BTA in a flocked substrate. (**A**) shows the supramolecular spines, still wetted by the *i*Pr-BTA solution. (**B**) gives the state of the supramolecular spines during continuous evaporation, while (**C**) shows the final completely dried supramolecular spines.

The self-assembly utilizing the flocked substrate is hypothesized to occur in several crucial steps. These steps are schematically depicted in four subsequent stages in Figure 3.3.13. In the first step, the flocked substrate is immersed in an *i*Pr-BTA solution, completely filling the pores of the flocked substrate. Afterward, the flock is placed on filter paper to remove the *i*Pr-BTA solution partially. During evaporation, capillary forces of the vertically aligned flock fibers transport the *i*Pr-BTA solution toward the top of the flock fiber. When reaching the tip of the flock fiber, evaporation occurs. Upon evaporation of the solvent, the concentration of the *i*Pr-BTAs increases, and nuclei are formed to initiate site-specific self-assembly and supramolecular fiber growth. As evaporation proceeds, additional *i*Pr-BTA building blocks are fed to the initially formed BTA fibrils. This process continues until most of the *i*Pr-BTA solution in the flocked substrate is consumed. Due to the concentration gradient between the pores of the flocked structure and the partially formed supramolecular spine, a depletion front is formed, resulting in hierarchical fibrils that eventually develop conical tips. Close to the end of the evaporation process, when the solution transport nearly stops, round *i*Pr-BTA fibers entwine along the flock fibers and at the bottom of the substrate are formed. The described process is completed within a couple of minutes. Since the self-assembly mechanism is capillary-driven, the local morphology of the flocked substrate has a significant influence on the resulting morphology of the supramolecular spine. Due to the random azimuthal orientation of the flock fibers, some spines have access to more *i*Pr-BTA solution than other spines, resulting in a large deviation of supramolecular spines with different sizes and flock fibers equipped with different numbers of supramolecular spines.

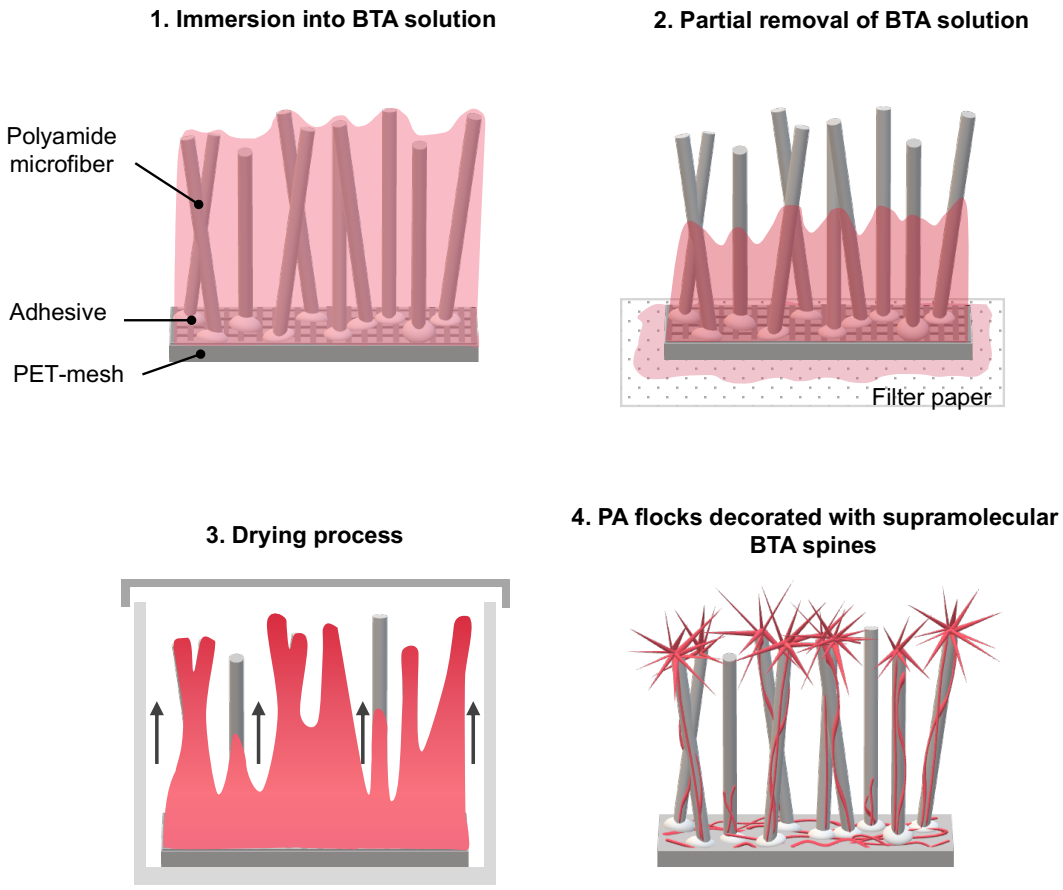

Figure 3.3.13: Schematic representation of the self-assembly in a flocked substrate toward BTA spines. The flocked substrate is first dip-coated in a BTA solution, followed by partial removal of the solution with filter paper. Afterward, the solution is evaporated while being transported by capillary forces to the tip of the flock fibers. Here, the BTA forms the spine structure due to the continuous depletion of the molecular building block and evaporation of the solution at the tip of the flock fibers. Reprinted with permission from [145].

The described guided evaporation-induced self-assembly is supported by observing the drying process by optical microscopy as well as performing several negative experiments as described in the following. In this context, the BTA peripheric unit is first investigated. The series from N^1, N^3, N^5-tri[2-(dimethyl amino)-ethyl]-1,3,5-benzenetricarboxamide (Me-BTA), N^1, N^3, N^5-tri[2-(diethyl amino)-ethyl]-1,3,5-benzenetricarboxamide (Et-BTA), N^1, N^3, N^5-tri[2-(dipropyl amino)-ethyl]-1,3,5-benzenetricarboxamide (*n*Pr-BTA) to *i*Pr-BTA follows the trend of decreased hydrophilicity and increased solubility in 2-propanol (Figure 3.3.14). [126] Furthermore, a BTA with a methyl ester of L-methionine in the peripheric unit (Methionine-BTA) was added to the series, which shows an even lower solubility in 2-propanol. Methionine-BTA is only soluble in 2-propanol at elevated temperatures and forms fibers already upon cooling (Figure 3.3.14 C).

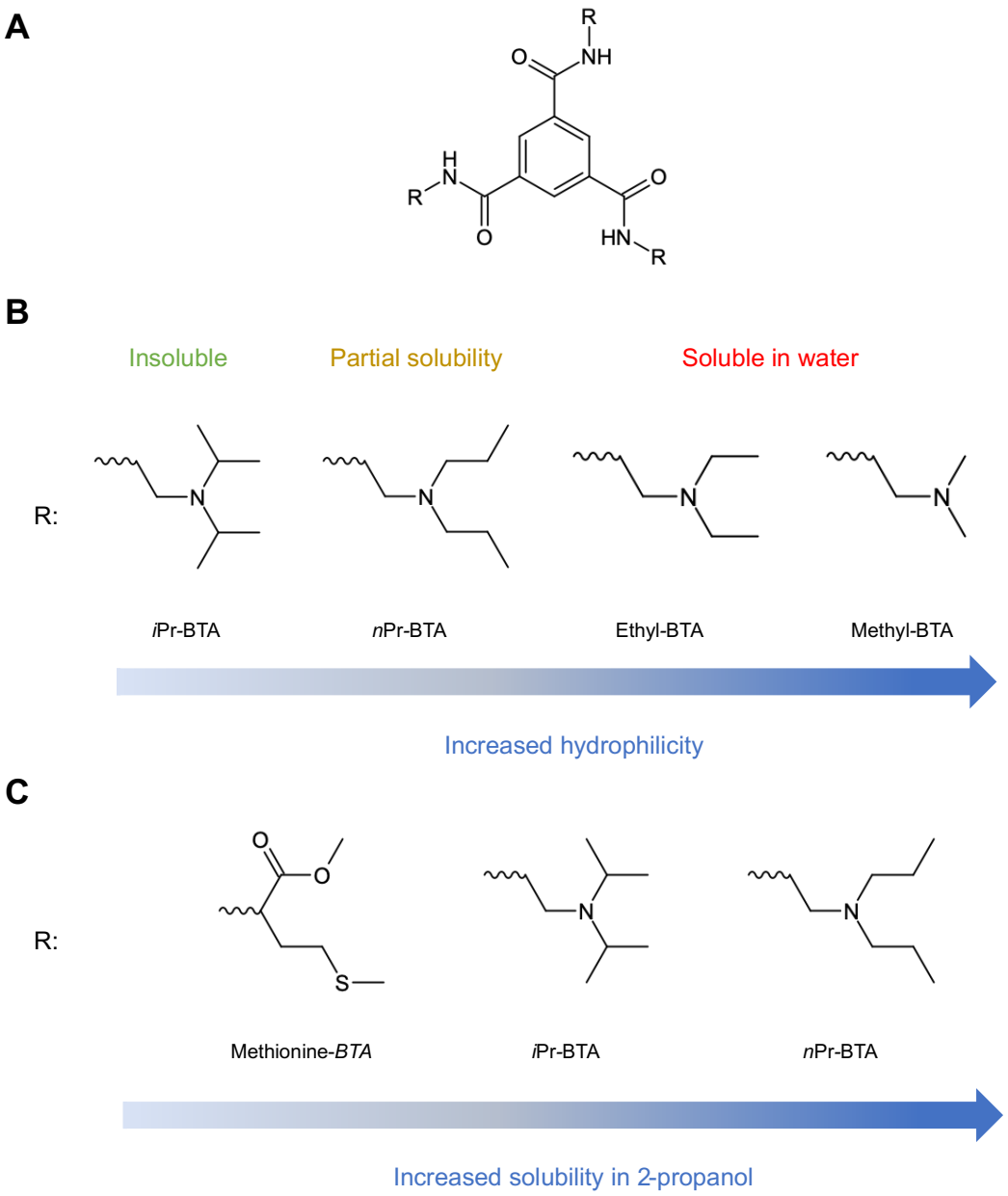

Figure 3.3.14: Overview of the tested BTAs and their water wettability and solubility in 2-propanol. (**A**) gives the molecular building block, while (**B**) shows the dependency of the periphery to the hydrophilicity and (**C**) to the solubility in 2-propanol.

As shown in Figure 3.3.15 A, Methionine-BTA formed upon cooling a spider web-like morphology between the single PA flock fibers. This is attributed to the low solubility of Methionine-BTA in 2-propanol. Upon cooling, Methionine-BTA immediately started to self-assemble, and no concentration gradient between the flock fibers and the tip of the flock fiber occurred.

On the other hand, *n*Pr-BTA, which has an increased solubility in 2-propanol than *i*Pr-BTA, did not form supramolecular spines upon solvent evaporation (cf. Figure 3.3.15 B). Upon evaporation, entwined supramolecular fibers were formed around the PA flock fibers. This behavior suggests that the BTA concentration needs to be close to the stable solution concentration. For *i*Pr-BTA, this concentration is at 0.5 wt. %, while for *n*Pr-BTA at a significantly higher concentration due to the increased solubility in 2-propanol. Besides the specific peripheric unit, also the specific solvent had a significant influence on the self-assembly behavior. By dissolving *i*Pr-BTA in DMF, no supramolecular spines were observed due to the decreased vapor pressure of DMF and, therefore, the decreased evaporation rate of the solvent at the flock fiber tip with respect to 2-propanol (cf. Figure 3.3.15 C). [127,128] Therefore, it is suggested that 2-propanol, as a solvent with sufficient vapor pressure, is needed.

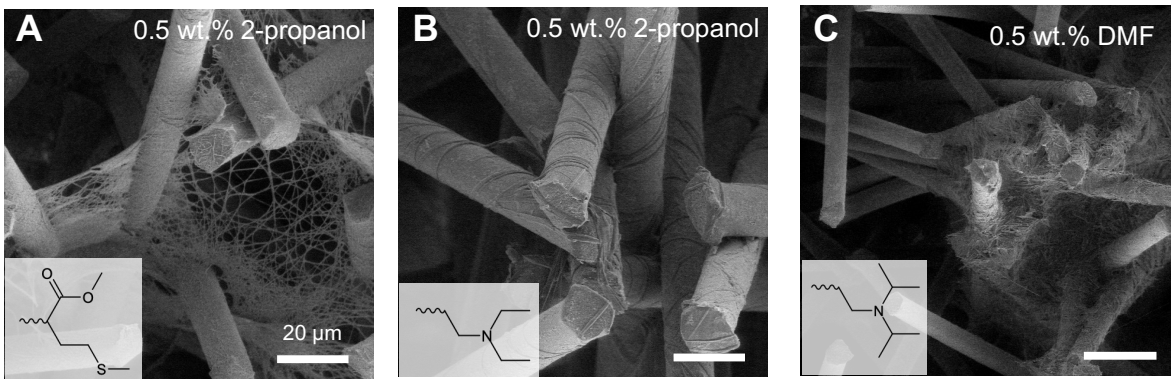

Figure 3.3.15: Self-assembly of different BTAs in a PA2 flocked substrate. (**A**) shows the *i*Pr-BTA assembly in DMF, (**B**) of Methionine-BTA, and (**C**) of Et-BTA in 2-propanol. The scale bars in the (**B**, **C**) correspond to 20 µm.

While the peripheric unit of the BTA and the respective solvent are essential for the self-assembly of supramolecular spines, the specification of the flock is expected to be crucial as well. As mentioned earlier, the BTA solution is transported from the base to the tip of the flock fiber. It is assumed that the solvent cannot overcome the structure at a certain flock fiber length before evaporation at the flock fiber tip occurs. The fabrication of supramolecular spines was already shown with PA2 flocks. Hence, PA3 and PA4 flocks were tested as well with a flock fiber length of 2 mm and 6 mm, respectively (cf. Table 3.1.1). As shown in Figure 3.3.16 A., the *i*Pr-BTA spines assembled at the tip of the flock fiber. However, due to the decreased stiffness of the PA3 flock fiber, the single flock fibers were not isolated but rather agglomerated to flock fiber bundles (cf. Figure 3.3.16 B). This resulted in the bending of several PA3 flock fiber tips toward the self-assembled *i*Pr-BTA.

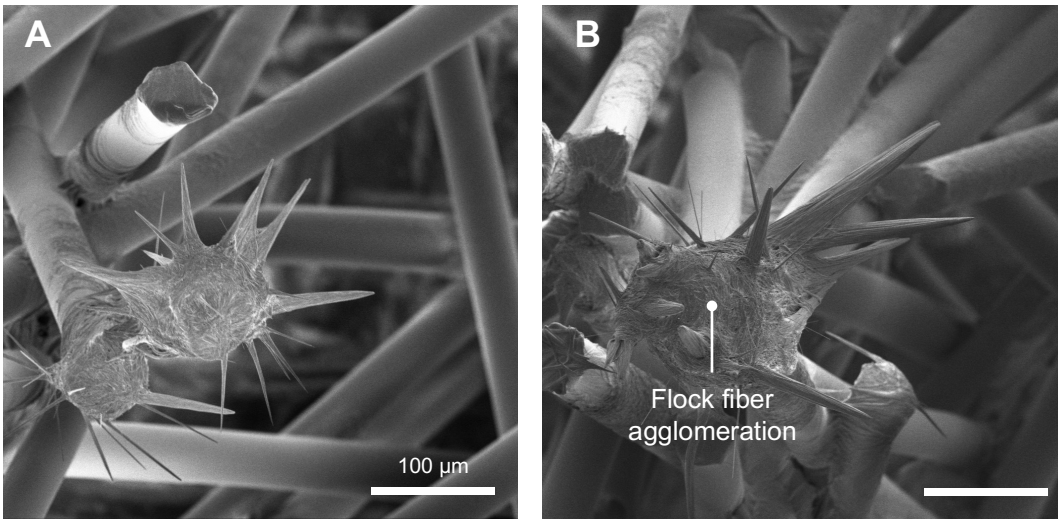

Figure 3.3.16: SEM micrographs of assembled *i*Pr-BTA-spines in a PA3 flocked substrate. (**A**) gives an overview micrograph while (**B**) focuses on the assembled spines. The scale bar in (**B**) corresponds to 100 µm.

This observed flock fiber agglomeration was even more expressed by the longer PA4 flock fibers (cf. Figure 3.3.17). It is hypothesized that the pressure on the fiber induced by solvent evaporation and self-assembly led to the agglomerated morphology. Due to the assembled *i*Pr-BTA fibers, the flock fibers were held in place. Furthermore, closer observation of the self-assembled *i*Pr-BTA revealed that self-assembly of the supramolecular spines occurred in a PA4 flocked substrate below the tip of the flock fiber, as depicted in Figure 3.3.17 B. The assembly at the middle of the flock fiber is also shown in Figure 3.3.18.

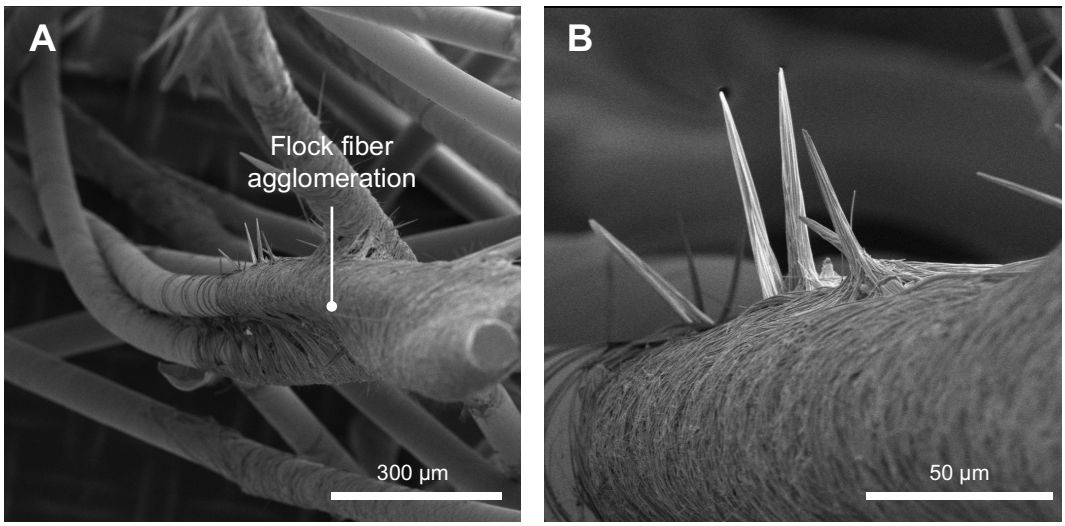

Figure 3.3.17.: SEM micrographs of agglomerated PA4 flock sample. (**A**) shows the overview, and (**B**) focuses on the spine.

At a higher magnification, no significant *i*Pr-BTA assembly was visible at the tip of the flock fiber (cf. Figure 3.3.18 B). This observed phenomenon indicates limited upward migration of the *i*Pr-BTA solvent front before self-assembly was triggered due to solvent evaporation. Therefore, concluding that a flock fiber length > 6 mm does not result in supramolecular spine formation at the tip of the flock fiber.

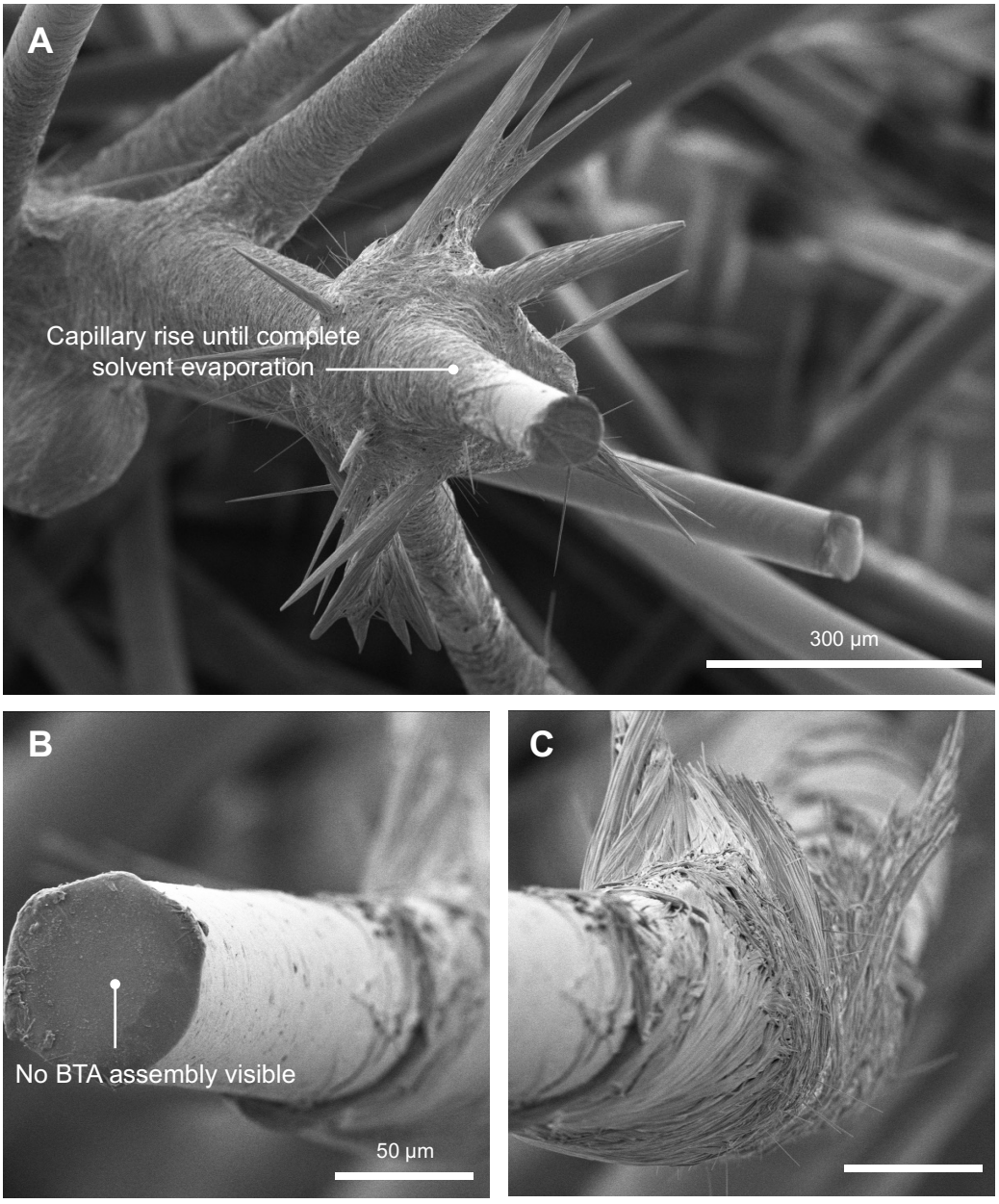

Figure 3.3.18: SEM micrographs of assembled BTA-spines in a PA4 flocked substrate. (**A**) shows an overview. (**B**) focuses on the PA4 flock fiber tip, where no *i*Pr-BTA assembly is visible, and (**C**) on the middle part of the PA4 flock fiber. The scale bar in (**C**) corresponds to 50 µm.

To summarize, the study revealed several crucial self-assembly conditions toward supramolecular spines. 1.) The solvent of the BTA needs to have a low vapor pressure to facilitate the evaporation rate. 2-propanol, as a nontoxic solvent with sufficient vapor pressure and good solubility of the BTA analogon was chosen. 2.) The BTA needs to be water stable, which excludes Me-BTA, Et-BTA, and *n*Pr-BTA from the series. 3.) The solubility of the BTA in the respective solvent must be high enough to form a stable solution at room temperature. 4.) The concentration of the BTA should be close to the stable solubility concentration. These requirements exclude Methionine-BTA, leaving *i*Pr-BTA as a viable option. 5.) The flock fibers need to have sufficient stiffness, excluding viscose, while suggesting the use of PA flock fibers. However, the bending modulus depends on the fiber diameter and length. If the flock fiber is too thin and long, the flock fibers bend during BTA assembly and form larger agglomerates. Furthermore, if the flock fiber is too long, the solution cannot climb to the flock fiber tip but rather start assembling the spine below the flock fiber tip. Therefore, PA2 flock fibers were chosen due to sufficient stiffness and decreased fiber length to ensure the assembly of supramolecular spines on the tip of the flock fibers.

Water Transport

As already mentioned in Chapter 1, the unidirectional water transport from the tip to the base for cacti spines is mainly attributed to a LAPLACE pressure difference due to conical geometry, longitudinal microgrooves, and a wettability gradient. [31,36,37] Combining these structural features in artificial spines results in the directional transport of water droplets. [31] The *i*Pr-BTA spines show all these features, including conical geometry, longitudinal microgrooves due to the alignment of the supramolecular fibrils, and a wettability gradient due to roughness difference increasing from the tip to the base. [27] To characterize the interaction of *i*Pr-BTA with water, the spines were isolated and investigated by ESEM at a constant water vapor pressure of 720°Pa (cf. Figure 3.3.19). The first row of Figure 3.3.19 depicts the water condensation of a PA flock fiber in the ESEM chamber upon cooling, while the second row gives the water condensation on an isolated supramolecular spine. During the measurement, the stage and, subsequently, the spines were cooled from 3.9°C to 1.9 °C at a cooling rate of 1 °C min^{-1}, reaching the dew point at 2.0°C under these conditions. The initial state prior to water condensation is shown in Figure 3.3.19 A and 3.3.19 D for PA and the supramolecular spine, respectively.

As already discussed in Chapter 3.1, PA flock fiber showed droplet formation while reaching the dew point (Figure 3.3.19 A), revealing a hydrophobic surface. On the other hand, cooling the *i*Pr-BTA spine to the dew point resulted in complete wetting and filling of the microgrooves with a larger accumulation of water at the base (Figure 3.3.19 F). This pronounced spreading across the supramolecular spine suggests a hydrophilic surface. [112] Upon further cooling to 1.9 °C, water condensation proceeds. Simultaneously, directional water transport from the tip toward the base of the *i*Pr-BTA spine occurred, as indicated by the formation of a droplet reservoir at the base. (Figure 3.3.19 F).

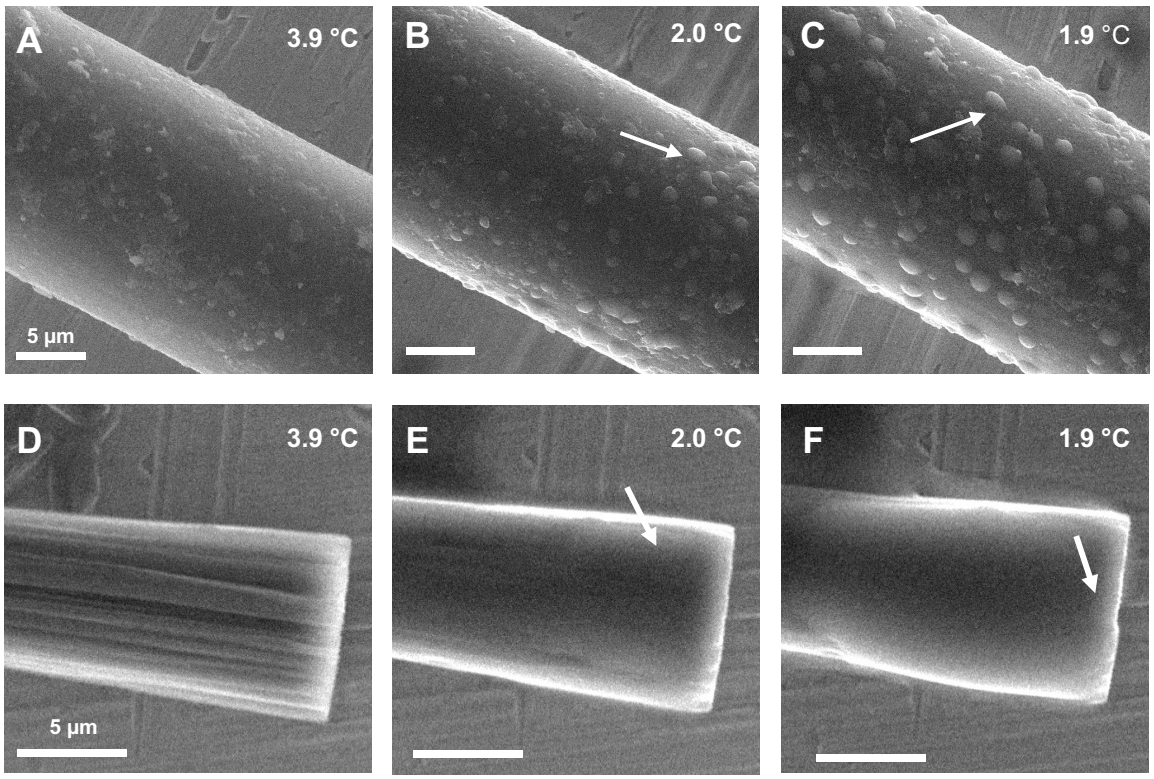

Figure 3.3.19: ESEM micrographs of a PA-flock fiber and an isolated *i*Pr-BTA-spine. (**A**-**C**) shows the PA2-flock fiber and (**D**-**F**) the isolated *i*Pr-BTA-spine. The relative water vapor pressure was kept at 720 Pa while the stage temperature was slowly lowered to the dew point. The white arrows indicate water condensation on the respective sample. The scale bars in (**B**-**F**) correspond to 5 µm. Reprinted with permission from [145].

To demonstrate the unidirectional water transport of droplets, the supramolecular spines were irrigated with fog while monitoring the spine by optical microscopy. In Figure 3.3.20, a group of supramolecular spines was continuously irrigated by fog. There, droplets were collected by the supramolecular spine tips and quickly transported toward the base. The transport velocity of this initial droplet transport was estimated to be ~ 150 µm s^{-1}.

Compared to the well-investigated model cactus *O. microdasys* (~12 µm s^{-1}), [31,129,130] the water droplet transport velocity of the supramolecular spines significantly exceeds the velocity of the natural spine. It was further observed that due to the hydrophilic wettability of the supramolecular spine, the first droplets were wetting the spine and forming a precursor water film. Once the spine was sufficiently wetted, the following droplets started to spread, resulting in a water film along the supramolecular spine. This water film gave rise to increased water transport, exceeding the temporal detection limit of the optical microscope. Here, the decrease of friction force during motion accelerated the droplet significantly. This effect has already been observed in literature and is referred to as the "lubrication effect". [119] Besides the decreased friction, the spreading of the water droplet resulted in a higher LAPLACE pressure difference due to an increase of R_1 and R_2 at the opposite sides of the droplet (cf. Equation 1.10). The decreased friction, as well as the increased LAPLACE pressure, significantly increased the droplet transport velocities.

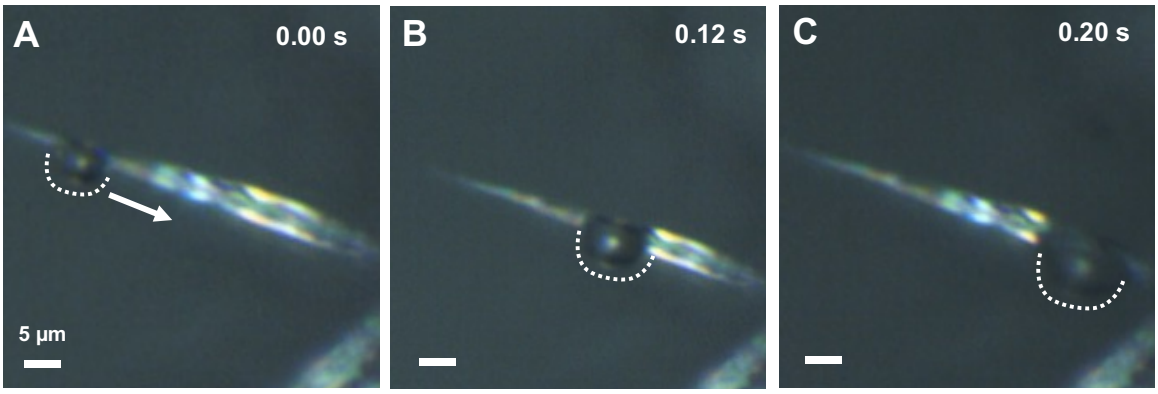

Figure 3.3.20: Optical microscopy micrographs of the *i*Pr-BTA-spine during fog irrigation. (**A**-**C**) shows the top view of the assembled *i*Pr-BTA spine during continuous fog irrigation at different time intervals. The white dashed line indicates the position of the water droplet. The scale bars in the figure correspond to 5 µm. Reprinted with permission from [145].

In conclusion, a fabrication protocol of biomimetic cacti-spines by the molecular self-assembly of *i*Pr-BTA in a flocked substrate was developed. The spines were obtained by a simple immersion process, which may be readily adapted to larger scales. Notably, the supramolecular spines exhibited both structural and functional similarities to natural cacti spines while exceeding fog droplet transport velocities compared to natural cacti spines significantly. Besides fog capture, the unique properties and structure of the supramolecular spine may be used for diverse applications, such as thermal insulation or coalescence filtration. However, before implementing these structures in industrial applications, the brittle mechanical properties of the *i*Pr-BTA must be addressed. At last, the study highlighted the potential of flocked substrates. The property as structure-directing material may be of relevance beyond the investigated BTA systems.

3.4. Flock Fibers with a Dandelion-Seed Morphology

Besides the water-collecting capabilities of cacti spines or Namib desert beetles, Dandelion seeds show an unusual interaction with water. This interaction relies on capturing water droplets and then coalescing these droplets into larger droplets. [52,53] In general, the functionality of the water capture and transport mechanism shows similarities to the water collecting mechanism of the Namib desert beetle. However, the structure to achieve this mechanism is quite different. While the Namib desert beetle takes advantage of a structured backplate with hydrophilic and hydrophobic spots, the Dandelion seed evolved a fiber-based morphology. The Dandelion seed consists of a branched filament head, referred to as a pappus, that merges into a single stem. At the base of the stem, the seed is attached. Due to this unique morphology, fabricating structures inspired by Dandelion seeds are generally challenging to implement. As a result, only a limited number of methods have been documented in the scientific literature. [131–134] These fabrication strategies include laser micromachining [134], photolithography and etching [133], precise cutting [131], or gluing the structures [132]. These strategies are labor-intensive and not easily scalable. In order to simplify the fabrication process and investigate the interaction with fog, a flock-based approach was developed. The fabricated Dandelion-seed inspired structures were then implemented toward a fog harvesting device. To the best of the author's knowledge, there is no existing scientific literature on the utilization of artificial Dandelion seeds for the purpose of fog harvesting applications.

Sample Preparation and Morphology

The flock-based approach toward Dandelion-inspired flock fibers relies on sequential stacking and flocking of different flock fibers. This technique provides a cost-effective and versatile alternative to the reported fabrication approaches, as it enables the utilization of commercially available flock fiber materials as well as different substrates on a larger scale. A schematic illustration of the fabrication process is shown in Figure 3.4.1. The initial step in creating the Dandelion-seed-inspired flock system involved applying the first flock layer to a cylindrical substrate (cf. Figure 3.4.1 A).

The substrate employed in this study was made up of wooden sticks which had a cross-sectional diameter of 2 mm. Once the first flock layer was cured, washed, and dried, the tip of the flock fibers was selectively modified with an adhesive droplet. To achieve the selective application of an adhesive droplet, a thin adhesive film was first applied to a glass slide. Subsequently, the flocked substrate was carefully pressed into the adhesive layer so that only the flock fiber tips were submerged (cf. Figure 3.4.1 B). It is highlighted that using a cylindrical substrate facilitates the application of the adhesive droplet. On a cylindrical substrate, the pore size increases, leading to isolated flock fibers due to the curvature of the substrate. On the other hand, on a flat substrate, flock fibers generally self-stabilize and lean against each other. In the last step, a second layer of flock fiber was applied, then cured, and washed to obtain the Dandelion-seed-inspired morphology (cf. Figure 3.4.1 C).

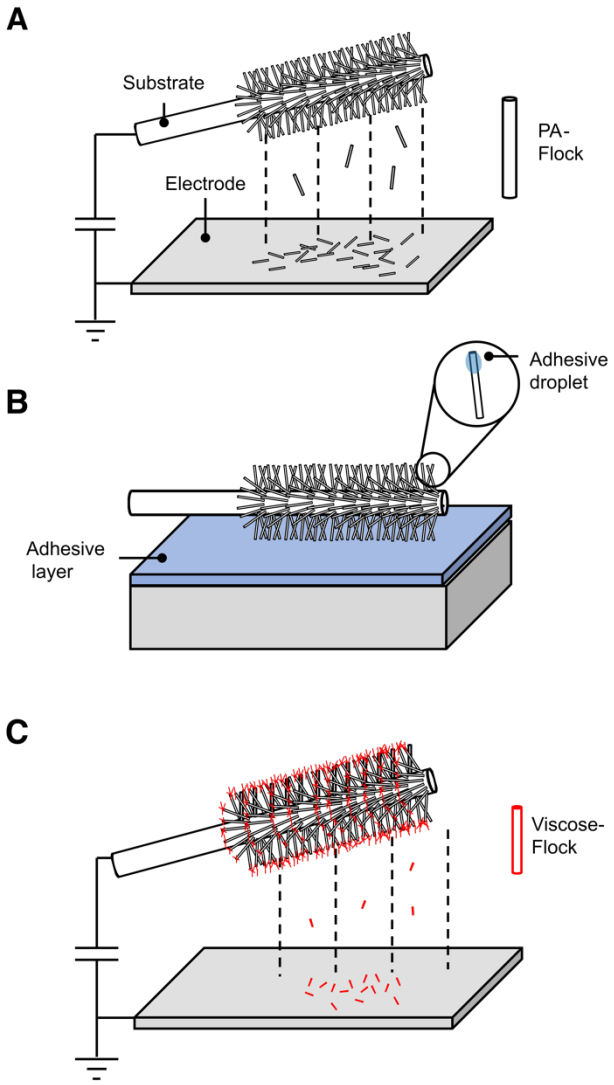

Figure 3.4.1: Schematic illustration of the preparation steps. (**A**) The substrate is first covered with an adhesive layer and then flocked with PA3 flock fibers. (**B**) After curing the adhesive layer, the flock is cleaned and rolled in an adhesive layer to selectively apply an adhesive droplet at the tip of the PA3 flock fibers. (**C**) Finally, viscose flock fibers are applied by electrostatic flocking. The sample is then cured and cleaned again to obtain the final Dandelion inspired morphology.

After curing and cleaning the sample, a flock fiber morphology similar to that of a Dandelion seed was obtained, as shown in Figure 3.4.2. The viscose flock fibers correspond to the branched filament of the seed and the PA3 flock fibers to the stem. Even though the morphology shows strong similarities, the length scales are different. While Dandelion seeds generally are in the range of a few centimeters [135], the proposed fabrication scheme results in artificial fibers with a length of 2-3 mm.

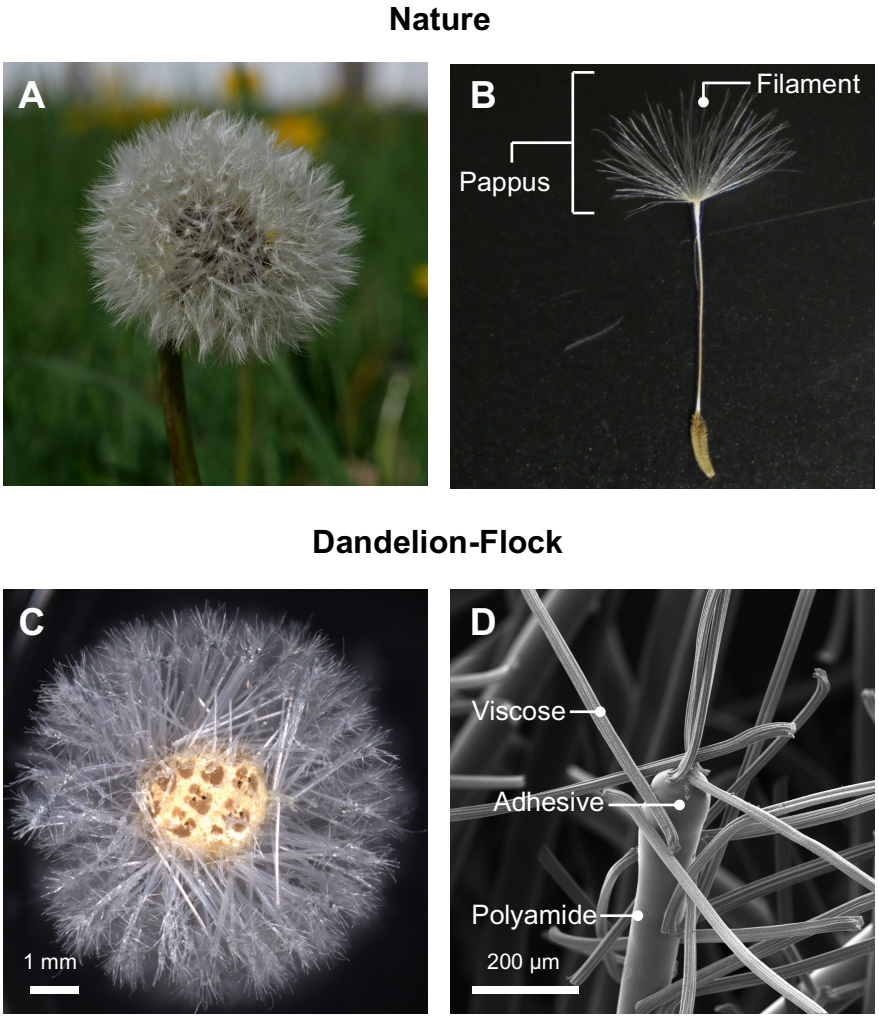

Figure 3.4.2: Comparison of a Dandelion seed with the prepared dandelion flock. (**A**, **B**) shows a photograph of a Dandelion flower with a single seed respectively. (**C**) optical microscopy micrograph of the cross-section of the prepared Dandelion flock sample. (**D**) SEM micrograph of a single Dandelion flock fiber.

In general, the fabrication method offers flexibility in utilizing various flock fibers. However, to limit the sample matrix, the choice of flock fibers was restricted to PA3 (d/l = 22 dtex/2 mm) for the first and V1 (1.7 dtex/0.5 mm), V2 (3.3 dtex/0.5 mm), and V3 (5.6 dtex/1 mm) for the second flock layer. The corresponding Dandelion-inspired flock samples are referred to as PA3V1, PA3V2, and PA3V3. An overview of the sample morphology with optical and SEM micrographs is depicted in Figure 3.4.3. The PA3 flock fibers, as shown in Figures 3.4.3 A, 3.4.3 D, and 3.4.3 G, were evenly distributed over the cylindrical substrate with a vertical orientation (Figures 3.4.3 B, 3.4.3 E, and 3.4.3 H). While the PA3 flock fibers were attached to the substrate, viscose flock fibers were anchored in adhesive droplets at the tip of the PA3 flock fibers (Figures 3.4.3 C, 3.4.3 F, and 3.4.3 I). The orientation of the viscose on the tip of the PA flock fibers was random.

Furthermore, not all viscose flock fibers were anchored by the flock fiber's base. Some viscose flock fibers were also attached by the middle part of the flock fiber, which is attributed to the chaotic nature of the flocking process. Due to air resistance and inhomogeneous charge distribution, flock fibers generally spin during electrostatic acceleration. [88] Therefore, the fibers were anchored according to the spin angle when hitting the tip of the PA flock fiber. The limited space available at the PA flock fiber tip further facilitates random orientation. The overall PA3 flock density was 19(1) mg/cm². Depending on the specific sample, the Dandelion flock showed similar densities of 22(1) mg/cm², 22(2) mg/cm², and 23(1) mg/cm² for PAV1, PAV2, and PAV3, respectively. Optical microscopy images of reference samples without the Dandelion-seed morphology are given in Figure 3.4.4.

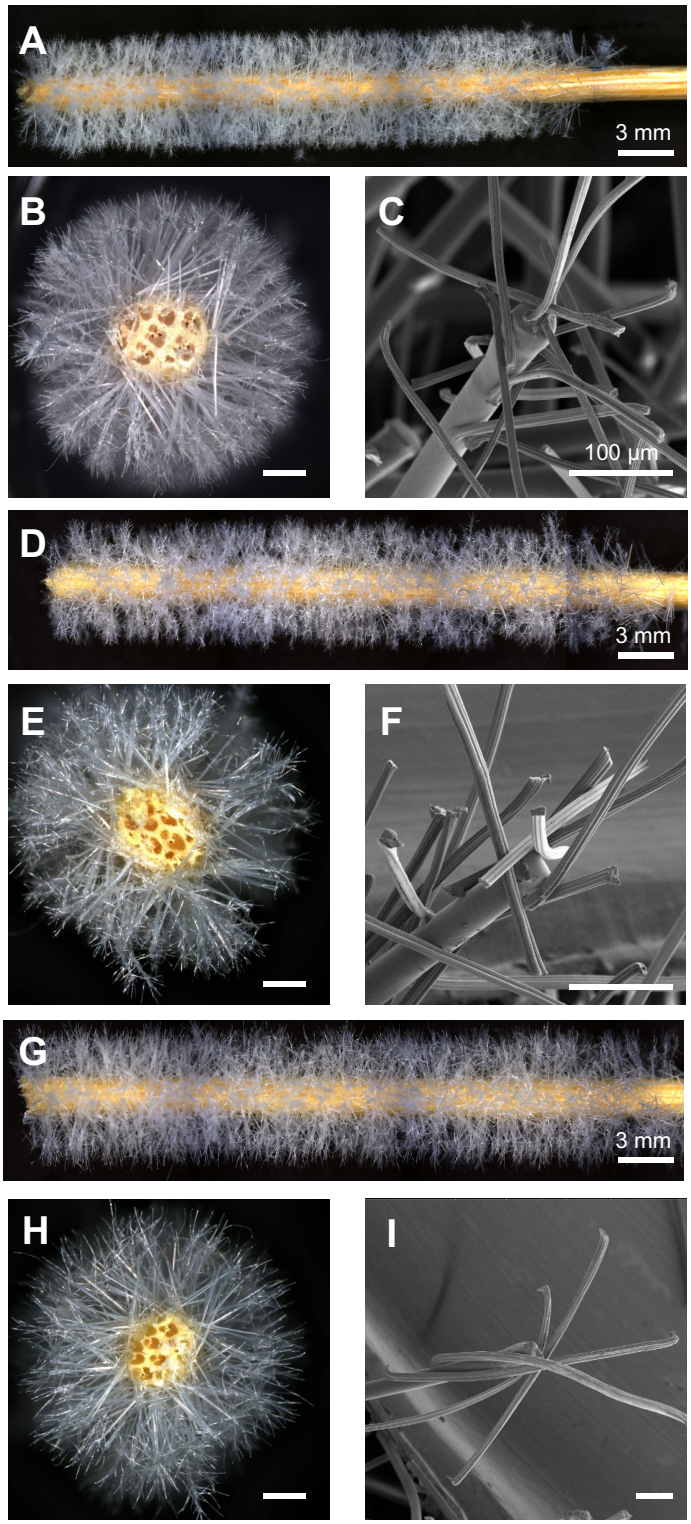

Figure 3.4.3: Overview of the fabricated Dandelion-inspired flock samples. (**A**, **D**, **G**) show the top-view of the polyamide (22 dtex/2 mm) (PA3) and viscose (1.7 dtex/0.5 mm, PA3V1), viscose (3.3 dtex/0.5 mm, PA3V2), and viscose (5.6 dtex/1.0 mm, PA3V3) samples. (**B**, **E**, **H**) give the corresponding crosssection images of PA3V1, PA3V2, and PA3V3. (**C**, **F**, **I**) are scanning electron microscopy micrographs of a single Dandelion-flock fiber for PAV1, PAV2, and PAV3. The scale bars in (**A**, **D**, **G**), (**B**, **E**, **H**), and (**C**, **F**, **I**) correspond to 3 mm, 1 mm, and 100 µm, respectively.

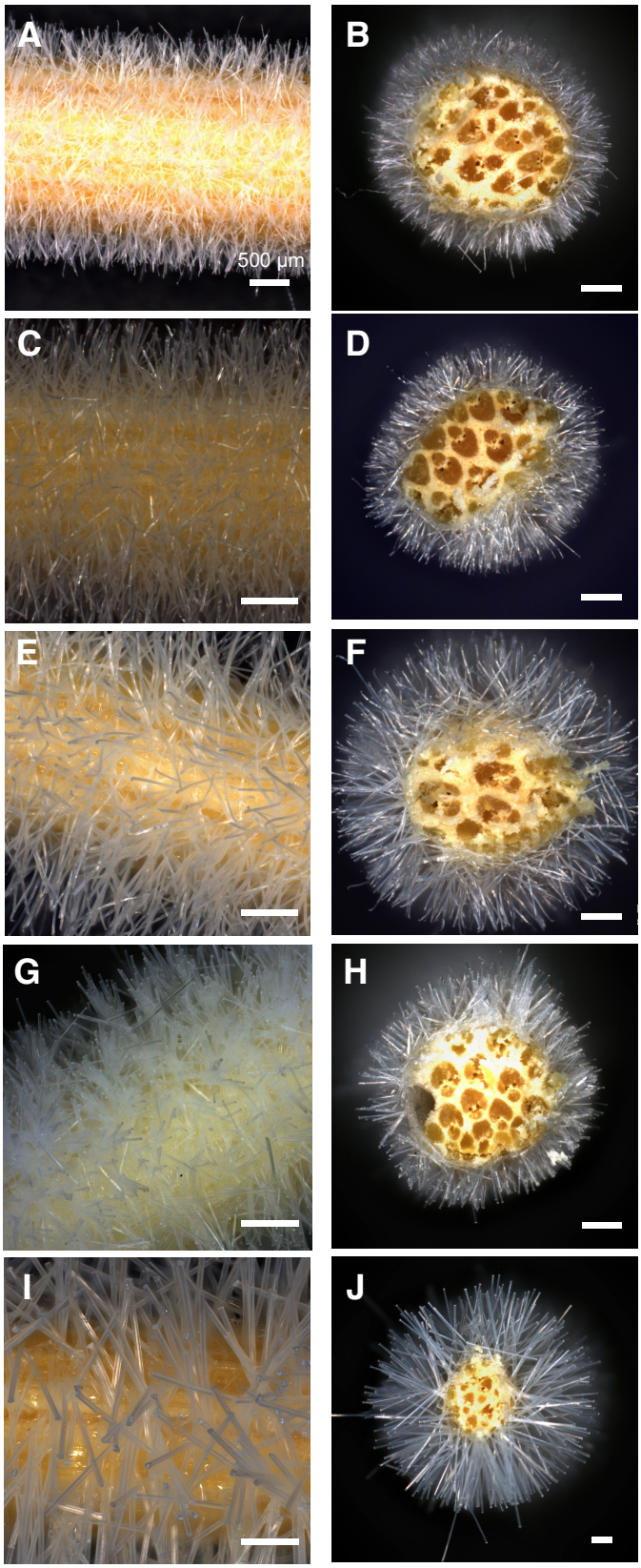

Figure 3.4.4: Overview of reference samples. (**A**, **C**, **E**, **G**, **I**) show top-view and (**B**, **D**, **F**, **H**, **J**) cross-section side view of V1, V2, V3, PA2, and PA3 respectively. The scale bars in (**B**-**J**) correspond to 500 µm.

A more detailed image of the morphology was obtained by high-resolution SEM (cf. Figure 3.4.5). The viscose flock fibers were clearly spatially separated from the PA flock fibers. Furthermore, as shown in Figure 3.4.5 C, the viscose flock fibers were partially immersed to the tip of the PA flock fiber by the adhesive film at the tip of the PA3 flock fibers.

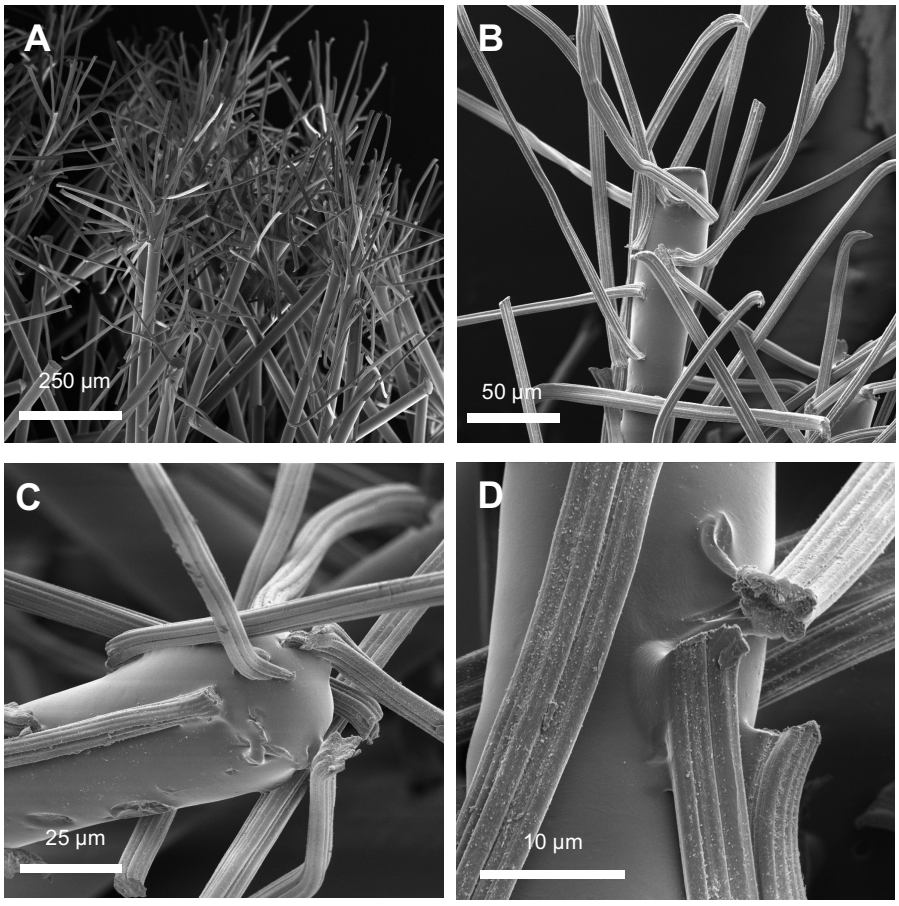

Figure 3.4.5: High-resolution scanning electron microscopy micrographs of PA3V2 sample. (**A**) shows the overview SEM micrograph of PAV2 sample while (**B-D**) focuses on a single Dandelion flock fiber.

To get a more comprehensive image of the chemical composition at the tip of the flock fiber, the PA3V2 sample was exemplary investigated by RAMAN-Imaging. As shown in Figure 3.4.6, a mixed phase at the tip, consisting of PA and adhesive, was determined, while the viscose flock fibers stand out from the PA and adhesive background, further confirming the mixed composition at the PA tip.

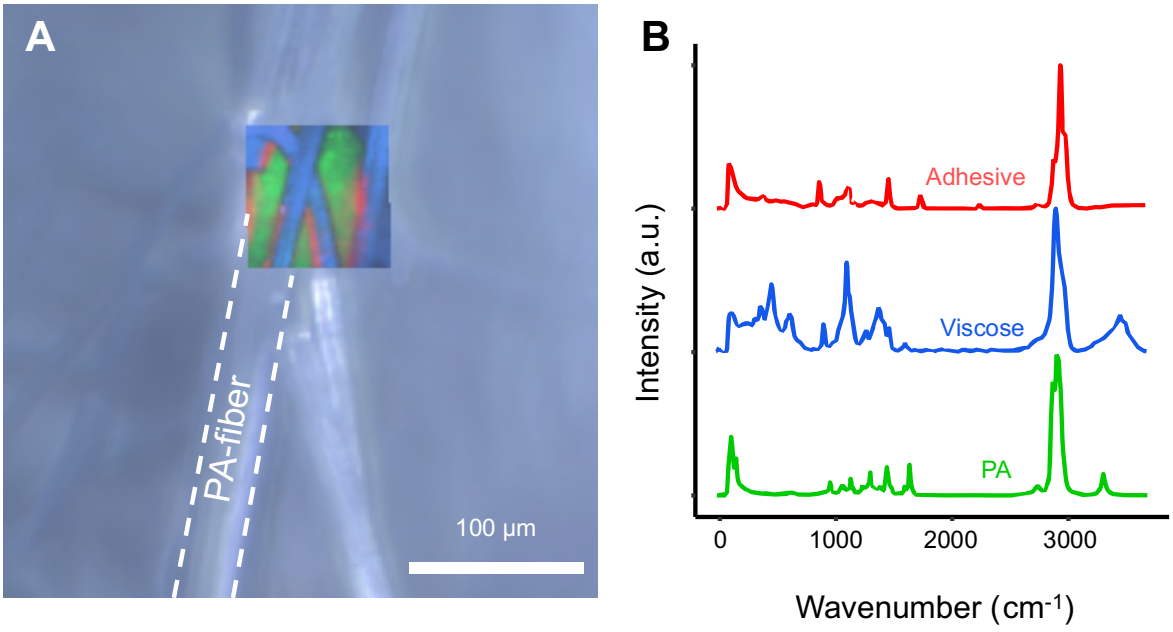

Figure 3.4.6: RAMAN Imaging of the Dandelion-inspired flock sample. The micrograph (**A**) shows the tip of the PA3 flock fiber. The scale bar corresponds to 100 µm. According to the RAMAN deconvolution (**B**), the tip consists of adhesive (red), viscose flock fibers (blue), and PA3 flock fibers (green).

It is worth mentioning that the described technique can also be applied to a flat two-dimensional substrate. However, such a two-dimensional flat substrate should be flexible to introduce a curvature during the adhesive droplet application. To illustrate this, a PET-mesh was wrapped around a 5 mL syringe and flocked according to the procedure shown in Figure 3.4.1. After the second flock was applied, the substrate was removed from the syringe and cured on a piece of aluminum foil. The resulting sample showed a similar morphology to the sample prepared on a cylindrical-shaped substrate (cf. Figure 3.4.7).

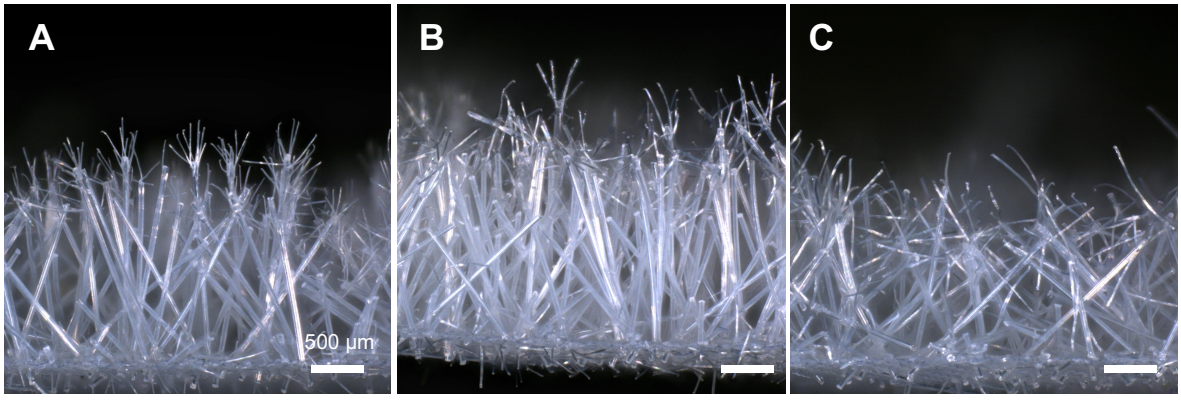

Figure 3.4.7: Optical microscopy micrographs of the Dandelion-inspired flocked samples on a flat 2D substrate. (**A-C**) show the cross-section of PAV1, PAV2, and PAV3 on a PET-mesh. The scale bar corresponds to 500 µm.

Water Transport

To first get an impression of the interaction of fog with a natural Dandelion seed, a seed was harvested and irrigated with fog under an optical microscope. A schematic overview of this process and the *in-situ* fog irrigation is depicted in Figure 3.4.8. It was observed that the pappus of the seed efficiently intercepted the fog particles. The intercepted fog particles formed spherical water droplets on the filament, indicating a hydrophobic contact angle (cf. Figure 3.4.8 A-C, Figure 3.4.8 D-G). This effect is reported in the literature and attributed to the microstructure of the filament (cf. Figure 3.4.8 H-J). [50–53] These droplets grew in size until they coalesced with other water droplets located on neighboring filaments. Due to surface tension and capillary effect, the filaments then collapsed. This process was repeated until the pappus was completely wetted and collapsed into a single structure.

The interaction of the natural Dandelion seed with fog relies on a coalescing filament mechanism. It is hypothesized that such a mechanism would result in an improved fog collecting yield. However, to adapt a coalescing filament interaction, flexible flock fibers with a low E-modulus are needed. Therefore, viscose flock fibers are utilized as an artificial pappus. To test this hypothesis, the PA3V2 sample was irrigated with fog and observed by optical microscopy. As already shown in Chapter 3.1, the fog condensation of PA and viscose flock fibers differs significantly. While the PA flock fiber captures single fog droplets, which are then agglomerated into larger droplets, the fog droplets captured by the viscose flock fibers immediately spread along the fiber. The difference in the collecting mechanism is attributed to the difference in the wettability of PA and viscose, respectively. The Dandelion seed-inspired flocked substrate showed a superposition of these two behaviors (Figure 3.4.9 C-E). First, the droplets were captured by the viscose flock (Figure 3.4.9 C), which led to an immediate spreading of the droplet. Afterward, the droplets were transported toward the intersection between the adhesive, PA-, and viscose flock fibers. Here, the droplets coalesced into larger droplets which were held in place at the intersection due to capillary forces exceeded by the branched morphology (Figure 3.4.9 D). The coalesced droplet grew until it was taken up by the flocked sample and transported further. An illustrative scheme of the collecting mechanism is shown in Figures 3.4.9 A and Figure 3.4.9 B.

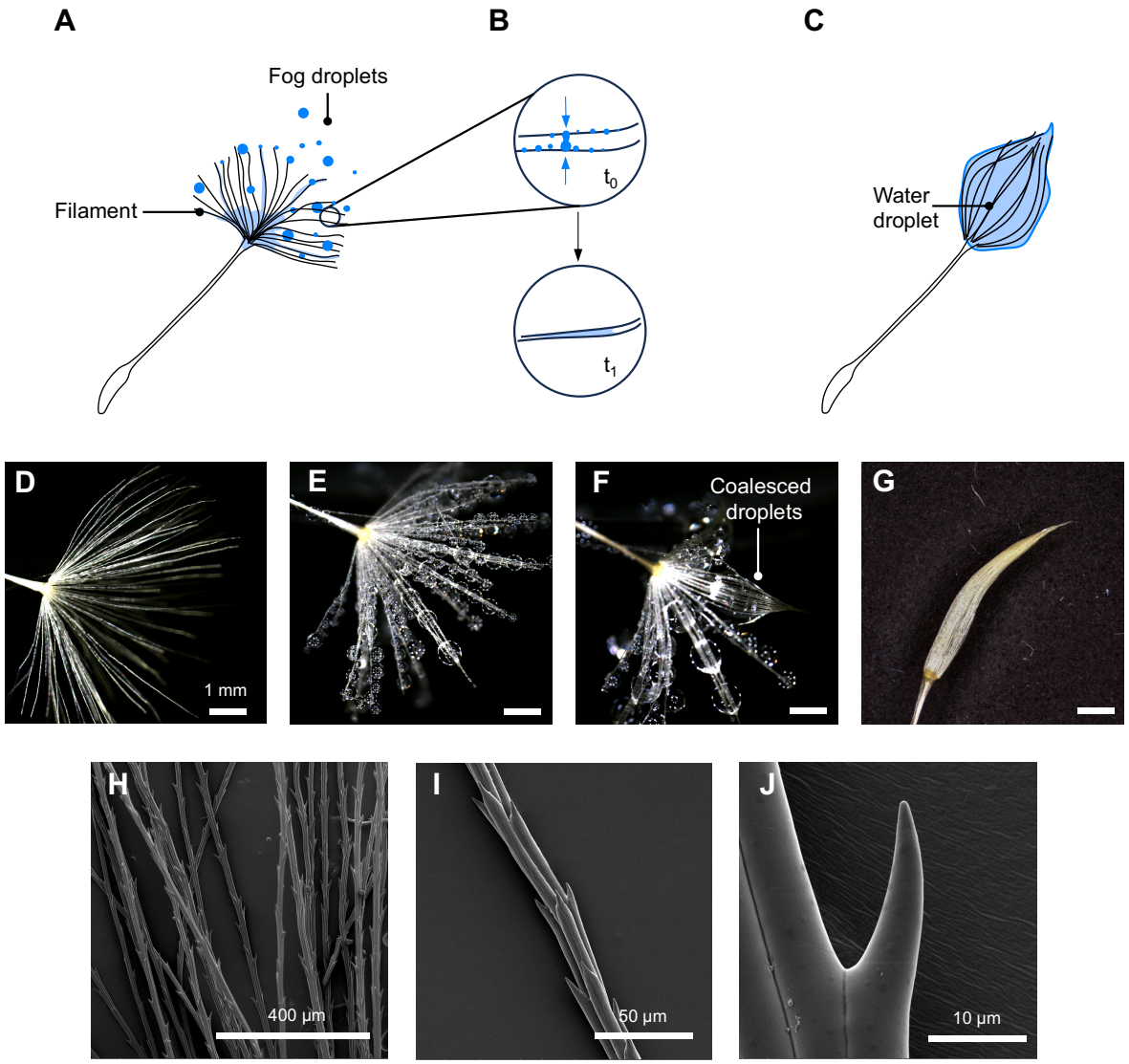

Figure 3.4.8: Interaction of fog with a Dandelion seed. (A-C) give schematic illustrations of the interaction of a Dandelion seed with fog. (**A**) shows the initial state when the Dandelion seed is irrigated with fog. (**B**) Once the fibrils are sufficiently wetted with fog, the water droplets grow until they coalesce with water droplets on neighboring filaments. (**C**) shows the state when the pappus is completely wetted and collapsed around a water droplet. (**D-G**) shows optical microscopy micrographs of a Dandelion seed irrigated at different irrigation states. (**H-J**) give SEM micrographs of the Dandelion seed filament. The scale bars in (**E-G**) correspond to 1 mm.

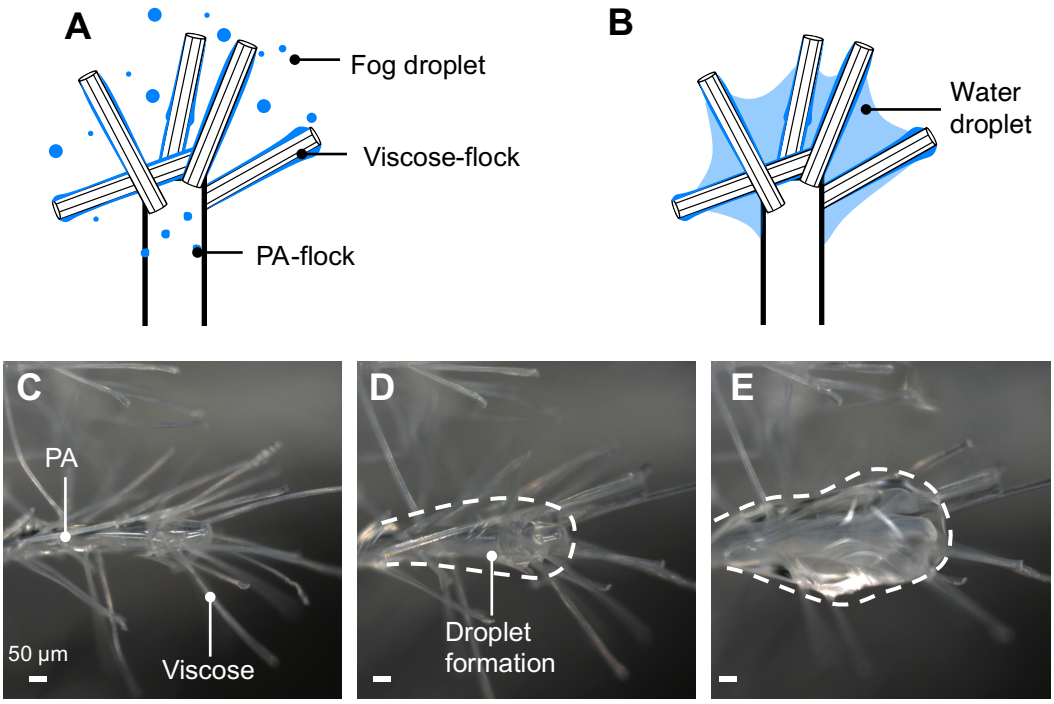

Figure 3.4.9: Schematical illustration and *in-situ* fog capture of a single Dandelion flock fiber (PA3V2). (**A**) and (**B**) illustrate schematically the fog-harvesting mechanism of the Dandelion flock. (**C**) Initial dry-state of a single PA3V2 flock fiber. (**D**) When fog droplets are intercepted by the viscose fiber, the fog droplets immediately spread and are transported toward the PA3-viscose intersection. (**E**) If sufficient fog particles are intercepted, a water droplet forms, which is held in place by capillary interaction. This droplet is then transported further either by gravity or by capillary interaction exceeded by the PA3-flock fibers. The white dashed line in (**D**, **E**) indicates the captured water droplet. The scale bars in (**D**, **E**) correspond to 50 µm.

Fog Harvesting of Dandelion-Inspired Flock Fibers

Numerous methods have been reported in the scientific literature for the purpose of condensing and capturing fog, each with distinct specific approaches. These approaches are generally based on a commercially available humidifier. [136] Such a commercially available humidifier is composed of an ultrasonic disc that generates fine fog particles (~ 1-10 µm). [137] These particles are then transported by a ventilator to the humidifier nozzle, where the sample is exposed for a certain time. By quantifying the condensed water and normalizing it to the time of the sample exposed in the fog stream as well as the sample area, the overall fog yield is determined. This general setup remains consistent in the literature. However, the specific experimental setups of each work vary significantly.

This variance leads to a wide range of parameters that influence the fog yield. Relevant parameters include sample distance, fog volume, surrounding humidity, fog velocity, and geometry of the fog stream, as well as many more. [136] While fog particle sizes and geometry of the fog stream seem to have a minor impact on the fog yield, sample distance and fog volume show a major positive correlation with the fog yield. [136] Due to inconsistent measurement parameters reported in the scientific literature, comparing the measured fog yields with values reported in the scientific literature is challenging. Therefore, this work omits a comparison to avoid contradictions. The values presented in this work are only compared with themselves to illustrate an overall trend. Furthermore, outdoor experiments were avoided due to the inconsistent and seasonable character of naturally occurring fog streams, which would make screening tests difficult to perform.

To test the fog yields, a setup was developed (cf. Figure 3.4.10). The sample table consisted of a Styrofoam plate, which was placed inside a transparent polypropylene (PP) box. Into the PP box, one inlet for the fog generator and four smaller outlets to prevent overpressure were cut. The sample itself was fixed with a sponge inside a microtube and placed on the sample stage. To ensure significant data points, the samples were irrigated continuously in the homemade setup for 3 h, where a measurement was taken every 45 min.

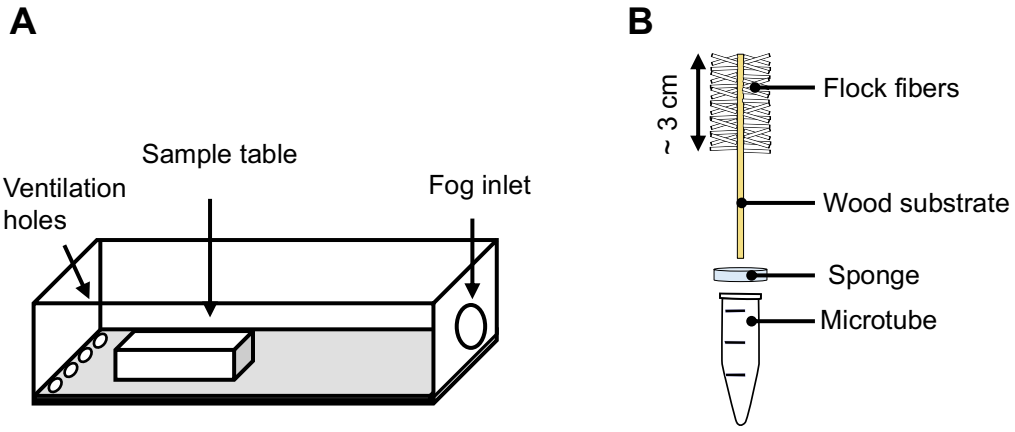

Figure 3.4.10: Schematic setup of the fog harvesting container. (**A**) Overview of the fog harvesting container. (**B**) shows the sample holder and collector setup.

The resulting water collecting (WC) values were calculated by dividing the mass difference by the projected mantle surface area of the sample:

$$WC = \frac{(m_t - m_0)}{2\pi r \cdot l}$$

(3.4.1)

Where m_t and m_0 correspond to the observed mass at a specific time *t*, and the initial sample mass. The radius of the substrate is *r*, which is fixed at 2 mm. The length of the substrate exposed to the fog is given by *l*.

To improve comparability between the different sample runs, a collecting ratio was defined. The ratio is calculated by dividing the water-collecting rate of the specific sample (WCR_S) by the water-collecting rate of the blank sample (WCR_B), which was obtained by linearly fitting the kinetic fog harvesting data as shown in Figure 3.4.11. The blank sample consisted of the substrate used for the preparation of Dandelion-inspired flock samples:

$$\mu = \frac{WCR_S}{WCR_B}$$

(3.4.2)

The collecting kinetics of the fog harvesting experiments are plotted in Figure 3.4.11 A. Here, two significant findings are drawn: First, *WC* followed a linear relationship. Fast *WC* and continuous drainage are relevant for designing an efficient fog harvesting system. If the flocked substrate is saturated with fog, a continuous flow of the water is suppressed. Therefore, an issue regarding water drainage would presumably have led to an attenuated *WC* during the experiment and, thus, to an overall diminished collecting efficiency. However, since a linear *WC*-time relationship for all samples was observed, sufficient drainage over 3 h is assumed. Second, conventional PA and viscose flocked samples showed already improved *WC* compared to the blank sample. The improved *WC* can be visualized by defining the collecting ratios μ, as shown in Equation 3.4.2. The corresponding μ values are plotted in Figure 3.4.11 B. While the collecting ratio for PA3 was determined to be 1.9(2), the viscose flocked substrate showed a collecting ratio of 1.4(1), 1.1(1), and 1.8(1) for V1, V2, and V3 respectively. Differences in collecting ratios can be generally attributed to surface area and specific wettability. As discussed in Chapter 3.1, viscose flock fibers have a hydrophilic and PA a more hydrophobic surface.

In general, a hydrophobic surface, compared to a hydrophilic surface, increases fog harvesting yields. [138] These results are in line with this trend. The hydrophilic viscose flocked substrate showed a lower collecting ratio than the hydrophobic PA. This relationship was also confirmed by comparing a PA2-flocked substrate sample with a V2 flocked substrate (μ(PA2) = 1.50(4)). The increased collecting ratio of V1 compared to V2 was presumably attributed to the increased surface area of V1 compared to V2. The significant increase from V1 to V3 is associated with the increased fiber length, which may facilitate fog droplet interception. The generally faster water transport of the viscose flocked substrate combined with the faster droplet growth of the PA flocked substrate synergized for the fog interaction of the Dandelion seed-inspired flocked samples. The coalescing fog interaction mechanism, as discussed in the previous chapter, translated to improved fog-collecting abilities. The samples with the Dandelion-inspired flock fibers showed collecting ratios of 2.1(2), 2.2(2), and 2.5(2) for PA3V1, PA3V2, and PA3V3, respectively. Comparing PA3V1 with PA3V2 suggests that the diameter of the viscose flock plays a diminishing role, while an increase in fiber length drastically improves the fog collection. The increased fiber length of PA3V3 goes hand in hand with increased pore size. The larger pore size of PA3V3 compared to PA3V2 and PA3V1 leads to a more accessible surface as well as a more efficient fog interception. It is suggested that these two effects led to an overall improvement in the collecting ratio. A summary of all relevant fitting parameters and values is listed in Table 3.4.1.

To conclude, Dandelion seed-inspired flock fibers on a cylindrical substrate were fabricated by utilizing a sequential flocking approach. Furthermore, the interaction between fog and the Dandelion-inspired structure was investigated in detail. The mechanism of fog collection was shown to rely on a coalescing interaction similar to that of the natural Dandelion seed. Furthermore, fog-collecting experiments were performed, and the collected water was quantified. The fog experiments revealed that the Dandelion seed-inspired flocked samples showed improved fog yields compared to a blank sample.

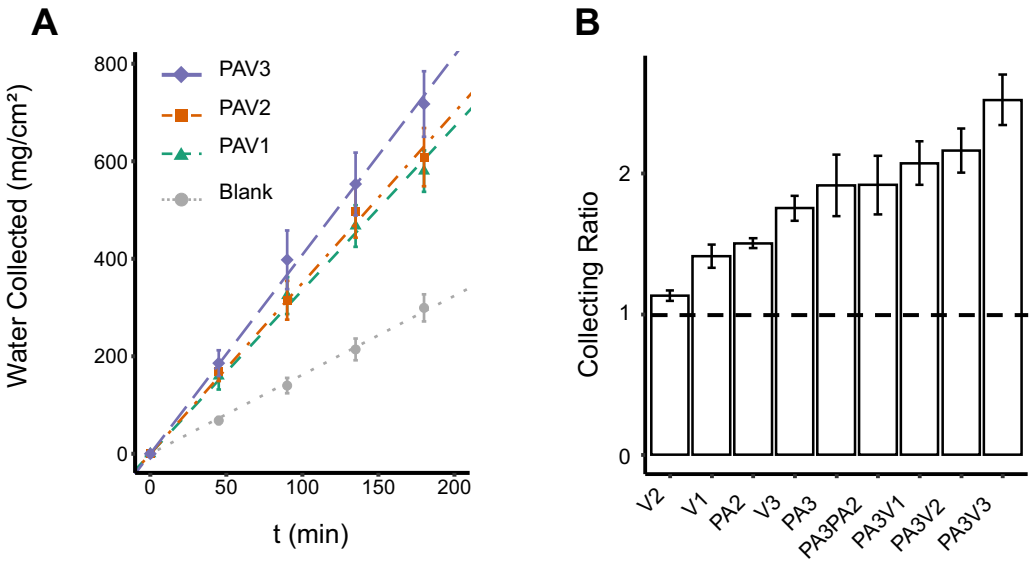

Figure 3.4.11: Fog harvesting performance of the Dandelion seed inspired flocked substrates. (**A**) shows the fog collecting kinetics and (**B**) the collecting ratio.

Table 3.4.1: Fitting parameters obtained from the linear fit of the kinetic fog harvesting data (Figure 3a). The values in the brackets give the standard error obtained by the fit. The first column corresponds to the sample ID, the second to the fitted Water Collection (*WC*), and the third to the adjusted R^2-value of the fit.

Sample ID	Water Collected ($mg/cm^2/min$)	Adjusted R^2 (%)
Blank	1.6(1)	99.89
V1	2.3(1)	99.85
V2	1.8(1)	99.85
V3	2.8(1)	99.85
PA2	2.4(1)	99.96
PA3	3.1(2)	99.32
PA3V1	3.4(1)	99.75
PA3V2	3.5(1)	99.79
PA3PA2	3.1(2)	99.39
PA3V3	4.1(1)	99.84

4. Conclusion

The thesis explored the interaction of electrostatically flocked substrates with fog toward the development of a fog-harvesting device. Thus, the study focused on bioinspired and biomimetic concepts due to the improved fog interaction. However, the complex hierarchical morphologies of biological systems are generally challenging to implement. As a secondary objective, the research aimed to showcase the potential of electrostatic flocking as a promising coating technique through the application of biomimetic and bioinspired concepts.

These objectives were achieved by first employing a preliminary study. The preliminary study was concluded in three major points: First, water transport parallel to the substrate was investigated. Here, the transport kinetics seemed to follow the WASHBURN law. Furthermore, it was shown that water is retained due to the unique morphology of the flock. Hereby, the amount of water retained in the flocked structure scaled with the pore size. Second, the different flock fibers used in the experiments (PA and viscose) showed complementary interactions with condensed water. The *in-situ* condensation experiments revealed that water tended to condense as droplets on the PA flock fibers. On the other hand, water condensing on the viscose flock fibers did wet along the flock fiber axis due to the increased hydrophilicity and grooved surface structure. Similar behavior was observed with the interaction of the flocked substrate with fog. When the PA flocked substrate interacted with fog, water droplets agglomerated into larger droplets, which were predominantly formed at the tip of the flock fiber. Similar to the direct condensation of water, viscose flocked substrate captured fog and spread droplets to a water film along the fiber axis. Third, the pore size and, therefore, the fiber dimensions influenced the interaction with fog. For flocked substrates with small pore sizes, fog mainly condensed on the flock fiber tip, while for larger pore sizes, more of the flock fiber surface was exposed to the fog stream.

Derived from the preliminary study, three bioinspired and biomimetic concepts based on the Namib desert beetle, cacti spines, and Dandelion seeds were developed and implemented. The first concept was inspired by the Namib desert beetle. The beetle specifically evolved to efficiently collect naturally occurring fog streams by a patterned backplate consisting of hydrophilic spots with a hydrophobic background. This morphology was adapted by selectively applying hydrophilic viscose flock fibers by a simple stamping technique. While the bioinspired fog interaction mechanism was successfully implemented in the structure, the morphology may be optimized in several ways.

Due to the spatial resolution limit of the FDM 3D printing process, adhesive spots with rather large cross-sectional diameters were applied. Different stamp fabrication methods may be used to obtain more control over the spatial resolution of the adhesive application process, or a different application method may be developed.

The second concept was inspired by the cactus spine, which is well known for collecting and unidirectionally transporting fog and water droplets. Such a hierarchical and anisotropic structure is challenging to implement, especially on a larger scale. However, utilizing a protocol based on the molecular self-assembly of *i*Pr-BTA in a flocked substrate revealed supramolecular spines. The spines were obtained by a simple immersion process, which may be readily implemented on larger scales. Notably, the supramolecular spine exhibited both structural and functional similarities to natural cacti spines while exceeding fog droplet transport velocities compared to natural cacti spines. Besides fog capture, the unique properties and structure of the supramolecular spine may be used for diverse applications, such as thermal insulation or coalescence filtration. However, before implementing these structures in industrial applications, the brittle mechanical properties of the *i*Pr-BTA must be addressed. Besides water transport applications, the project highlighted the potential of flocked substrates as structure-directing agents for materials beyond the investigated BTA systems.

The final device was inspired by the Dandelion seed. While the interaction of Dandelion seeds with water is well described in the literature, the adaptation of artificial Dandelion seeds toward a fog harvesting device is, to the author's best knowledge, not yet reported. In general, the fog capture mechanism of the Dandelion seed may be compared to that of the Namib Desert Beetle, where the pappus of the Dandelion seed leads to the coalescence of larger water droplets. Utilizing only electrostatic flocking in a sequential approach led to a morphology similar to a Dandelion seed. The simple approach and reliance on commercially available materials may facilitate industrial adaptation. The *in-situ* fog experiments revealed that the artificial Dandelion seed showed a similar fog-collecting mechanism to the biological role model. Finally, fog yields were determined, further confirming the improved water-collecting ability of the artificial Dandelion morphology.

The high flexibility and industrial establishment of electrostatic flocking technique may facilitate the adaption of the proposed fog capturing devices. However, while the interaction with water and fog were investigated, long term exposure, as well as biological safety issues has to be addressed in future work. The proposed structures may also be used for different applications besides fog harvesting like filtration-, thermal insulation, or tissue engineering applications.

5. Experimental Part

All chemicals were used as received unless noted otherwise. 2-Propanol (100 %, VWR) and ultrapure water (18.2 mΩ, < 2 ppb) were used in the experiments. Ethanol and acetone were distilled prior to use. Commercially available PA, viscose flock fibers, and adhesives (D535, D490, Tubicoll 1510A, L5515) were purchased from Borchert+moller. An overview of the available flock fibers, their lengths, and diameters, as well as the abbreviations used in this work, are given in Table 5.1.

Electrostatic flocking experiments were performed with a semiautomatic flocking device by Borchert+Moller (RF500) as well as with a smaller BT setup by Scenics (Pro Grass Box). A photograph of both setups is shown in Figure 5.1. The TB setup consisted of (1) a sample carousel, (2) a sample table, (3) a controller, (4) a high voltage connection, and (5) the flock fiber reservoir (cf. Figure 5.1 A). The sample carousel was connected to the ground and rotated underneath the flock fiber reservoir. The voltage and flock fiber feed were adjusted with the controller. After application of the flock fibers, the samples were removed from the carousel and cured in a convection oven (HTMA 6/220_3508 by Cabolite Gero). Excess flock fibers were collected by the sample table, which was fed back to the fiber reservoir after flock fiber application. While the TB setup was applicable for larger samples and higher sample throughput, testing different flock fibers is labor intensive since excessive cleaning steps would have been necessary to minimize contamination of different flock fibers. Therefore, for more rapid prototyping, a smaller BT setup was used (cf. Figure 5.1 B). The TB flocking device was utilized for the fabrication of flocked samples, as presented in Chapter 3, while the BT flocking device was employed for the preparations of the flocked substrates in the remaining Chapters. Specific preparation protocols of the sample preparation are given in the following Chapters.

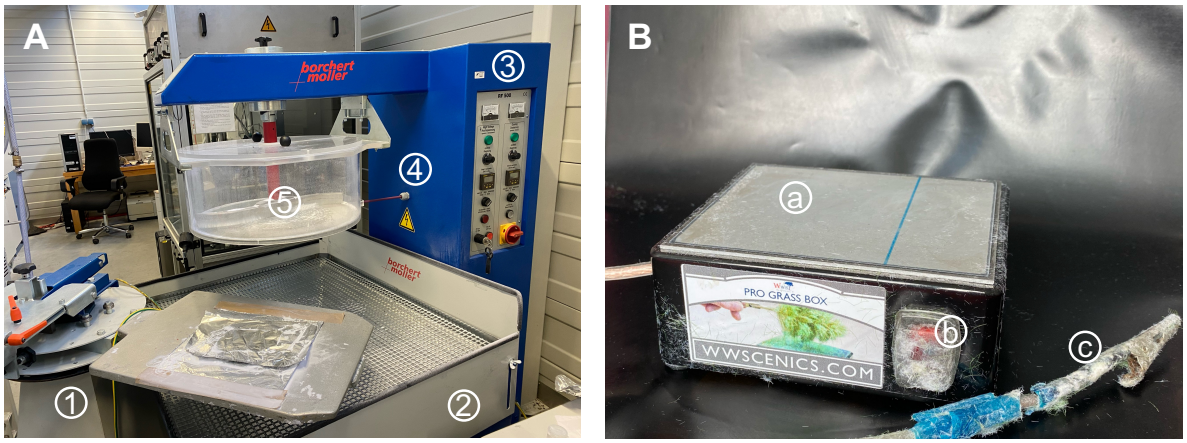

Figure 5.1: Electrostatic flocking devices. (**A**) shows semiautomatic TB setup by Borchert+Moller (RF 500). 1) corresponds to the sample carousel, 2) to the flock table, 3) to the console, 4) to the high voltage connection, and 5) to the flock fiber reservoir. (**B**) shows the BT setup by Scenic (Pro Grass Box). a) is the flock fiber reservoir and electrode, b) the power switch, and c) the ground cable.

Table 5.1 summarizes the flock fibers and adhesives used to prepare flocked samples in the specific chapters. In the preliminary experiments, all available flock fibers and adhesives were used for the sample preparations but were later limited to the listed ones.

Table 5.1.: Overview of materials used in the sample fabrication. The table lists the flock fibers, adhesive and substrates used in the respective chapters.

Chapter No.	Flock fibers	Adhesive	Substrate
1	PA2, PA2-1 PA3, PA4, V1, V2, V3	D490	Glass slide, Al-foil
2	V2, PA2, V3	D535	P(VDF-co-HFP)
3	PA2, PA3, PA4	Tubicoll 1510A, L5515	PET-Mesh
4	PA2, PA3, V1, V2, V3	D490	Wood sticks

Interaction of Flocked Substrates with Water

Preparation of the Flocked Samples

The adhesive was applied to a glass slide with a mask, and the different viscose and PA flock fibers were applied to Al-foil and cured at 90 °C for 30 min. Afterward, the samples were cleaned with water and pressured air and attached to a glass slide.

Investigation of the Wicking Properties

The flocked glass slides were placed vertically into a beaker filled with a methylene blue solution. A video was recorded while the flock was filled with the liquid. A calibration was placed next to the glass slides to evaluate the capillary rise.

In-situ Fog and Dew-Condensations Experiments

The *in-situ* dew-condensation experiments were investigated by optical microscopy. The setup consists of a 3D-printed cooling stage, a holder for an Arduino Uno (Arduino Foundation), and a breadboard. The cooling stage includes a copper cooling sink, a PELTIER element as the active cooling device and specimen table, and a petri dish as a top cover. Inside the cooling stage, a thermistor probe (NTC 10K by Funduino) was adhered with thermal paste onto the specimen stage. The temperature and humidity inside the chamber were tracked with a combi-sensor (DHT22 by Joy-IT). The values were recorded by an Arduino and displayed at the front of the setup by an OLED display. Using the following equation, the dewpoint was estimated by the Magnus formula as proposed by Mark G. Lawrence: [113]

$$T_{Dew} = \frac{B_1 \left[\ln\left(\frac{RH}{100}\right) + \frac{A_1 T}{B_1 + T}\right]}{A_1 - \ln\left(\frac{RH}{100}\right) - \frac{A_1 T}{B_1 + T}} \tag{5.1}$$

T_{Dew} corresponds to the dewpoint, T to the dry bulb temperature, RH to the relative humidity and A_1 = 17.625, B_1 = 243.04 °C to fitting coefficients. [113]

A PETRIE dish was placed on top of the setup, which was modified with a glass slide to ensure a non-distorted view into the chamber. The Peltier element was controlled by an external power supply. Varying the voltage and current limit, different cooling powers were realized. In general, an applied voltage between 2.0 V and 5.0 V at 1.2 A was sufficient to cool the sample to the dewpoint.

Namib Desert Beetle-Inspired Membrane

Electrospinning of P(VDF-*co*-HFP)

Random-oriented P(VDF-*co*-HFP) nanofiber nonwovens were obtained by electrospinning. The polymer was dissolved (16 wt./v. %) at 50 °C in a DMF-acetone (6/4 v./v.) mixture 3 h prior to spinning.

The nonwoven was spun at a voltage of 15 kV, a mass flow of 0.6 mL / h, a temperature of 20.0 °C, and a relative humidity of 50 % onto a piece of aluminum foil. After spinning, the nonwoven was washed to remove residual solvent and dried at room temperature for 72 h.

Fabrication of a 3D printed stamp

To selectively apply the adhesive to the nonwoven, a 3D-printed stamp was designed with Blender3D. The model was exported and sliced with PrusaSlicer, using the 0.2 mm quality preset. After slicing, the model was printed with a Prusa Mini+ (Prusa, 0.4 mm nozzle). The stamp was 3D-printed with PLA by PolyTerra.

Fabrication of Namib Desert Beetle inspired Membrane

An adhesive film was applied to a glass slide. The 3D-printed stamp was pressed slightly into the adhesive film. Immediately afterwards, the stamp was pressed to the previously fabricated nonwoven. After a few seconds, the stamp was peeled off the nonwoven, the ground was attached to the nonwoven and a voltage was applied between the nonwoven and the flock fibers. The ground from the flocked nonwoven was removed and excess flock fibers were carefully dusted down. The sample was allowed to dried for 72 h. Finally, the flocked nonwoven was cleaned with pressured air, deionized water and then dried before investigating the fog condensation.

Supramolecular Cacti Spines

Preparation of the Flocked Substrates

Adhesive and hardener were thoroughly mixed in 1:1 wt.-ratio for about 15 min. After 5 min of settling, the PET-meshes (Eckert GmbH, 100 µm pore, and thread size) were dip-coated with a thin adhesive layer and transferred to a paper towel. The excessive adhesive was removed by squeegeeing with a glass rod. The adhesive-coated coated PET-mesh was fixed on an aluminum foil as an electrode and placed below the flocking chamber (RF 500, Borchert+Moller). An electric field of 2.3 kV/cm was applied for 60 s. After a 10 s delay, the flock feed was switched on for 30 s. Finally, the PET-mesh with the vertically deposited PA (3.3 dtex/0.5 mm, *reinweiß*) microfibers was placed onto a steel trail and transferred into a convection oven to crosslink the adhesive at 120 °C for 20 min. Afterward, the flock was stored for 24 h at room temperature to complete the adhesive curing. The samples were cleaned with pressured air to remove loose microfibers and subsequently washed with H_2O (3x50 mL), ethanol (3x50 mL), 2-propanol (3x50 mL), acetone (2x30 mL) and dried in vacuum at 50 °C for 12 h.

Synthesis of *N*^{1},*N*^{3},*N*^{5}-tri[2-(diisopropylamino)-ethyl]-1,3,5-benzenetricarboxamide (*iPr*-BTA)

N^1,*N*^{3},*N*^{5}-tri[2-(diisopropylamino)-ethyl]-1,3,5-benzenetricarboxamide was synthesized as described elsewhere. [125,126] Briefly, the synthesis of *i*Pr-BTA was performed in two steps. In the first step trimesic acid (**1**, 0.476 mol, 100 g) was dissolved in 1.5 L of methanol (MeOH). To the solution, 7 mL of concentrated sulfuric acid (H_2SO_4) were added and the mixture was refluxed for two days. After cooling, the precipate was filtered and washed with a few milliliters of MeOH. After drying, trimesic acid trimethyl ester (**2**, 0.465 mol, 108.0 g, 90 %) was obtained as a white powder.

Yield: 108.0°g (90 %) of a white powder. ^{1}H-NMR (300 MHz, $CDCl_3$, δ): 3.99 (s, 9H), 8.85 (s, 3H). ^{13}C-NMR (75 MHz, $CDCl_3$, δ): 20.9, 38.5, 42.8, 47.8, 127.8, 135.3, 165.2 ppm.

In the second step, trimesic acid trimethyl ester (**2**, 28 mmol, 7.17 g) were dispersed in *N*,*N*-diisopropylethylenediamine (142 mmol, 25 mL) under constant argon atmosphere. The mixture was heated to 125 °C and stirred for 17 h. After cooling to r.t., the mixture was twice boiled in 400 mL of ethyl acetate and subsequently filtered. After filtering and drying, *i*Pr-BTA (**3**, 12.2 g, 72 %) was obtained as a white powder.

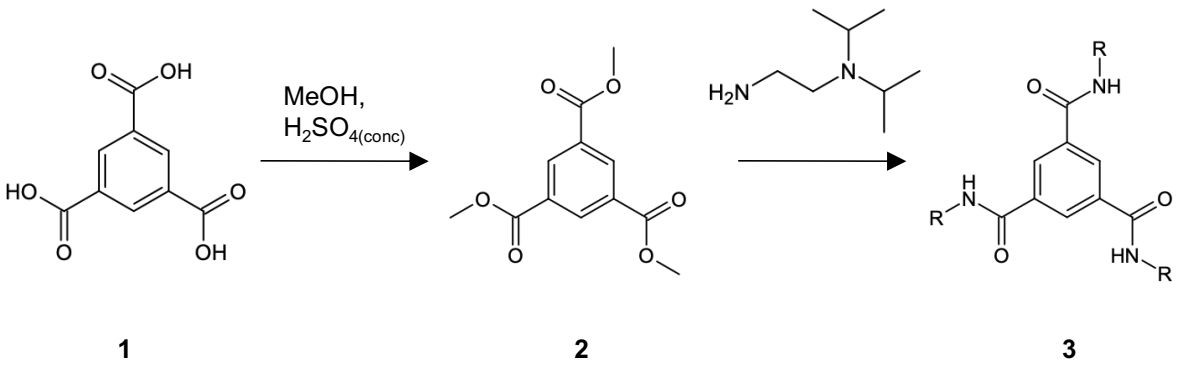

Scheme 5.1.: Synthesis of *i*Pr-BTA. First, an esterification of trimesic acid to trimesic acid trimethyl ester. In the second step, trimesic acid trimethyl ester was reacted with *N,N*-diisopropylethylenediamine to *i*Pr-BTA.

Yield: 12.2°g (72%) of a white powder. ^{1}H-NMR (300 MHz, $CDCl_3$, δ): 1.06 (d, 36H), 2.71 (t, 6H), 3.07 (m, 6H), 3.45 (quartett, 6H), 7.23 (t(br), 3H), 8.41 (s, 3H) ppm. ^{13}C-NMR (75 MHz, $CDCl_3$, δ): 20.9, 38.5, 42.8, 47.8, 127.8, 135.3, 165.2 ppm.

Evaporation-Induced Self-Assembly of BTA from Solution

A clear solution containing 0.50 wt.% of the BTA in 2-propanol was prepared. 5 µL of this solution was dropped on a Si-wafer and the solvent was evaporated at ambient conditions.

Preparation of Supramolecular Spines

The PA flocked substrate was immersed with a *i*Pr-BTA solution of 0.50 wt.% in 2-propanol for 30 seconds and placed for 10 seconds on a filtration paper to partially remove the *i*Pr-BTA solution. The specimen was then placed in a petri dish, covered with aluminum foil, and stored at 30 °C to complete solvent evaporation.

Flocked Samples with a Dandelion-Seed Morphology

Preparation of Conventional Flocked Samples

Fog harvesting samples were prepared by the electrostatic flocking technique. First, a thin adhesive coating (D535) was applied to a cylindrical wooden substrate (d = 2 mm, Fackelmann) with a brush. Afterward, an electrostatic potential is applied between the adhesive layer and the flock fibers for ~ 30 s. After sufficiently covering the samples with flock fibers, the samples were cured at 120 °C for 30 min, followed by ~ 12 h at room temperature. To remove any loose flock fibers, the samples were cleaned with pressured air.

Preparation of Flocked Samples with a Dandelion-Seed Morphology

PA3 flock fibers were applied to a wooden stick and cured as described above. Subsequently, a thin adhesive layer was applied onto a glass slide (~0.02 mL/cm²). The PA flock was then rolled into the thin adhesive layer to modify the flock fiber tips with adhesive droplets. Afterward, an electrostatic potential is applied between the viscose and the PA flock fibers. The sample is again cured at 120 °C for 30 min and 12 h at room temperature. Finally, the sample was again cleaned with pressured air.

Investigation of Fog Harvesting Performance

Inspired by the setup of S. Knapczyk-Korczak *et al*., [139,140] a modified fog harvesting setup was designed. A commercial fog humidifier (Beuer LB88) was used as a fog generator. The fog speed at the outlet was determined to be ~ 0.5 m/s, and the mean particle size was between 3.0-5.0 µm. The fog generator was attached to a polypropylene (12 cm*24.5 cm*31.5 cm, h*b*l) container with a 3D printed connector (d = 5 cm). To prevent overpressure in the chamber, four ventilation holes were drilled (d = 0.8 cm) at the rear edge of the container. After the setup was warmed up for 1 h, the three samples were placed at a distance of 15 cm from the fog inlet and irrigated for 3 h, while every 45 min, the weight difference was measured. Water that condensed at the outside of the microtube was removed, and the weight of the microtube was recorded. Afterward, the sample was placed back in the fog chamber and continued irrigated for 180 min.

Characterization

Scanning Electron Microscopy

Prior to the recordings of electron microscopy micrographs, the samples were sputtered (Cressington 208HR with planetary stage and QCM crystal) with 2 nm of Pt metal. The samples were investigated with FEI Quanta FEG 250 (ThermoFisher) using an Everhardt Thornley detector (ETD) at a high vacuum (2 10^{-3} Pa), an acceleration voltage of between 1 kV-8 kV, a spot size of 3, and a working distance between 8 mm and 12 mm.

Environmental Scanning Electron Microscopy

The water condensation behavior and wettability of non-sputtered supramolecular spines and neat PA microfibers were investigated by the environmental scanning electron microscope (ESEM) FEI Quanta FEG 250 (Thermo Fisher Scientific) equipped with a Peltier cooling stage (ThermoFisher) and a gaseous secondary electron detector (GSED).

ESEM images were recorded with an acceleration voltage of 10 kV. Measurements were carried out at constant water pressure of 720 Pa and upon cooling the sample from 3.9 °C to 1.9 °C (at a rate of 1 °C min^{-1}).

Optical Light Microscopy

Samples and in-situ fog irrigation were investigated with a digital optical microscope (Smartzoom 5, Zeiss). The microscope was equipped with a 4.2-megapixel sensor and two different objectives (Zeiss PlanApo D 1.6x/0.1 FWD 36 mm, 36x-360x magnification, and Zeiss PlanApo D 5x/0.3 FWD 30mm, 101x-1010x magnification). The illumination was ensured by a coaxial brightfield and ring light.

RAMAN-Imaging

Raman imaging measurements were performed with *a* WITec alpha 300 RA+ imaging system equipped with a UHTS 300 spectrometer and a back-illuminated Andor Newton 970 EMCCD camera for confocal RAMAN imaging. The measurements were conducted at an excitation wavelength of $\lambda = 532$ nm, using a laser power of 30 mW and an integration time of 0.5 s. All spectra were subjected to a cosmic ray removal routine and baseline correction. Imaging maps were determined by measuring the components separately under the same conditions.

Nuclear Magnetic Resonance Spectroscopy (NMR)

^{1}H-NMR (300MHz) and ^{13}C-NMR (75 MHz) spectra were recorded on a Bruker Avance AC 300 spectrometer at room temperature.

Software

For the data evaluation, ImageJ [141] and R [142–144] were utilized. The models were created with Blender 3D (BlenderFoundation, Version 3.6.4) and sliced with the quality preset with PrusaSlicer (Prusa, Version: 2.6.1).

Grammar and orthography of the thesis were checked with Grammarly (Version 1.50.1.1) before submission.

References

1. Gautieri, A., Vesentini, S., Redealli A., Buehler, M. J. Hierarchical Structure and Nanomechanics of Collagen Microfibrils from the Atomistic Scale Up. *Nano Lett.* **11**, 757–766 (2011).
2. Nazzi, F. The hexagonal shape of the honeycomb cells depends on the construction behavior of bees. *Sci Rep* **6**, 28341 (2016).
3. Bai, F., Wu, J., Gong, G., Guo, L. Biomimetic Cactus Spine with Hierarchical Groove Structure for Efficient Fog Collection. *Adv. Sci.* **2**, 1500047 (2015).
4. Parker, A. R. & Lawrence, C. R. Water capture by a desert beetle. *Nature* **414**, 33–34 (2001).
5. Seale, M. *et al.* Dandelion pappus morphing is actuated by radially patterned material swelling. *Nat Commun* **13**, 2498 (2022).
6. Bhushan, B. Biomimetics: lessons from nature–an overview. *Philos Trans R Soc A* **367**, 1445–1486 (2009).
7. Liao, X. *et al.* High strength in combination with high toughness in robust and sustainable polymeric materials. *Science* **366**, 1376–1379 (2019).
8. Burgard, M. *et al.* Mesostructured Nonwovens with Penguin Downy Feather–Like Morphology—Top–Down Combined with Bottom–Up. *Adv Funct Materials* **29**, 1903166 (2019).
9. Zhang, L. Inkjet printing for direct micropatterning of a superhydrophobic surface: toward biomimetic fog harvesting surfaces. *J Mater Chem A* (2015).
10. Fratzl, P. Biomimetic materials research: what can we really learn from nature's structural materials? *J R Soc Interface* **4**, 637–642 (2007).
11. Wang, Y., Zhao, W., Han, M., Xu, J. & Tam, K. C. Biomimetic surface engineering for sustainable water harvesting systems. *Nature Water* **1**, 587–601 (2023).

12. Ward, D. *The Biology of Deserts*. (Oxford University Press, 2016).
13. Waterman, T. H. Evolutionary challenges of extreme environments (part 2). *J. Exp. Zool.* **291**, 130–168 (2001).
14. Rothschild, L. J., Mancinelli, R. L. Life in extreme environments. *Nature* **409**, 1092–1101 (2001).
15. Martorell, C. & Ezcurra, E. The narrow-leaf syndrome: a functional and evolutionary approach to the form of fog-harvesting rosette plants. *Oecologia* **151**, 561–573 (2007).
16. FAO. *The State of the World's Land and Water Resources for Food and Agriculture – Systems at Breaking Point (SOLAW 2021)*. (FAO, Rome, 2021).
17. World Economic Forum. *Global Risks 2015*. (2015).
18. Liu, J. *et al.* Water scarcity assessments in the past, present and future. *Earth's future* **5**, 545–559 (2017).
19. Meigs, P. *Geography of coastal deserts; Arid zone research*. (1966).
20. Abdul-Wahab, S. A., Al-Hinai, H., Al-Najar, K. A., Al-Kalbani, M. S. Fog Water Harvesting: Quality of Fog Water Collected for Domestic and Agricultural Use. *Environ. Eng. Sci.* **24**, 446–456 (2007).
21. Kaseke, K. F., Wang, L. Fog and Dew as Potable Water Resources: Maximizing Harvesting Potential and Water Quality Concerns. *GeoHealth* **2**, 327–332 (2018).
22. Wan, K., Gou, X. & Guo, Z. Bio-inspired Fog Harvesting Materials: Basic Research and Bionic Potential Applications. *J Bionic Eng* **18**, 501–533 (2021).
23. Yu, Z. *et al.* Fog Harvesting Devices Inspired from Single to Multiple Creatures: Current Progress and Future Perspective. *Adv Funct Materials* **32**, 2200359 (2022).
24. Kennedy, B. S. & Boreyko, J. B. Bio-Inspired Fog Harvesting Meshes: A Review. *Adv Funct Materials* 2306162 (2023).

25. Gurera, D., Bhushan, B. Designing bioinspired surfaces for water collection from fog. *Philos. Trans. Royal Soc. A* **377**, 20180269 (2019).

26. Butt, H.-J., Graf, K. & Kappl, M. *Physics and Chemistry of Interfaces*. (Wiley-VCH, Weinheim, 2003).

27. Wenzel, R. N. Resistance of Solid Surfaces to Wetting by Water. *Ind. Eng. Chem.* **28**, 988–994 (1936).

28. Cassie, A. B. D. & Baxter, S. Wettability of porous surfaces. *Trans. Faraday Soc.* **40**, 546 (1944).

29. Marmur, A. Wetting on Hydrophobic Rough Surfaces: To Be Heterogeneous or Not To Be? *Langmuir* **19**, 8343–8348 (2003).

30. Bormashenko, E. Progress in understanding wetting transitions on rough surfaces. *Adv Colloid Interface Sci* **222**, 92–103 (2015).

31. J. Ju, H. Bai, Y. Zheng, T. Zhao, R. Fang, L. Jiang. A multi-structural and multi-functional integrated fog collection system in cactus. *Nat. Commun.* **3**, 1247 (2012).

32. Chaudhury, M. K. & Whitesides, G. M. How to Make Water Run Uphill. *Science* **256**, 1539–1541 (1992).

33. Zheng, Y. *et al.* Directional water collection on wetted spider silk. *Nature* **463**, 640–643 (2010).

34. J. Ju, K. Xiao, X. Yao, H. Bai, L. Jiang. Bioinspired conical copper wire with gradient wettability for continuous and efficient fog collection. *Adv. Mater.* **25**, 5937–5942 (2013).

35. Li, X., Yang, Y., Liu, L., Luyang, Chen, Y., Chu, M., Sun, H., Shan, W., Chen, Y. 3D–Printed Cactus–Inspired Spine Structures for Highly Efficient Water Collection. *Adv. Mater. Interfaces* **7**, 1901752 (2020).

36. C. Luo. Theoretical Exploration of Barrel-Shaped Drops on Cactus Spines. *Langmuir* **31**, 11809–11813 (2015).

37. É. Lorenceau & D. Quéré. Drops on a conical wire. *J. Fluid Mech.* **510**, 29–45 (2004).

38. Guo, L., Kumar, S., Yang, M., Tang, G. & Liu, Z. Role of the microridges on cactus spines. *Nanoscale* **14**, 525–533 (2022).

39. Seely, M. K. & Hamilton, W. J. Fog catchment sand trenches constructed by tenebrionid beetles, lepidochora, from the namib desert. *Science* **193**, 484–486 (1976).

40. Zhu, H. Beetle-inspired wettable materials: from fabrications to applications. *Mater Today Nano* **6***,* 100034 (2019).

41. Khadka, K. & Ferguson, G. S. Does the Roll-off Angle Depend on Work of Adhesion? *Langmuir* **38**, 4820–4825 (2022).

42. Furmidge, C. G. L. Studies at phase interfaces. I. The sliding of liquid drops on solid surfaces and a theory for spray retention. *J Colloid Sci* **17**, 309–324 (1962).

43. Correia, D. M. *et al.* Surface wettability modification of poly(vinylidene fluoride) and copolymer films and membranes by plasma treatment. *Polymer* **169**, 138–147 (2019).

44. Yu, Z. Namib desert beetle inspired special patterned fabric with programmable and gradient wettability for efficient fog harvesting. *J Mater Sci* (2021).

45. Zhai, L., Berg, M. C., Rubner, M. F. & Cohen, R. E. Patterned Superhydrophobic Surfaces: Toward a Synthetic Mimic of the Namib Desert Beetle. *Nano Lett.* **6**, 1213–1217 (2006).

46. Black, C. C., Osmond C. B. Crassulacean acid metabolism photosynthesis: `working the night shift'. in *Discoveries in Photosynthesis* (Springer-Verlag, Heidelberg, 2005).

47. F. T. Malik, R. M. Clement, D. T. Gethin, M. Kiernan, T. Goral, P. Griffiths, D. Beynon, A. R. Parker. Hierarchical structures of cactus spines that aid in the directional movement of dew droplets. *Philos. Trans. Royal Soc. A* **374**, (2016).

48. Malik, F. T., Clement, R. M., Gethin, D. T., Beysens, D., Cohen, R. E., Krawszik, W., Parker, A. R. Dew harvesting efficiency of four species of cacti. *Bioinspir. Biomim.* **10**, 036005 (2015).

49. Yi, S., Wang, J., Chen, Z., Liu, B., Ren, L., Liang, L., Jiang, L. Cactus–Inspired Conical Spines with Oriented Microbarbs for Efficient Fog Harvesting. *Adv. Mater. Technol.* **4**, 1900727 (2019).

50. Stewart-Wade, S. M., Neumann, S., Collins, L. L. & Boland, G. J. The biology of Canadian weeds. *Taraxacum officinale* G. H. Weber ex Wiggers. *Can. J. Plant Sci.* **82**, 825–853 (2002).

51. Grauso, L., Emrick, S., De Falco, B., Lanzotti, V. & Bonanomi, G. Common dandelion: a review of its botanical, phytochemical and pharmacological profiles. *Phytochem Rev* **18**, 1115–1132 (2019).

52. Han, Y. L. *et al.* Collective Wetting of a Natural Fibrous System and Its Application in Pump-Free Droplet Transfer. *Adv Funct Materials* **27**, 1606607 (2017).

53. Hale, A. N. *et al.* Reduced Seed Germination after Pappus Removal in the North American Dandelion (*Taraxacum officinale* ; Asteraceae). *Weed sci.* **58**, 420–425 (2010).

54. Sørensen, P. A., Kiil, S., Dam-Johansen, K. & Weinell, C. E. Anticorrosive coatings: a review. *J Coat Technol Res* **6**, 135–176 (2009).

55. Montemor, M. F. Functional and smart coatings for corrosion protection: A review of recent advances. *Surf Coat Technol* **258**, 17–37 (2014).

56. Radhamani, A., Lau, H. C. & Ramakrishna, S. Nanocomposite coatings on steel for enhancing the corrosion resistance: A review. *J Compos Mater* **54**, 681–701 (2020).

57. Zhang, H. & Chiao, M. Anti-fouling Coatings of Poly(dimethylsiloxane) Devices for Biological and Biomedical Applications. *J. Med. Biol. Eng.* **35**, 143–155 (2015).

58. Pistone, A., Scolaro, C. & Visco, A. Mechanical Properties of Protective Coatings against Marine Fouling: A Review. *Polymers* **13**, 173 (2021).

59. Wang, F. *et al.* Review of the research on anti-protein fouling coatings materials. *Prog Org Coat* **147**, 105860 (2020).

60. Arshad, Momen, G., Farzaneh, M. & Nekahi, A. Properties and applications of superhydrophobic coatings in high voltage outdoor insulation: A review. *IEEE Trans. Dielect. Electr. Insul.* **24**, 3630–3646 (2017).

61. Wu, J., Li, X., Li, M., Li, Y. & Qiu, A. Review of effects of dielectric coatings on electrical exploding wires and *Z* pinches. *J. Phys. D: Appl. Phys.* **50**, 403002 (2017).

62. Zhu, M., Xue, J., Wei, Y., Li, G. & Zhang, G. Review of interface tailoring techniques and applications to improve insulation performance. *High Voltage* **7**, 12–31 (2022).

63. Goldschmidt, A., Streitberger, H.-J. *BASF Handbook on Basics of Coating Technology*. (Vincentz Network, Hannover, 2014).

64. Gooch, J. W. *Lead-Based Paint Handbook*. (Springer International Publishing, Cham, 2002).

65. Kumpugdee-Vollrath, M., Kruase, J.-P. *Easy Coating: Grundlagen Und Trends Beim Coating Pharmazeutischer Produkte*. (Vieweg + Teubner in GWV Fachverlage GmbH, Wiesbaden, 2011).

66. Nazarpour, S. *Thin Films and Coatings in Biology*. (Springer Netherlands, Dordrecht, 2013).

67. Ichou, H., Arrousse, N., Berdimurodov, E. & Aliev, N. Exploring the Advancements in Physical Vapor Deposition Coating: A Review. *J Bio Tribo Corros* **10**, 3 (2024).

68. Lobe, S., Bauer, A., Uhlenbruck, S. & Fattakhova-Rohlfing, D. Physical Vapor Deposition in Solid-State Battery Development: From Materials to Devices. *Adv Sci* **8**, 2002044 (2021).

69. Hampden-Smith, M. J. & Kodas, T. T. Chemical vapor deposition of metals: Part 1. An overview of CVD processes. *Chem Vap Depos* **1**, 8–23 (1995).

70. Dobkin, D. M. & Zuraw, M. K. *Principles of Chemical Vapor Deposition*. (Springer Netherlands, Dordrecht, 2003).

71. Schneller, T. *Chemical Solution Deposition of Functional Oxide Thin Films*. (Springer Vienna, Vienna, 2013).

72. Tilney, R. Electrostatic coating processes. *Br. J. Appl. Phys.* **4**, S51–S54 (1953).

73. Ayrilmis, N. A review on electrostatic powder coatings for the furniture industry. *Int J Adhes Adhes* **113**, 103062 (2022).

74. Pietschmann, J. *Industrielle Pulverbeschichtung: Grundlagen, Verfahren, Praxiseinsatz*. (Springer Fachmedien Wiesbaden, Wiesbaden, 2023).

75. Giessmann, A. *Coating Substrates and Textiles*. (Springer Berlin Heidelberg, Berlin, Heidelberg, 2012).

76. Xu, X. *et al.* Slippery-Liquid-Infused Electrostatic Flocking Surfaces for Marine Antifouling Application. *Langmuir* **37**, 10020–10028 (2021).

77. Zheng, Y., Zhou, X., Xing, Z. & Tu, T. Fabrication of a superhydrophobic surface with underwater air-retaining properties by electrostatic flocking. *RSC Adv.* **8**, 10719–10726 (2018).

78. Ni, J., Feng, K., Zhao, H., Wang, Z. & Meng, Z. Wettability enhancement of high-speed steel surface with electrostatic flocking method. *Colloids Surf A* **651**, 129781 (2022).

79. Wang, Y. *et al.* A cilia-inspired micropatterned sensor with a high-permittivity dielectric hydrogel for ultrasensitive mechanoreception both in air and underwater. *J. Mater. Chem. A* **11**, 26562–26572 (2023).

80. Sung, B. *et al.* Fine-Particle Collection Using an Electrostatic Precipitator Equipped With an Electrostatic Flocking Filter as the Collecting Electrode. *Plasma Polym* **3**, 661–667 (2006).

81. Li, X. *et al.* Three-dimensional stretchable fabric-based electrode for supercapacitors prepared by electrostatic flocking. *J Chem Eng* **390**, 124442 (2020).

82. Luo, J. *et al.* Ultrasensitive airflow sensor prepared by electrostatic flocking for sound recognition and motion monitoring. *Mater. Horiz.* **9**, 1503–1512 (2022).

83. Hitzbleck, M., Lovchik, R. D. & Delamarche, E. Flock-Based Microfluidics. *Adv Mater* **25**, 2672–2676 (2013).

84. Guo, Y. *et al.* Solar-Driven All-in-One Interfacial Water Evaporator Based on Electrostatic Flocking. *Adv Sustain Syst* **5**, 2000202 (2021).

85. Gossla, E. *et al.* Electrostatic flocking of chitosan fibres leads to highly porous, elastic and fully biodegradable anisotropic scaffolds. *Acta Biomater* **44**, 267–276 (2016).

86. A. McCarthy, J. V. John, L. Saldana, H. Wang, M. Lagerstrom, S. Chen, Y. Su, M. Kuss, B. Duan, M. A. Carlson, J. Xie. Electrostatic Flocking of Insulative and Biodegradable Polymer Microfibers for Biomedical Applications. *Adv. Healthc. Mater.* **10**, e2100766 (2021).

87. Walther, A. *et al.* Novel Textile Scaffolds Generated by Flock Technology for Tissue Engineering of Bone and Cartilage. *Mater* **5**, 540–557 (2012).

88. McCarthy, A., Shah, R., John, J. V., Brown, D. & Xie, J. Understanding and utilizing textile-based electrostatic flocking for biomedical applications. *Appl Phys Rev* **8**, 041326 (2021).

89. Uetani, K. *et al.* Elastomeric Thermal Interface Materials with High Through-Plane Thermal Conductivity from Carbon Fiber Fillers Vertically Aligned by Electrostatic Flocking. *Adv Mater* **26**, 5857–5862 (2014).

90. Büttel, U. *Beflocken von Kunststoffen*. vol. 2 (Carl Hanser Verlag, 2016).

91. Bolgen, S. W. Flocking Technology. *J Coat Fabr* **21**, 123–131 (1991).

92. Borchert+Moller GmbH, Technische Information D453/5-09.

93. Borchert+Moller GmbH, Technische Information Tubicoll. (2008).

94. Borchert+Moller GmbH, Technische Information Kleber L 860. (2017).

95. Gong, R.H.*Specialist Yarn and Fabric Structures: Developments and Applications*. (Woodhead Publishing, 2011).

96. Hopmann, C. *Technologie der Kunststoffe: Lern- und Arbeitsbuch für die Aus- und Weiterbildung*. vol. 5 (Carl Hanser Verlag, 2021).

97. Wyss, D., Wyss, W. & Lerch, E. Electrically conductive flock for electrostatic flocking. US3511704A (1967).

98. Marti, T. Process for preparing flock fibers for electrostatic flocking. US3935370 (1972).

99. Sun, Y., Wang, S., Li, M., Gu, Y. & Zhang, Z. Improvement of out-of-plane thermal conductivity of composite laminate by electrostatic flocking. *Mater Des* **144**, 263–270 (2018).

100. Takeshita, T. *et al.* Relationship between Contact Pressure and Motion Artifacts in ECG Measurement with Electrostatic Flocked Electrodes Fabricated on Textile. *Sci Rep* **9**, 5897 (2019).

101. McCarthy, A. *et al.* Extracellular Matrix Secretion Mechanically Reinforces Interlocking Interfaces. *Adv Mater* **35**, 2207335 (2023).

102. Shen, C., Sun, S., Zhang, H. & Zhang, Z. Bioinspired Ultrasensitive and Flexible Airflow Sensor based on Short Carbon Fiber Network. *Adv Materials Technologies* **8**, 2200571 (2023).

103. Tashiro, K., Kobayashi, M. & Tadokoro, H. Elastic Moduli and Molecular Structures of Several Crystalline Polymers, Including Aromatic Polyamides. *Macromol* **10**, 413–420 (1977).

104. Gill, R. A. & Steele, R. The resiliency and modulus of viscose rayon as a function of swelling and temperature. *J. Appl. Polym. Sci.* **5**, 589–600 (1961).

105. Gleissner, C., Bechtold, T. & Pham, T. Enhancing the Wettability of Fibre Surface: A Comparative Experimental Study of Different Surface Activation Principles on Single Polyamide Fibre. *Fibers Polym* **24**, 4241–4252 (2023).

106. Rojo, E. *et al.* Alkali treatment of viscose cellulosic fibers from eucalyptus wood: Structural, morphological, and thermal analysis. *J of Applied Polymer Sci* **130**, 2198–2204 (2013).

107. Washburn, E. W. The Dynamics of Capillary Flow. *Phys. Rev.* **17**, 273–283 (1921).

108. Usevičiūtė, L. & Baltrėnaitė-Gedienė, E. Modelling of a Capillary Rise Height of Biochar by Modified Lucas–Washburn Equation. *Environ Model Assess* **27**, 29–43 (2022).

109. Markl, D. *et al.* Mathematical modelling of liquid transport in swelling pharmaceutical immediate release tablets. *Int J Pharm* **526**, 1–10 (2017).

110. Schurhardt, D. R. & Berg, J. C. LIQUID TRANSPORT IN COMPOSITE CELLULOSE - SUPERABSORBENT FIBER NETWORKS. *Wood Fiber Sci.* **23**, 342–357 (1991).

111. Shi, S. Q. & Gardner, D. J. A new model to determine contact angles on swelling polymer particles by the column wicking method. *J. Adhes. Sci. Technol.* **14**, 301–314 (2000).

112. Brugnara, M. Using the ESEM for the Measurement of Contact Angles on Flat Samples. *Microsc. Anal.* **21**, 17–19 (2007).

113. Lawrence, M. G. The Relationship between Relative Humidity and the Dewpoint Temperature in Moist Air: A Simple Conversion and Applications. *Bull. Amer. Meteor. Soc.* **86**, 225–234 (2005).

114. Sun, J. Facile fabrication of a superhydrophilic–superhydrophobic patterned surface by inkjet printing a sacrificial layer on a superhydrophilic surface. *RSC Adv* **6**, 31470-31475 (2016).

115. Agarwaal, S., Burgard, M., Greiner, A. & Wendorff, J. H. *Electrospinning: A Practical Guide to Nanofibers*. (De Gruyter, 2016).

116. Wendorff, J. H., Agarwaal, S. & Greiner, A. *Electrospinning: Materials, Processing, and Applications*. (Wiley-VCG, 2012).

117. Marmur, A. Hydro- hygro- oleo- omni-phobic? Terminology of wettability classification. *Soft Matter* **8**, 6867 (2012).

118. Ölçeroğlu, E. & McCarthy, M. Self-Organization of Microscale Condensate for Delayed Flooding of Nanostructured Superhydrophobic Surfaces. *ACS Appl. Mater. Interfaces* **8**, 5729–5736 (2016).

119. Chen, D., Li, J., Zhao, J., Guo, J., Zhang, S., Sherazi, T. A., Ambreen, Li, S. Bioinspired superhydrophilic-hydrophobic integrated surface with conical pattern-shape for self-driven fog collection. *J. Colloid Interface Sci.* **530**, 274–281 (2018).

120. Heng, X., Xiang, M., Lu, Z., Luo, C. Branched ZnO wire structures for water collection inspired by cacti. *ACS Appl. Mater. Interfaces* **6**, 8032–8041 (2014).

121. Cantekin, S., De Greef, T. F. A. & Palmans, A. R. A. Benzene-1,3,5-tricarboxamide: a versatile ordering moiety for supramolecular chemistry. *Chem. Soc. Rev.* **41**, 6125 (2012).

122. Weiss, D., Kreger, K. & Schmidt, H.-W. Self-Assembly of Alkoxy-Substituted 1,3,5-Benzenetrisamides Under Controlled Conditions. *Macromol. Mater. Eng.* **302**, 1600390 (2017).

123. Drummer, M. *et al.* Stable Mesoscale Nonwovens of Electrospun Polyacrylonitrile and Interpenetrating Supramolecular 1,3,5-Benzenetrisamide Fibers as Efficient Carriers for Gold Nanoparticles. *ACS Appl. Mater. Interfaces* **13**, 34818–34828 (2021).

124. Weiss, D. *et al.* Tailoring Supramolecular Nanofibers for Air Filtration Applications. *ACS Appl. Mater. Interfaces* **8**, 14885–14892 (2016).

125. Frank, A. *et al.* Functional Mesostructured Electrospun Polymer Nonwovens with Supramolecular Nanofibers. *Macromol. Rapid Commun.* **43**, 2200052 (2022).

126. A. Frank, A. Bernet, K. Kreger, H.-W. Schmidt. Supramolecular microtubes based on 1,3,5-benzenetricarboxamides prepared by self-assembly upon heating. *Soft Matter* **16**, 4564–4568 (2020).

127. Cui, X., Chen, G. & Han, X. Experimental Vapor Pressure Data and a Vapor Pressure Equation for *N* , *N* -Dimethylformamide. *J. Chem. Eng. Data* **51**, 1860–1861 (2006).

128. Berman, N. S., Larkam, C. W. & McKetta, J. J. Vapor Heat Capacity and Heat of Vaporization of 2-Propanol. *J. Chem. Eng. Data* **9**, 218–219 (1964).

129. Chen, H. *et al.* Ultrafast water harvesting and transport in hierarchical microchannels. *Nat Mater* **17**, 935–942 (2018).

130. J. Wang, S. Yi, Z. Yang, Y. Chen, L. Jiang, C.-P. Wong. Laser Direct Structuring of Bioinspired Spine with Backward Microbarbs and Hierarchical Microchannels for Ultrafast Water Transport and Efficient Fog Harvesting. *ACS Appl. Mater. Interfaces* **12**, 21080–21087 (2020).

131. Chen, Y. *et al.* Light-driven dandelion-inspired microfliers. *Nat Commun* **14**, 3036 (2023).

132. Yang, J., Zhang, H., Berdin, A., Hu, W. & Zeng, H. Dandelion-Inspired, Wind-Dispersed Polymer-Assembly Controlled by Light. *Adv Sci* **10**, 2206752 (2023).

133. Kim, B. H. *et al.* Three-dimensional electronic microfliers inspired by wind-dispersed seeds. *Nature* **597**, 503–510 (2021).

134. Iyer, V., Gaensbauer, H., Daniel, T. L. & Gollakota, S. Wind dispersal of battery-free wireless devices. *Nature* **603**, 427–433 (2022).

135. Ledda, P. G., Siconolfi, L., Viola, F., Camarri, S. & Gallaire, F. Flow dynamics of a dandelion pappus: A linear stability approach. *Phys Rev Fluids* **4**, (2019).

136. D. Nioras, K. Ellinas, V. Constantoudis, E. Gogolides. How Different Are Fog Collection and Dew Water Harvesting on Surfaces with Different Wetting Behaviors? *ACS Appl. Mater. Interfaces.* **13**, 48322–48332 (2021).

137. Kooij, S., Astefanei, A., Corthals, G. L. & Bonn, D. Size distributions of droplets produced by ultrasonic nebulizers. *Sci Rep* **9**, 6128 (2019).

138. Azad, M. A. K., Ellerbrok, D., Barthlott, W. & Koch, K. Fog collecting biomimetic surfaces: Influence of microstructure and wettability. *Bioinspir Biomim* **10**, 016004 (2015).

139. Knapczyk-Korczak, J. & Stachewicz, U. Biomimicking spider webs for effective fog water harvesting with electrospun polymer fibers. *Nanoscale* **13**, 16034–16051 (2021).

140. Knapczyk-Korczak, J., Szewczyk, P. K., Ura, D. P., Berent, K. & Stachewicz, U. Hydrophilic nanofibers in fog collectors for increased water harvesting efficiency. *RSC advances* **10**, 22335–22342 (2020).

141. Schneider, C. A. NIH Image to ImageJ: 25 years of image analysis. *Nat Methods* **9**, 671-675 (2012)

142. Kassambara, A. ggpubr: 'ggplot2' Based Publication Ready Plots. (2020).

143. Wickham, H. *Ggplot2: Elegant Graphics for Data Analysis*. (Springer-Verlag New York, 2016).

144. Xu, S. *et al.* Use ggbreak to effectively utilize plotting space to deal with large datasets and outliers. *Front genet* **12**, 774846 (2021).

145. M. Weber, F. Bretschneider *et al.*, Mimicking cacti spines via hierarchical self-assembly for water collection and unidirectional transport *Adv. Mater. Interfaces* **11***,* 2400101 (2024)

Danksagung

Zunächst möchte ich mich bei Prof. Dr. Andreas Greiner bedanken. Sie haben mir dieses vielseitige und interessante Thema und die benötigten Mittel zur Verfügung gestellt. Darüber hinaus waren Sie immer für offene und hilfreiche Gespräche erreichbar. Vielen Dank, dass Sie mir die kreative Freiheit geben und auch das Vertrauen in mich gesetzt haben.

Des Weiteren möchte ich bei Prof. Dr. Seema Agarwal bedanken. Sie haben mir permanent Denkanstöße und Inspiration für weitere Experimente gegeben. Gerade Ihr Interesse und Anmerkungen haben es mir ermöglicht meine Arbeit von einer anderen Seite zu betrachten.

Eine besondere Dankbarkeit bin ich Prof. Dr. Hans-Werner Schmidt verpflichtet. Ihr Interesse, offenes Ohr und Kreativität war eine maßgebliche Motivation für diese Arbeit. Darüber hinaus bin ich Ihnen zutiefst für die Stunden an Arbeit dankbar, die Sie in Melinas und meine Forschung investiert haben.

Des Weiteren möchte ich Dr. Klaus Kreger für die Diskussionen, Ratschläge und Interesse danken. Ohne deine Hilfe wäre die gemeinsame Publikation nicht möglich gewesen.

Einen riesigen Dank geht an Melina Weber ohne deren Einfluss die Arbeit nicht zustande gekommen wäre. Neben deinem scheinbar unendlichen Fachwissen möchte ich mich besonders für dein immer offenes Ohr bedanken.

In keiner besonderen Reihenfolge möchte ich meinen Dank an die folgenden Personen ausrichten, ohne denen die Arbeit nicht möglich gewesen wäre:

Dr. Holger Schmalz und Lothar Benker für sämtliche RAMAN Messungen.

Dr. Ulrich Mansfeld für die Einführung in die Elektronenmikroskopie und seine Interesse und Hilfe bei sämtlichen Mikroskopie Fragen. Darüber hinaus möchte ich ihn auch für die Unterstützung bei den ESEM-Messungen danken.

Martina Heider für ein immer freundliches Ohr sowie jegliche Unterstützung bei den SEM-Messungen.

Alexander Kern für sein umfassendes technisches Wissen und Unterstützung und die vielen Stunden am 3D Drucker.

Nina Volk für die freundlichen Gesprächen und die Unterstützung für ICP-OES und TEM Messungen.

Nina Volk, Simon Knorr, Sophie Fritze, und Tasmai Paul für die Unterstützung bei ICP-OES Messungen und den Mikrowellen Aufschlüssen.

Rika Schneider für GPC-Messungen und Einführung in die DLS.

Lothar Benker für das Teilen des Büroplatzes und für die vielen Diskussionen.

Meine direkten Laborkollegen Sophie Fritze, Thomas Schmitt, Emilia Fulajtar, Hendrik Volz, Yinging Ding, Lisa Leitner, Lars Schwarzer, Yannick Eich, und Chenhui Ding.

Melina Weber, Sophie Fritze, Tasmai Paul, Marius Schmidt, Thomas Schmitt und Elke Reuschel für die finale Korrekturrunde und die hilfreichen Anmerkungen.

Meine ehemaligen Kollegen Dr. Adrian Wambach, Dr. Ann-Kathrin Müller und Thomas Schmitt für die Unterstützung am Lehrstuhl am Anfang meiner Arbeit.

Meine Kollegen der MCI und MCII für die freundliche Unterstützung und Diskussionen.

Den Botanischen Garten der Universität Bayreuth (UBT) für die Bereitstellung von Kaktus Stacheln.

Als letztes möchte ich mich zutiefst bei meiner Familie und bei meinen Freunden bedanken, die mich unnachgiebig und bindungslos bei meiner akademischen Reise sowohl in schlechten und als auch in guten Zeiten begleitet und unterstützt haben.

(Eidesstattliche) Versicherungen und Erklärungen

(§9 Satz 2 Nr. 3 PromO BayNat)

Hiermit versichere ich eidesstattlich, dass ich die Arbeit selbstständig verfasst und keine anderen als die von mir angegebenen Quellen und Hilfsmittel benutzt habe (vgl. Art. 97 Abs. 1 Satz 8 BayHIG)

(§9 Satz 2 Nr. 3 PromO BayNat)

Hiermit erkläre ich, dass ich die Dissertation nicht bereits zur Erlangung eines akademischen Grades eingereicht habe und dass ich nicht bereits diese oder eine gleichartige Doktorprüfung endgültig nicht bestanden habe.

(§9 Satz 2 Nr. 4 PromO BayNat)

Hiermit erkläre ich, dass ich Hilfe von gewerblichen Promotionsberatern bzw. -vermittlern oder ähnlichen Dienstleistern weder bisher in Anspruch genommen habe noch künftig in Anspruch nehmen werde.

(§9 Satz 2 Nr. 7 PromO BayNat)

Hiermit erkläre ich mein Einverständnis, dass die elektronische Fassung meiner Dissertation unter Wahrung meiner Urheberrechte und des Datenschutzes einer gesonderten Überprüfung unterzogen werden kann.

(§9 Satz 2 Nr. 8 PromO BayNat)

Hiermit erkläre ich mein Einverständnis, dass bei Verdacht wissenschaftlichen Fehlverhaltens Ermittlungen durch universitätsinterne Organe der wissenschaftlichen Selbstkontrolle stattfinden können.

_____

Ort, Datum, Unterschrift